

20170727: DARK MATTER SEARCH AND ELECTRON BACKGROUND
EVALUATION
TESTING OF TPC GRID DESIGNING

A DISSERTATION
SUBMITTED TO THE DEPARTMENT OF PHYSICS
AND THE COMMITTEE ON GRADUATE STUDIES
OF STANFORD UNIVERSITY
IN PARTIAL FULFILLMENT OF THE REQUIREMENTS
FOR THE DEGREE OF
DOCTOR OF PHILOSOPHY

Wei Ji
August 2018

¹³

© Copyright by Wei Ji 2018

¹⁴

All Rights Reserved

I certify that I have read this dissertation and that, in my opinion, it is fully adequate in scope and quality as a dissertation for the degree of Doctor of Philosophy.

15

(Tom Shutt) Principal Adviser

I certify that I have read this dissertation and that, in my opinion, it is fully adequate in scope and quality as a dissertation for the degree of Doctor of Philosophy.

16

(Dan Akerib)

I certify that I have read this dissertation and that, in my opinion, it is fully adequate in scope and quality as a dissertation for the degree of Doctor of Philosophy.

17

(Peter Graham)

I certify that I have read this dissertation and that, in my opinion, it is fully adequate in scope and quality as a dissertation for the degree of Doctor of Philosophy.

18

(Giorgio Gratta)

I certify that I have read this dissertation and that, in my opinion, it is fully adequate in scope and quality as a dissertation for the degree of Doctor of Philosophy.

19

()

Approved for the Stanford University Committee on Graduate Studies

20

²¹ Preface

²² This thesis is discussing about the design and validation of liquid xenon LZ Dark Matter experiment
²³ and results from LUX Dark Matter experiment.

²⁴ **Acknowledgments**

²⁵ I would like to thank you Dan, for everything.

²⁶ Contents

²⁷ Preface	iv
²⁸ Acknowledgments	v
²⁹ List of Tables	viii
³⁰ List of Figures	ix
³¹ 1 Gas Test descriptions	1
³² 1.1 The gaseous detector	2
³³ 1.2 Data Acquisition	7
³⁴ 1.3 Operation	11
³⁵ 1.4 Data processing	14
³⁶ 1.5 PMT Calibration	17
³⁷ 1.6 Light Collection	20
³⁸ 1.7 Light production	25
³⁹ 1.8 Signals	30
⁴⁰ 1.8.1 Electron emission	32
⁴¹ 1.8.2 Particle radiation	36
⁴² 1.8.3 Cosmic ray	53
⁴³ 1.8.4 Other miscellaneous sources	55
⁴⁴ 1.9 Signal selections	72
⁴⁵ 1.9.1 Signal selections based on signal shape	72
⁴⁶ 1.9.2 Signal selections based on previous signals	79
⁴⁷ 1.9.3 Signal selections varying $\Delta V_{T,B}$ and operating gas density	85
⁴⁸ 1.10 Evaluation	92
⁴⁹ 1.10.1 Simulations	92
⁵⁰ 1.10.2 Summary	93

51	A Gas Test RQ documentation	94
52	B Abbreviations	101
53	Bibliography	103

⁵⁴ List of Tables

⁵⁵ 1.1	Spectral response of PMTs tested at Hamamatsu Photonics	5
⁵⁶ 1.2	Data Acquisition system parameters.	8
⁵⁷ 1.3	PMT dead time duration	11
⁵⁸ 1.4	PMT calibration.	20
⁵⁹ 1.5	Light collection simulation geometry parameters.	24
⁶⁰ 1.6	Light collection simulation material parameters.	24
⁶¹ A.1	<i>Gas Test</i> RQ documentation	100

⁶² List of Figures

63 1.1	<i>Gas Test</i> apparatus physical layout.	4
64 1.2	<i>Gas Test</i> electroluminescence detector.	6
65 1.3	<i>Gas Test</i> signal: example waveforms during dead time.	10
66 1.4	Distribution of PMT time differences between pulses in one PMT.	12
67 1.5	<i>Gas Test</i> good and bad voltage configurations.	15
68 1.6	PMT pulse amplitude distribution.	19
69 1.7	PMT SPHE pulse amplitude vs. pulse area distribution.	21
70 1.8	Light collection efficiency of (r, z) cross section in the ELD from simulation.	26
71 1.9	Light collection efficiency and TBA in the EL region in different grid configurations from simulation.	27
72 1.10	Light collection efficiency in the EL region with different PTFE reflectivity from simulation.	27
73 1.11	The reduced first Townsend ionization coefficient $\eta \equiv \alpha/E$ for neon, argon, krypton, and xenon.	31
74 1.12	<i>Gas Test</i> electron emission event from grid wires	33
75 1.13	<i>Gas Test</i> detector electric field.	35
76 1.14	A 3D simulation of an electron drifting in an axially symmetric electric field in xenon gas.	37
77 1.15	Simulated cathodic electron gas gain vs. reduced surface electric field.	38
78 1.16	Simulated signal areas vs. ΔV_{T-B}	39
79 1.17	Attenuation length of photon in xenon.	40
80 1.18	CSDA range of electrons in xenon.	41
81 1.19	<i>Gas Test</i> signal: anode cone event.	43
82 1.19	<i>Gas Test</i> signal: anode cone event (cont.).	44
83 1.20	<i>Gas Test</i> signal: cathode cone event.	45
84 1.21	<i>Gas Test</i> signal: S1 S2 event in the cathode corner.	46
85 1.22	Electrostatic solution of the <i>Gas Test</i> detector (grid ring region).	47

90	1.23 <i>Gas Test</i> signal: S1 S2 event in the EL region.	49
91	1.24 <i>Gas Test</i> signal: grid wire region event.	50
92	1.25 <i>Gas Test</i> signal: grid ring region event.	51
93	1.26 <i>Gas Test</i> signal: multiple scattering event.	52
94	1.27 <i>Gas Test</i> signal: EL region muon event.	54
95	1.28 <i>Gas Test</i> signal: muon event between the grid rings.	56
96	1.29 <i>Gas Test</i> signal: anode cone muon event.	57
97	1.29 <i>Gas Test</i> signal: anode cone muon event (cont.).	58
98	1.30 <i>Gas Test</i> signal: cathode cone muon event.	59
99	1.31 <i>Gas Test</i> signal: electronic noise.	61
100	1.32 <i>Gas Test</i> signal: PMT dark current accidental coinciding.	61
101	1.33 <i>Gas Test</i> signal: PTFE fluorescence after an event with large photon production.	63
102	1.33 <i>Gas Test</i> signal: PTFE fluorescence after an event with large photon production (cont.).	64
103	1.34 Photon fluorescence rate after photon production in the ELD.	65
104	1.35 The average of scaled waveform in the range of 0 μ s to 2000 μ s since source signals.	67
105	1.36 The ratio of the number of photon in the range of 200 μ s to 600 μ s since source signals to the number of photons in the source signal.	67
106	1.37 <i>Gas Test</i> signal: Cherenkov radiation in PTFE.	69
108	1.38 <i>Gas Test</i> signal t_{10-90} duration vs. signal area.	71
109	1.39 <i>Gas Test</i> signal selection (part 1).	81
110	1.39 <i>Gas Test</i> signal selection (part 2).	82
111	1.39 <i>Gas Test</i> signal selection (part 3).	83
112	1.39 <i>Gas Test</i> signal selection (part 4).	84
113	1.40 <i>Gas Test</i> signal selection with ΔV_{T-B} at 8 kV, operating gas density at 0.137 mol L $^{-1}$	86
114	1.41 <i>Gas Test</i> signal selection with ΔV_{T-B} at 10 kV, operating gas density at 0.137 mol L $^{-1}$	87
115	1.42 <i>Gas Test</i> signal selection with ΔV_{T-B} at 12 kV, operating gas density at 0.137 mol L $^{-1}$	88
116	1.43 <i>Gas Test</i> signal selection with ΔV_{T-B} at 14 kV, operating gas density at 0.137 mol L $^{-1}$	89
117	1.44 <i>Gas Test</i> signal selection with ΔV_{T-B} at 16 kV, operating gas density at 0.137 mol L $^{-1}$	90
118	1.45 <i>Gas Test</i> signal selection with ΔV_{T-B} at -12 kV, operating gas density at 0.137 mol L $^{-1}$	91

¹¹⁹ **Chapter 1**

¹²⁰ ***Gas Test descriptions***

¹²¹ In LZ, metallic wire grids under high voltage are used to form electric fields. We apply one field
¹²² in the liquid volume to drift ionization electrons upwards and another in the gas volume to extract
¹²³ these electrons from the liquid in order to produce proportional scintillation light (S2). Achieving
¹²⁴ high voltages on such grids is necessary for the operation of the LZ TPC. However, such high voltages
¹²⁵ also increase the rate of electron emission ,which is one of the potential sources of background in
¹²⁶ LZ. Therefore, reduction of the field induced electron emission rate should greatly benefit physics
¹²⁷ studies in the LZ detector.

¹²⁸ Electric field induced electron emission from metallic surfaces is a well known phenomenon. The
¹²⁹ electric field lowers the potential energy outside the metallic surface allowing electrons to come out
¹³⁰ from the metallic surface. The rate of electric field induced electron emission increases with the
¹³¹ electric field on the metallic surface.

¹³² The electric field induced electron emission events are potential problems in LZ for three reasons.
¹³³ First, these events look like low energy events in the LZ detector. Thus, reduction of electron
¹³⁴ emission background rate from the grid wires improves our sensitivity to low energy events. This
¹³⁵ in turn improves our ability to study low mass WIMPs. Second, the electron emission events may
¹³⁶ accidentally coincide with WIMP signals which we want to study in the LZ detector. Reduction
¹³⁷ of electron emission rate helps to keep the data recording environment in LZ cleaner. This reduces
¹³⁸ the systematic errors for S1 and S2 and improves their quality. From that, we improve our events
¹³⁹ classification and energy reconstruction. This in turn improves all physics studies using the LZ
¹⁴⁰ detector. Finally, the electron emission events interrupt the desired data recording capability of
¹⁴¹ the LZ detector. This may prevent or interrupt recordings of wanted data. Thus, the reduction of
¹⁴² electron emission rate helps to keep the data recording environment in LZ quieter to allow longer
¹⁴³ detector live times for wanted events. In summary, the reduction of the electron emission event rates
¹⁴⁴ benefits LZ because of its impact on detector sensitivity, data quality and data acquisition live time.

¹⁴⁵ To achieve these qualities, we are developing a two-stage study on the reduction of the electric

146 field induced electron emission rate using two small detectors, *Gas Test* and *LZ System Test: Phase*

147 *I*. These two detectors are capable of testing a pair of grids which have surface areas $\sim 1\%$ the

148 area of grids that will be used in LZ. With these small detectors, we can study the effect of rate

149 reduction in a shorter time than if we were to use full-size grids. Thus, we use these detectors to

150 study parameters that may affect the emission rate in a short period of time.

151 At the first stage, a gaseous detector, “*Gas Test*”, is built to study different methods for reducing

152 the electron emission rate. This detector measures electron emission rates with different electric

153 fields before and after various physical and chemical treatments. Once we discover an effect on the

154 reduction of the electric field induced electron emission rate from these treatments, a second stage

155 of study with a liquid xenon detector, *LZ System Test: Phase I*, is undertaken to confirm that

156 reduction persists in a liquid xenon environment, like that of LZ.

157 After confirmation that a treatment produces a rate reduction, this treatment is used to produce

158 full-size LZ grids. A similar two-stage study method is used to test the full-size LZ grids in a gaseous

159 detector, *LZ System Test: Phase II*(details are described in Ref. ??), and the liquid xenon detector

160 LZ. These two detectors measure the performance and assure the quality of LZ grids.

161 This chapter focuses on descriptions of the *Gas Test* detector. I will first introduce the design

162 concepts for each individual component in *Gas Test* . Then I will discuss data acquisition and the

163 data processing framework. **Last, I will discuss the analysis framework ,which includes event selec-**

164 **tions , simulations and validations, as well as characteristic pulse shape and rate of the background**

165 **events.** Results from measurements for different grids in *Gas Test* will be discussed in Chapter.??.

166 1.1 The gaseous detector

167 The gaseous detector, *Gas Test*, is designed to study grid behavior under high voltage in LZ. It

168 measures scintillation and electroluminescence (EL) light signals from events in the detector. Pairs

169 of grids are made from the same waving technique, material, wire pitch, and wire diameter as the

170 grids that will be used in LZ. The same pair of grids can also be tested in *LZ System Test: Phase I*

171 to study their performance in liquid xenon. Since these grids are physically similar to the grids in

172 LZ except for the overall surface area, the results from studying these grids are useful for LZ grid

173 design.

174 The main interest of our study is the electron emission process from the grid wires, which

175 is studied by grid electron emission tests via using PMTs to detect the associated photon signals.

176 Before each grid electron emission test, a grid sparking test is carried out to understand the maximum

177 operating voltage and the optimal operating voltage. Grid sparking tests are performed with both

178 gaseous xenon and argon under various pressures in order to uncover discharges in the detector

179 via biasing the grids. It provides the detector operation information for grid emission tests. Grid

180 electron emission tests are usually performed with gaseous xenon, in which photons can be produced

181 for carrying out the electron emission signalmeasurements.

182 Next, I will introduce the design concepts of the components in the *Gas Test* detector.

183 **Detector** *Gas Test* detector is the main tool we used to study the electron emission process from
184 metallic grid wire surfaces. The *Gas Test* detector operates with xenon gas, argon gas, and vacuum.
185 The operating pressure for this detector is in the range of 10^{-5} bara to 3.5 bara.

186 A cylindrical vessel, the diameter of which is 10 inch and the height of which is 24 inch, is used to
187 host a electroluminescence detector(ELD), which detect measurable events. The pressure and the
188 temperature of the detector are monitored by sensors mounted above the vessel. A gas circulation
189 system is used to add, remove and purify gas in the detector. Fig. 1.1a and Fig. 1.1b show the
190 physical layout of the vessel setup and the ELD inside.

191 The electroluminescence detector (ELD) is the major location of active measurable electron
192 emission events. Its conceptual drawing is illustrated in Fig. 1.2. A pair of grids for measurement
193 are mounted in the center of the vessel. They are separated apart by 12 PEEK spacers, ,which are
194 13 mm in height. These two grids are biased to different voltages during the measurement. This
195 creates a voltage difference between the two grids. It enables electrons between these two grids to
196 produce EL photons ,which can be measured by the PMTs. The region between these two grids is
197 called the EL region.

198 These grids are named after their physical location in the detector as top grid and bottom grid.
199 The grid plane diameters are 140.9 mm for the top grid and 137.4 mm for the bottom grid. Voltages
200 of the two grids are noted as V_T for the top grid and V_B for the bottom grid. The voltage difference
201 between the top and bottom grids is expressed with ΔV_{T-B} (dV) $\equiv V_T - V_B$. These grids also
202 have another name by their bias voltages; the anodic grid and cathodic grid, and their voltage are
203 respectively V_A and V_C . The top grid is anodic and the bottom grid is cathodic when studying
204 electron emission from the bottom grid, which is called normal polarity operation. Occasionally, the
205 top grid is cathodic and the bottom grid is anodic when studying electron emission from the top
206 grid, which is called reverse polarity operation.

207 Two PTFE reflector cones are used to improve light collection efficiency for the primary scintil-
208 lation and EL photons. These reflector cones are mounted on the top and bottom of the EL region.
209 The surface of the PTFE cones overhang 0.1 mm above the grid. The diameters of the opening of
210 the PTFE cones to the grids are 130 mm. The EL region have the most sensitivity for grid electron
211 emission signal with regart to light collection. The EL region defines the overall grid surface area
212 of studying. Two PMTs mounted on the PTFE reflector cones are used to measure the primary
213 scintillation and EL photons. Distances between the PMTs to the closest grids are 110 mm.

214 The two PMTs used to measure the primary scintillation and EL photons from events happening
215 in the detector are model R11410-20 PMTs manufactured by Hamamatsu Photonics, as described
216 in Ref. [1]. The model of PMT has a synthetic quartz window that is mostly transparent to incident
217 photons of ~ 175 nm (xenon scintillation photons). The PMT window is coated with a bialkali



Figure 1.1: *Gas Test* apparatus physical layout. (a) The *Gas Test* detector: detector vessel (middle), electronic and gas gauge breakouts (top), Genie lift for detector assembly and disassembly (left), vacuum pumps and leak checking system (right). (b) ELD inside the detector vessel. (c) Gas circulation panel. (d) Circulation pump (left), and storage bottles (right).

photocathode material, which absorbs the incident photon and emits electrons by the photoelectric effect. The emitted electron which lands on the effective area of the first dynode is multiplied along the PMT dynode chain in an electron gain process and observed, which is the measured signal. The two PMTs are named after their physical location in the detector as top PMT and bottom(bot) PMT. Their spectral response of is summarized in Table 1.1.

	Top(top) PMT	Bottom(bot) PMT
Serial Number	KB1163	KB1170
Cathode Luminous Sens. [$\mu\text{A lm}^{-1}$]	149.0	148.0
Anode Luminous Sens. [A lm^{-1}]	657.0	1010.0
Anode Dark Current [nA]	1.00	4.60
Cathode Blue Sens. Index	12.60	12.30
Q.E. [%]		
165 nm	22.1	21.2
170 nm	33.3	32.6
175 nm	36.3	36.0
182 nm	37.1	37.0
188 nm	36.1	36.2
194 nm	33.9	34.1
200 nm	32.6	32.9

Table 1.1: Spectral response of PMTs tested at Hamamatsu Photonics.

A CAEN R1470ETD high voltage power supply is used to bias the two grids and the two PMTs. Two custom ceramic feed-throughs are used to deliver high voltage to the two grids in the detector vessel. Each feed-through has a low-pass filter box attached for noise removal. Custom designed cables and cable terminations are used to apply voltages through the feed-throughs to the grids. The cable terminations were a limitation on our ability to bias the grids to high voltage. New design elements have been introduced to solve this problem. Details of iterations of these designs will be discussed in Chapter. ??.

Gas circulation system A gas circulation system is used to purify, add, and remove xenon gas in the detector. The circulation system maintains the gas purity condition in the detector, which is essential for the operation for the following reasons. The purity of xenon gas ensures that electrons that are produced in the ELD do not combine with impurity atoms, thus decreasing the production of primary scintillation and EL light. The purity of xenon also has a notable effect on electron drift velocity in xenon gas, which biases our study; that is impure xenon gas tends to have a slower electron drift velocity. The deviation of electron drift velocity between different impurity levels can reach 20 % in certain reduced electric fields (ratio of electric field to gas density), as described in Ref. [Brooks1982]. This deviation biases the electron emission signal selection, which is based on the predicted pulse duration according to electron drift velocity, and introduces systematic error to the electron emission signal study.

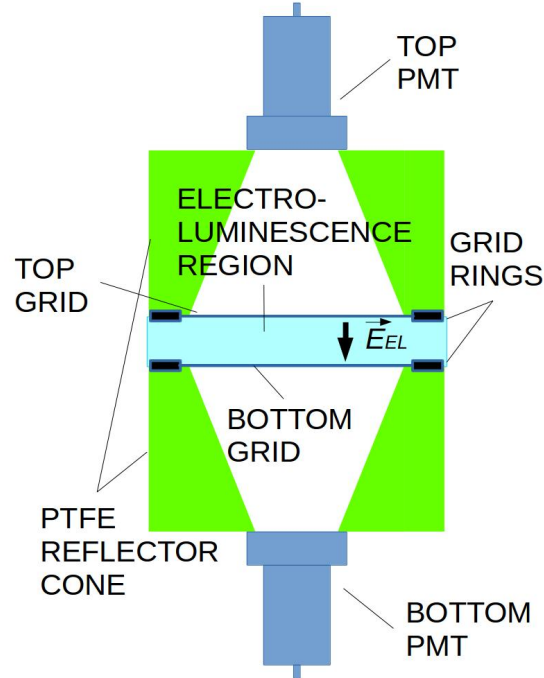


Figure 1.2: Conceptual drawing of *Gas Test* electroluminescence detector (ELD)

Xenon purification is carried out with the following elements in the gas circulation system. A gas circulation panel (Fig. 1.1c) is used to control the flow of xenon gas. A SAES PS3-MT3-R-1 rare gas purifier mounted on the circulation panel is used to purify the gas. The getter element has a sub-ppb efficiency of removing water, nitrogen, oxygen, carbon oxide, carbon dioxide, hydrogen, and hydrocarbons, as described in Ref. [2]. A custom pump (Fig. 1.1d) manufactured by KNF Neuberger, Inc. drives the gas circulation in the system. This pump is a type PM26101-0150.1.2.12 double diaphragm pump, which has company specified 1.5 bar operating pressure, as described in Ref. [3]. During the actual operation, the pump works at pressures of up to 3.7 bar with a leak rate less than 10^{-7} bar L s⁻¹. An Alicat MC-5SLPM-D-485 mass flow controller (MFC) on the gas circulation panel controls the circulation flow rate, which allows a maximum flow rate of 5 slpm, as described in Ref. [4]. During the gas purification process, the flow of gas was controlled and driven through the getter for \sim 20 min to allow the complete absorption of the gas impurities in the detector. This process is frequently conducted between each dataset to ensure the gas purity quality.

The addition and removal of xenon gas are carried out with the same gas panel. Two 4 L bottles (Fig. 1.1d) are used for the storage of xenon gas used in the tests when the gas is not used in the detector. During the xenon gas removal process, these bottles are inserted into two dewars filled with liquid nitrogen. Reducing the temperature of the bottles by using liquid nitrogen allows xenon

258 gas to flow through the gas circulation panel back to the bottles, and to condense inside the bottles.
259 During the addition of xenon gas process, the bottles are taken out from the dewar and warmed up.
260 This process raises the gas pressure in the bottle, which drives the gas to fill the detector through
261 the getter on the gas panel. The gas flow is controlled by the gas regulator and the MFC on the
262 panel.

263 1.2 Data Acquisition

264 A data acquisition(DAQ) system is used for recording PMT pulses for grid emission tests. The
265 DAQ system is designed and made at SLAC, previously used and tested in *LZ System Test: Phase*
266 *I* detector. The DAQ system is customized to maximize the probability for capturing single photon
267 electron (SPHE) pulses from the PMTs. This also enables the DAQ system to record electron
268 emission signals, which are collections of multiple SPHE pulses. The DAQ system contains three
269 parts: (1) amplification and digitization, (2) recording, and (3) transfer and storage. The DAQ
270 system works continuously, except when interrupted by the data transfer process. This interruption
271 is called dead time of the DAQ system. The dead time issue is addressed by the subtraction of live
272 times after each recorded pulses. Aspects of the DAQ system are described below.

273 **Amplification and digitization** This process amplifies and digitizes PMT pulse signals. The
274 amplification and digitization of the PMT signals are carried out by two separate custom made
275 boards. The amplification of signals improves signal to noise ratio. However, this amplification may
276 also cause distortion of the waveform if the pulse signal amplitude exceeds the maximum capability
277 of the electronic circuits in the amplification and digitization boards. Two amplifier gain settings
278 are implemented: low gain ($\times 12$), and high gain ($\times 100$). For electron emission tests, the low
279 gain setting is used to obtain a satisfactory signal to noise ratio. The low gain setting allows 40 to
280 60 SPHEs to be recorded simultaneously without distortion, when the high gain setting is not used
281 because its without distortion SPHE recording range is only 5 to 7 SPHEs, which is too small for the
282 counts of simultaneous SPHEs in electron emission signals. An optical fiber connecting these two
283 boards transfers the amplified PMT signals to the digitizer board. The digitizer board is capable of
284 doing a 16 bit digitization in a dynamic range of 2.5 V (~ -1.26 V to 1.24 V). The digitizer reverses
285 the polarity of signals, which changes SPHE pulses from negative spikes to positive spikes. The
286 digitizing sampling frequency is every 4 ns. Digitized data are written to a buffer memory in the
287 digitizer board. The amplification and digitization system sets the precision of SPHE measurement
288 and signal to noise ratio, and digitizes PMT pulse signals to be handled numerically later.

289 **Recording** The recording system for DAQ makes decisions for data recording. The decision
290 making algorithm is controlled by customized DAQ XML parameters in an XML file. The pulse
291 recording is undertaken in a pending mode without a conventional trigger, which is explained below.

292 First, the continuous digitized pulse amplitude data are compared to a pre-threshold voltage (trigger
 293 voltage), which is called the pre-threshold value, until a threshold crossing is reached. The time of
 294 this threshold crossing is the pulse recording reference time (trigger time). Pulse recording also
 295 includes a preceding segment of samples, which is called the pre-delay. The start time of the
 296 pre-delay period is the pulse recording start time. Next, digitized data are compared to a post-
 297 threshold voltage, which is called the post-threshold value, until a threshold crossing is reached.
 298 Then, the pulse recording continues for a succeeding segment of samples, which is called the post-
 299 delay. During the post-delay period, the digitized data are compared to the pre-threshold value
 300 again. If no pre-threshold crossing is reached, the pulse recording ends when the post-delay period
 301 ends. Otherwise, the DAQ system keeps recording until after a post-threshold crossing is reached,
 302 no other pre-threshold crossing is reached in the next post-delay period. The end time of the last
 303 post-delay period is the pulse recording stop time. The pre-threshold values are chosen so that the
 304 SPHE recording efficiency, also called the trigger efficiency, of both PMTs are larger than 95 %. The
 305 trigger efficiency is estimated by fitting SPHE amplitude distributions to Gaussian distributions, as
 306 described in Section 1.5. Results of these evaluations show that at normal PMT operating voltage
 307 (-1.5 kV) the top PMT and the bottom PMT have good trigger efficiency of 99.6 % and >99.9 %.
 308 The recorded pulses are called pulses of digitization (PODs), which are one of the fundamental
 309 elements for the next step; coinciding event building, as described in Section 1.4.

310 The used DAQ XML parameters during the tests are summarized in Table 1.2.

name	XML parameter name	value	explanation
post-delay	'PostDelay'	500 sample	counts of samples to keep after crossing post-trigger threshold ('PostThreshold').
pre-delay	'PreDelay'	30 sample	counts of samples to keep before crossing pre-trigger threshold ('PreThreshold').
post-threshold	'PostThreshold'	0x7D80 or as needed	crossing this threshold value determines the stop time of pulse recording.
pre-threshold	'PreThreshold'	0x7D61 or as needed	crossing this threshold value determines the start time of pulse recording.

Table 1.2: DAQ system parameters. (1 sample is 4 ns.)

311 **Transfer and storage** The transfer and storage system transfers data from the digitizer board
 312 and stores data in binary format in the main computer system. The buffer memory data that pass
 313 the selection of trigger algorithm are transferred through an optical fiber and written to files stored
 314 in the main computer. The data transfer speed is 250 MB s^{-1} . For an average pulse duration of

315 $2\ \mu\text{s}$ (500 sample), the DAQ allows approximately 30 thousand pulses to be recorded per second.
 316 The continuously recorded data are separately saved to series of files; each with a maximum size of
 317 1.1 GB. The process of data transfer interrupts the process of buffer memory writing of the incoming
 318 digitized data, which raises the dead time issue.

319 **Dead time** The dead time of DAQ is the segment of time that the DAQ system stops working
 320 after the end of each pulse recording. The reason for the dead time is because the process of buffer
 321 writing and the process of data transfer in the DAQ system cannot happen simultaneously. Dead
 322 time issue brings challenges in measuring electron emission rates. The duration of dead time shows
 323 a dependence on the preceding pulse duration. However, the quantitative relationship between the
 324 two is unclear. We address this issue by subtracting a segment of time succeeding each recorded
 325 pulse from the live time of study.

326 We studied the dead time issue by using two methods. The first method is finding problematic
 327 pulses that might be a result of dead time. We found there exist a population of pulses that when
 328 one PMT detects large quantities of photons, the other PMT detects no photon simultaneously.
 329 Since the two PMTs are observing the same space in the ELD, we expect to see similar magnitude of
 330 photons in both PMTs. The most likely reason for this to happen is that the other PMT channel is
 331 suffering from dead time. The other possible causes of these problematic pulses, such as misbehavior
 332 of one PMT, are less dominant. The time difference between the recording time of large quantities
 333 of photons in one PMT and the first preceding pulse in the dead time problematic PMT is the
 334 potential duration of dead time, as shown in Fig. 1.3. More than 400 dead time problematic pulses
 335 are examined. From the examinations, we found that for a particular pulse with a duration of $2\ \mu\text{s}$,
 336 the duration of dead time is in the range of $0.3\ \mu\text{s}$ to $15\ \mu\text{s}$. For longer pulses, we observe the duration
 337 of dead time for as long as $80\ \mu\text{s}$.

338 To estimate the systematic error, we employ a second method based on the idea that the presence
 339 of dead time will shift the distribution of time intervals between two consequential pulses in one PMT.
 340 In the absence of dead time, the time distribution should be an exponential distribution characterized
 341 by the average rate, which is expressed by:

$$\text{probability} = \frac{1}{\tau} \exp\left(-\frac{t}{\tau}\right) \quad (1.1)$$

342 where τ is the time constant, which is the inverse of the average rate.

343 Results of this shift are shown in Fig. 1.4. The figure includes studies of pulses categorized by
 344 their durations. These studies confirm the previous conclusion about the dead time issue and further
 345 show that the dead time duration is dependent on the preceding pulse duration. The low statistics
 346 at the small time interval range, e.g. range $0\ \mu\text{s}$ to $10^2\ \mu\text{s}$ for pulse length in the range of larger than
 347 $30\ \mu\text{s}$, clearly show the shift from the expected exponential distribution. The low statistic region
 348 varies with the preceding pulse duration, as summarized in Table 1.3. The difference on the slopes

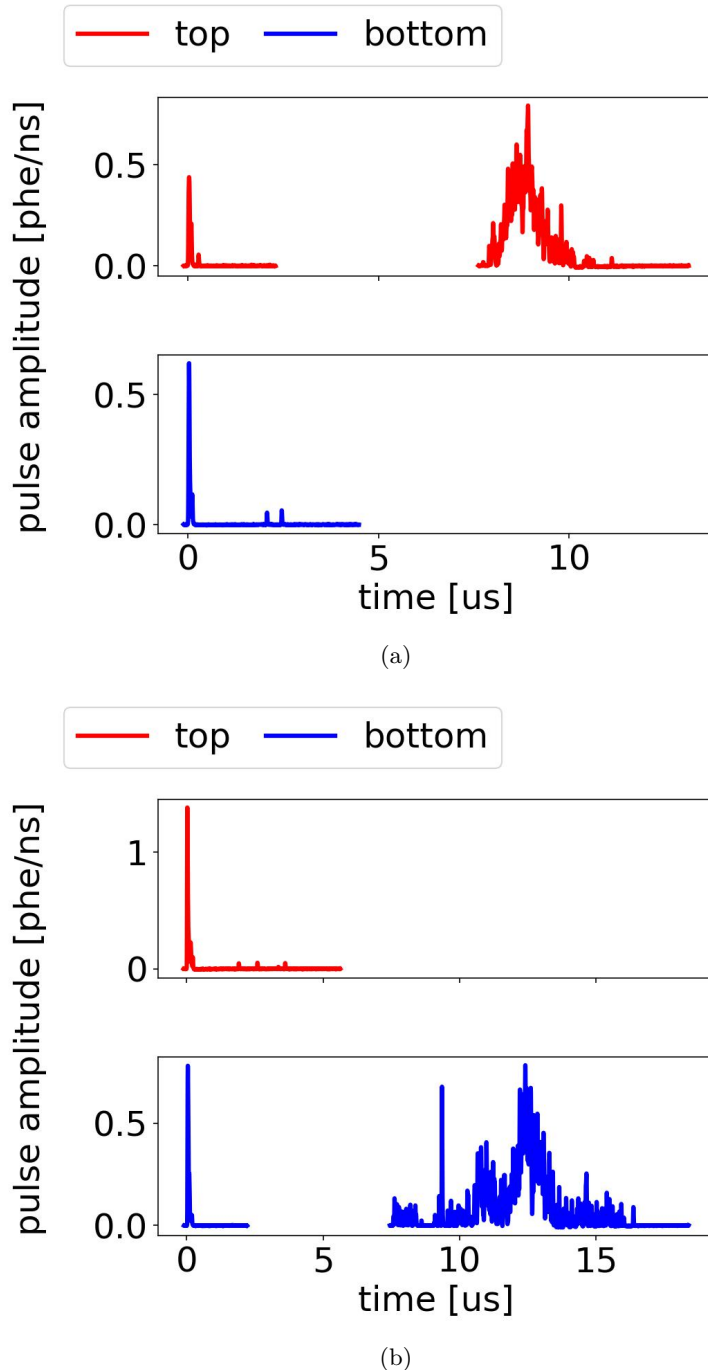


Figure 1.3: *Gas Test* signal: example waveforms during dead time. (a) The top PMT channel is suffering from dead time. (b) The bottom PMT channel is suffering from dead time.

349 of these curves is due to PTFE fluorescence that occurs subsequent to each pulse, which is more
350 obvious for larger-area (long-duration) pulses, and increases the average rate succeeding such pulses,
351 as will be discussed in Section 1.8.

pulse duration [μs]	dead time duration (low statistics region) [μs]	dead time duration (maximum observed) [μs]
all	7	80
[0, 3)	7	15
[3, 10)	10	15
[10, 30)	50	80
[30, ∞)	100	80

Table 1.3: PMT dead time duration. Data were taken at 2017-12-8 14:02, with grid voltages V_T and V_B at +6 kV and -6 kV, operating gas density at 0.137 mol L⁻¹.

352 Thus, to resolve the dead time issue, we subtract a segment of time after each recorded pulse from
353 the live time of study and eliminate all pulses that are recorded in this time period, as described in
354 Section 1.9. The remaining pulses are used to study the absolute rate of signals of interest; electron
355 emission signals. The rate of signals of interest is close to the absolute rate without the dead time
356 issue from the view of DAQ behavior.

357 1.3 Operation

358 We make sure to have stabilized operation conditions to study the electron emission process from
359 grids. This allows us to obtain results at a fixed condition and to compare results between different
360 operations.

361 **Operating conditions** When running the *Gas Test* electron emission tests, (1) the detector is
362 filled with xenon gas, (2) two PMTs are running stably, and (3) two grids are biased to proper
363 voltages.

364 The typical operating xenon gas density for the electron emission tests is 0.137 mol L⁻¹ (~3.3 bara
365 at temperature 295 K, or equivalent to the xenon gas density at 177 K on xenon liquid-vapor satu-
366 ration curve). This choice minimizes the probability of discharges between the two grid electrodes.
367 These discharges may cause potential damage to grids, and also prevent stable running of the tests.

368 The gas operating condition at a density of 0.137 mol L⁻¹ allows us to measure the electron
369 emissions in the sensitivity range of ΔV_{T-B} 8 kV to 16 kV. The grids that we use in our tests are
370 usually woven with a wire pitch of 5 mm and a wire diameter of 75 μm. For these grids, the sensitivity
371 ΔV_{T-B} range corresponds to an average wire surface electric field in the range of 65 kV cm⁻¹ to
372 110 kV cm⁻¹. However, since EL production decreases as the reduced electric field (ratio of electric

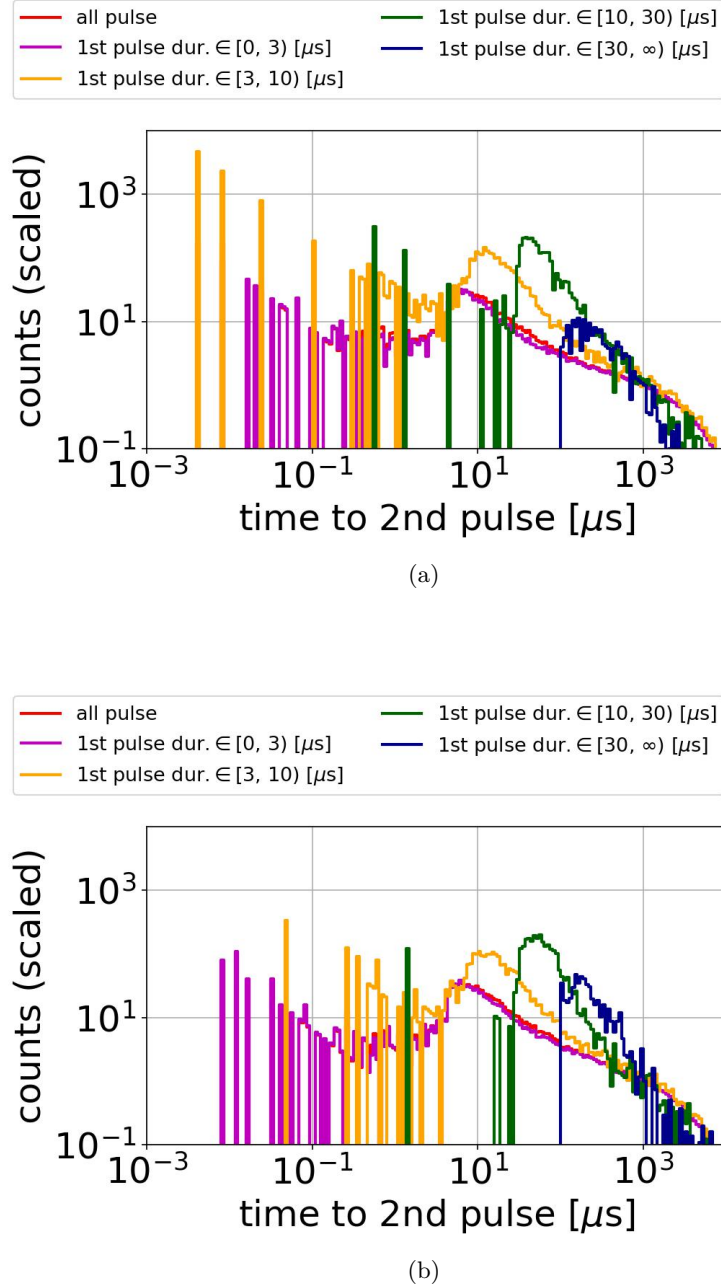


Figure 1.4: Distribution of PMT time differences between pulses in one PMT: (a) top PMT; (b) bottom PMT.

373 field to gas density) in the EL region decreases, the photon production per electron emission is
 374 smaller for a lower ΔV_{T-B} . This prevents us from having enough sensitivity to study the electron
 375 emission for a lower operating voltage and wire surface electric field. So the electron emission rate
 376 for a lower wire surface electric field is measured at a lower gas density to get an increase of the
 377 reduced electric field, which leads to a higher EL photon production in gas. The dependence of the
 378 EL light production on reduced electric field is described in Section 1.8.

379 Two PMTs normally operate at -1.5 kV . This guarantees that both PMTs have enough gain
 380 and signal to noise ratio. Before safely turning on the PMTs to measure the light from electron
 381 emissions from the grids, a series of tests are conducted to figure out the high voltage behavior
 382 and high voltage weak points in the system. Improvements are made to increase the maximum grid
 383 voltages V_T and V_B , under which the two grids do not create discharges. These improvements include
 384 cleaning the surface of spots which create discharges, increasing the smoothness and the rounding
 385 radius on the corner of metal surfaces, and increasing the distance between the electrodes and the
 386 ground. Physical contact with the grid wires is avoided during these improvements. The maximum
 387 grid voltages V_T and V_B that these grids can hold without creating discharges are measured with
 388 different gas (e.g. xenon, argon, and nitrogen) and different pressures. The dark current SPHE
 389 rate of both PMTs while they are stable running is approximately 0.500 kHz to 1 kHz . Test which
 390 produce a SPHE rate above 2.5 kHz are excluded.

391 The high voltage power supply is capable in biasing both grids separately in the range of -8 kV to
 392 8 kV . The current between the power supply and the grid is monitored to guarantee stable operation
 393 of grid bias voltages. An unstable grid biasing usually shows as a spike in the monitored current,
 394 and a spike on PMT recording rates. These segments of time referring to the unstable current are
 395 excluded.

396 **Obtaining data** The most common operating voltages we choose for electron emission measure-
 397 ments are $V_T = -V_B$ at $\pm 4\text{ kV}$, $\pm 4.5\text{ kV}$, $\pm 5\text{ kV}$, $\pm 5.5\text{ kV}$, $\pm 6\text{ kV}$, $\pm 6.5\text{ kV}$, $\pm 7\text{ kV}$, $\pm 7.5\text{ kV}$, and $\pm 8\text{ kV}$.
 398 This voltage range allows us to measure the electron emission rate vs. ΔV_{T-B} for most grids we study.
 399 Measurements outside this voltage range are also performed to understand the detector better. How-
 400 ever, their results usually are not included in the electron emission studies.

401 The typical duration for obtaining data is three minutes. An increasing trend of light production
 402 is seen during the operations when obtaining data takes longer than three minutes. This is probably
 403 from the increase of EL light production in the more ionized chamber environment and the increase
 404 of fluorescence light emissions from the PTFE reflector cones in the detector. Usually, after each
 405 3 min dataset, high voltage power for both grids are set back to 0 kV and rest for at least 30 s before
 406 the next measurement is taken. Obtaining data at each voltage configuration is handled by using
 407 scripts in Ignition slow control software, as described in Ref. [Ignition2018]. This is to make sure
 408 obtaining data is consistent and reproducible.

409 Datasets with the cathodic grid bias voltage $> -2.5\text{ kV}$ are explicitly excluded from electron

410 emission measurements. The reason is because this configuration allows electrons created by external
 411 particles in the cone region to drift to the EL region. These electrons will produce EL light in the
 412 EL region, the process of which could introduce a background rate for the electron emission studies.
 413 The process is illustrated in Fig. 1.5.

414 1.4 Data processing

415 Data processing is undertaken to save the useful information from the data by reducing the amount
 416 of extraneous information. The useful information of a pulse are characterized by Reduce Quantities
 417 (RQs) of a pulse.

418 The data processing framework includes three parts: (1) single pulse processing, (2) coinciding
 419 event building and coinciding pulse processing, and (3) random segment sampling of the dataset.

420 This section explains the main part of the data processing framework. It does not seek to explain
 421 all the RQs that have been computed. A full documentation of the RQs used in *Gas Test* analysis
 422 is summarized in Appendix A.

423 **Single pulse processing** A single pulse of digitization, POD, is defined to be the individual pulse
 424 recorded by the DAQ system in only one PMT channel. This processing requires two steps: (1)
 425 waveform reconstruction, and (2) pulse shape characterization.

426 The waveform is reconstructed by the following method. First, the baseline voltage of the pulse
 427 (RQ name: ‘baselines’) is identified based on the average DC voltages of the pulse of the first
 428 10 samples. The baseline voltage represents the voltage at the time when the pulse is recorded,
 429 assuming no pulse occurs. Samples used for identifying the baseline voltages are 80 ns ahead of the
 430 trigger time of the pulse. Therefore, these samples provide a reliable measure of the baseline as they
 431 are close in time from and unaffected by the rest of the pulses. There are certain fluctuations of
 432 baseline voltages for both PMTs. The amplitude of fluctuation ~ 0.36 mV is very small compared
 433 to the average SPHE pulse amplitude, which is 15 mV to 35 mV. After identifying the baseline,
 434 the baseline value was subtracted from the digitized data to get the waveform of the pulse. The
 435 waveform is then scaled back from ADC counts to mV to get the reconstructed waveforms. Along
 436 this process, RQs for the voltage of the trigger sample (RQ name: ‘trigvals’), and the voltage of the
 437 first sample (RQ name: ‘firstvals’) are also calculated.

438 From the reconstructed waveform, the maximum positive amplitudes (RQ name: ‘waveampli-
 439 tudes’) and the pulse area (RQ name: ‘waveareas’), which is the time integral of the pulse amplitude,
 440 are calculated. However, because of the long post-delay duration ($2 \mu\text{s}$, 500 sample) from the DAQ
 441 pulse recording, baseline fluctuation during the post-delay period is included in the total time inte-
 442 gral of the pulse area. This biases our understanding of the pulse areas. Thus, another revised pulse
 443 area RQ (RQ name: ‘waveareas_trim_end’) is calculated by integrating the waveform which has the

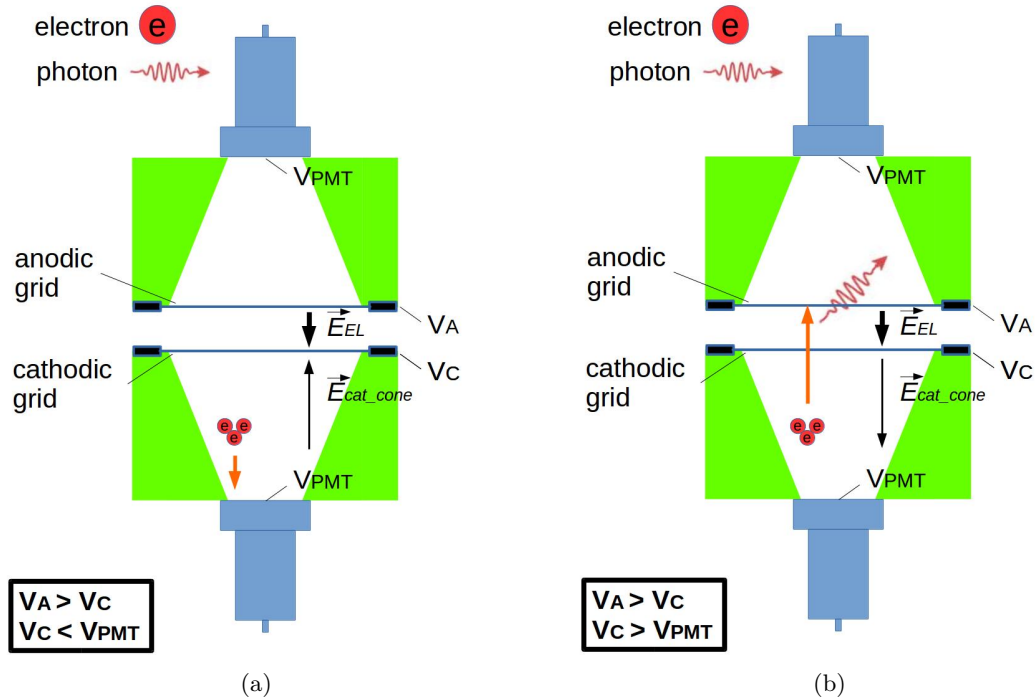


Figure 1.5: (a) Good configuration ($V_C < V_{PMT}$): drift fields pointing from PMT to the grids. Electrons created in the cone region will drift to PMT. This process does not create numerous photons as electron emission signal. (b) Bad configuration ($V_C > V_{PMT}$): drift fields pointing from grids to the PMT. Electrons created in the cone region will drift to EL region. This process creates plenty of EL photons which could look like an electron emission signal.

444 last $1.8 \mu\text{s}$ (450 sample) removed. This revised pulse area RQ is used in the main analysis instead in
 445 the PMT pulse area calibrations.

446 Series of pulse shaping parameters are also calculated. The time-weighted integral of the wave-
 447 form (RQ name: ‘wtimeN’) is used to study the skew and the kurtosis of the pulse. The time
 448 percentiles of the waveform are also calculated respect to the start time of the pulses. These time
 449 percentiles are the characteristic time differences of the pulse (RQ name: aft_tXX), which are useful
 450 to understand the pulse shape, pulse duration, and the center of mass of the pulse. These help the
 451 future signal selections and signal classifications which will be discussed in the following sections.

452 **Coinciding event building and coinciding pulse processing** The DAQ system records pulses
 453 in each PMT channel independently. An electron emission signal usually can produce enough quan-
 454 tities of photons that can be recorded by both PMTs. RQs of coinciding pulses between the two
 455 PMTs contain more useful information for electron emission signals. So, for each dataset we take,
 456 we do a coinciding event building and a coinciding event processing to help us separate electron
 457 emission signals from other background events, such as dark currents in one PMT.

458 The coinciding event building is undertaken by using the following method. This requires records
 459 in both PMTs taken within a short period of time. The PODs are put into coinciding POD groups;
 460 each includes not just two but all PODs that occur close in time.

461 First, to preserve only the useful part of the POD signal, for all single PODs, two segments of
 462 time are subtracted from the beginning and end of a POD to reduce the influence of the baseline
 463 fluctuation in the PMT. The default values for post-POD subtraction and pre-POD subtraction are
 464 1800 ns (450 sample) and 0 ns (0 sample). The time subtraction preserves 120 ns before the first pre-
 465 threshold crossing time, and 200 ns after the last post-threshold crossing time. The signal dominant
 466 time period of the POD locates between the two crossing times. The beginning and ending time of
 467 the remaining part of the POD are called the start (t_{start}) and the stop time (t_{stop}) of the POD.

468 Second, a POD search is performed between a certain segment of time before the start of a single
 469 POD and the same amount of time after the stop time of the POD. The value of additional segments
 470 of time is called the coinciding window width (CWW, RQ name ‘window_width’), which is $1.7 \mu\text{s}$, if
 471 not specified otherwise. If no other POD is found in this time range, no coinciding is identified for
 472 this particular single POD. If another POD is found in this time range, the two PODs are considered
 473 as connected.

474 Third, we group all connected PODs to form indivisible coinciding POD groups. A coinciding
 475 POD group contains all PODs that are connected to any element in the group, and cannot be divided
 476 to subgroups that match the same criterion.

477 Then, we check whether the coinciding POD group contains PODs from both PMTs. If so, we
 478 determine a coinciding event building is successful.

479 Last, we characterize coinciding pulse RQs which are formed from the coinciding pulse waveforms.
 480 A coinciding pulse waveform is defined as the addition of normalized pulse waveforms in each PMT

481 channel. The normalization is done by dividing the pulse waveform amplitude by the average SPHE
 482 pulse area in corresponding channel. A pulse characterization is performed for the coinciding pulses
 483 similar to the single POD processing.

484 Coinciding pulse RQs are the fundamental parameters for the electron emission signal analysis
 485 framework, which will be described later. Some commonly used coinciding pulse RQs are listed
 486 below:

- 487 • coinciding pulse area: RQ name ‘coin_pulse_areas_norm’, pulse area of coinciding pulse, mea-
 488 sured in phe.
- 489 • t_{XX} : RQ name ‘coin_pulse_areas_tXX’, time difference between the start of the coinciding pulse
 490 and the subsequent integrated pulse area reaching XX% of the coinciding pulse area, measured
 491 in ns. XX = 01, 05, 10, 15, 25, 50, 75, 85, 90, 95, 99.
- 492 • signal t_{01-99} duration (t_{01-99}): $t_{99} - t_{01}$.
- 493 • signal t_{10-90} duration (t_{10-90}): $t_{90} - t_{10}$.
- 494 • signal t_{25-75} width (t_{25-75}): $t_{75} - t_{25}$.
- 495 • signal t_{50} width (t_{50}).
- 496 • top-bottom asymmetry (TBA): TBA $\equiv (T-B)/(T+B)$, where T is the pulse area in the top
 497 PMT; and B is the pulse area in the bottom PMT.

498 **Random segment sampling** The event rates are checked by observing pulses in random samples
 499 of time during the operation. In each dataset, 10,000 random times are chosen. From each random
 500 time, total pulse areas in the preceding and the succeeding 10 μ s, 20 μ s, 50 μ s, and 100 μ s windows
 501 are calculated. These values of random samplings represent the average photon density in the
 502 detector in this dataset. They are compared to other segments of time to study light production in
 503 the detector.

504 1.5 PMT Calibration

505 PMT calibrations are performed for understanding the trigger efficiency, pulse amplitude, and pulse
 506 area of a SPHE for each PMT. SPHE trigger efficiency of a PMT, the probability of SPHE signal
 507 recording, determines the event recording efficiency. SPHE pulse amplitude of a PMT determines
 508 the capability of DAQ to record the full height of a sized pulse. SPHE pulse area of a PMT is the
 509 fraction denominator we use to calculate the counts of photon electrons in each pulse. Counts of
 510 photoelectrons in each pulse are roughly estimated by,

$$\# \text{ photoelectrons in a pulse [phe]} \sim \frac{\text{total pulse area}}{\text{single photon electron pulse area}} \quad (1.2)$$

511 Datasets that are used in the calibration are taken at vacuum and grid voltages V_T and V_B at
 512 0 kV. The detector in this condition will have the minimum influence from events from internal and
 513 external sources. Thus, a cleaner population of SPHE can be selected.

514 **PMT trigger efficiency** PMT trigger efficiency is estimated by comparing its trigger voltage
 515 (pre-threshold voltage) to its SPHE amplitude distribution. A simple Gaussian distribution is used
 516 to represent the distribution of SPHE amplitude. A fit range in the pulse amplitude of is chosen to
 517 avoid the influence from noise and overlapping of multiple photo electrons. The fit range is 12 mV to
 518 28 mV for the top PMT, and 22 mV to 38 mV for the bottom PMT. The range choices are $\sim \pm 8$ mV
 519 from the center peak values of the SPHE pulse amplitude. The trigger voltage of each PMT is
 520 compared to the survival function (complementary cumulative distribution function) of the fitted
 521 Gaussian distribution to get the trigger efficiency. Results of curve fittings are shown in Fig. 1.6.
 522 The figures show a close to unity trigger efficiency of both PMTs.

523 **PMT SPHE pulse area** PMT SPHE pulse area is calibrated with fitting the pulse amplitude
 524 and integrated area to a two dimensional Gaussian distribution. A fit range in the pulse amplitude
 525 and area is chosen to avoid the influence from noise and overlapping of multiple photo electrons
 526 this time. The fit ranges are 12 mV to 28 mV, 0 mV ns to 800 mV ns for the top PMT, and 22 mV to
 527 38 mV, 0 mV ns to 1000 mV ns for the bottom PMT. These chosen ranges contain the SPHE peaks
 528 of particular PMTs ,which is identified as the brightest feature above the noise and attributed to
 529 dark current. The used fitting function is,

$$z = A \exp \left(- \left(\frac{1}{2\sigma_x^2} ((x - \mu_x) \cos \theta - (y - \mu_y) \sin \theta)^2 + \frac{1}{2\sigma_y^2} ((x - \mu_x) \sin \theta + (y - \mu_y) \cos \theta)^2 \right) \right) \quad (1.3)$$

530 where x is the pulse area;
 531 y is the pulse amplitude;
 532 z is the total counts at each pulse area and amplitude, represented in the color scale;
 533 A is the amplitude of the fit;
 534 μ_x is the position of the center of the peak on x axis;
 535 σ_x is the standard deviation on rotated x axis;
 536 μ_y is the position of the center of the peak on y axis;
 537 σ_y is the standard deviation on rotated y axis;
 538 and θ is the rotated angle.

539 The mean values for pulse area and pulse amplitude are μ_x and μ_y . The standard deviation
 540 values for pulse area and pulse amplitude are $\sigma_x \cos \theta - \sigma_y \sin \theta$ and $\sigma_x \sin \theta + \sigma_y \cos \theta$. Results of
 541 these fits are shown in Fig. 1.7. Results from PMT calibrations are summarized in Table 1.4. Fitting

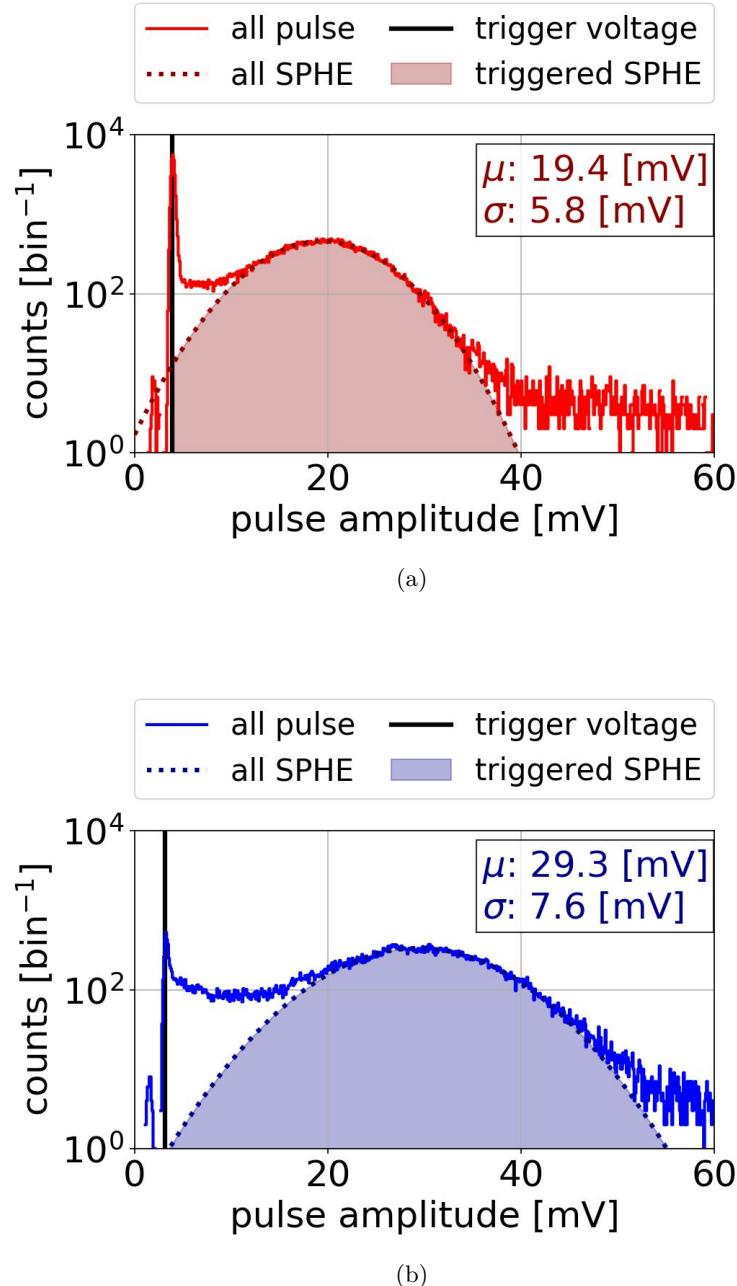


Figure 1.6: PMT pulse amplitude distribution: (a) top PMT (b) bottom PMT. Data were taken at 2018-03-12 11:41.

542 values of different dataset show an agreement within 1 % on the mean PMT single photon electron
 543 pulse area and pulse amplitude.

544 The values of SPHE pulse amplitudes are approximately 20 mV for the top PMT and 30 mV for
 545 the bottom. Thus, a naive estimation based on the dynamic range 1260 mV noted previously shows
 546 the DAQ system allows approximately 60 SPHEs to be simultaneously recorded by the top PMT
 547 without distortion of pulse shape, and 40 for the bottom PMT. This dynamic simultaneous photon
 548 recording range is large enough for record electron emission signal without pulse shape distortion in
 549 most situations.

550 Degrading of PMTs is not noticed during the run, even though the possibility of degrading of
 551 PMTs is discussed in their manual (Ref. [1]). However, since this effect is not observed during the
 552 tests. For consistency of studying, the same value for PMT SPHE pulse area is used through all the
 553 studies.

554 There are two revisions of these values of SPHE pulse area. In revision 1 (Rev1), the values used
 555 are 426 mV ns for the top PMT and 638 mV ns for the bottom PMT. This is from analyzing pulse
 556 area on datasets taken with the detector filled with xenon gas and grid voltages V_T and V_B higher
 557 than 0 kV. These datasets contains more multiple photon electron pulses and biased the estimation.
 558 In revision 2 (Rev2), data taken at vacuum condition with grid voltages V_T and V_B at 0 kV are used.
 559 The values used are 413 mV ns for the top PMT and 610 mV ns for the bottom PMT. Rev2 gives a
 560 better estimation on SPHE pulse area. SPHE pulse area is noted as PHE below.

time	PMT name	trigger voltage [mV]	trigger efficiency	pulse amplitude [mV]	pulse area [mV ns]
2018-02-3 13:21	top	3.762	0.997	19.4 ± 3.3	413 ± 132
	bottom	3.103	1.000	27.9 ± 4.6	607 ± 161
2018-03-12 11:41	top	3.853	0.996	19.3 ± 3.5	411 ± 130
	bottom	3.130	1.000	29.2 ± 5.1	607 ± 161
2018-05-15 12:03	top	3.713	0.997	19.4 ± 3.5	413 ± 131
	bottom	3.091	1.000	29.5 ± 5.4	615 ± 167
adopted value (Rev1)	top	-	1	-	426
	bottom	-	1	-	638
adopted value (Rev2)	top	-	1	-	413
	bottom	-	1	-	610

Table 1.4: PMT SPHE calibration.

561 1.6 Light Collection

562 *Gas Test* studies event-based primary scintillation light and EL light. Light collection efficiency is

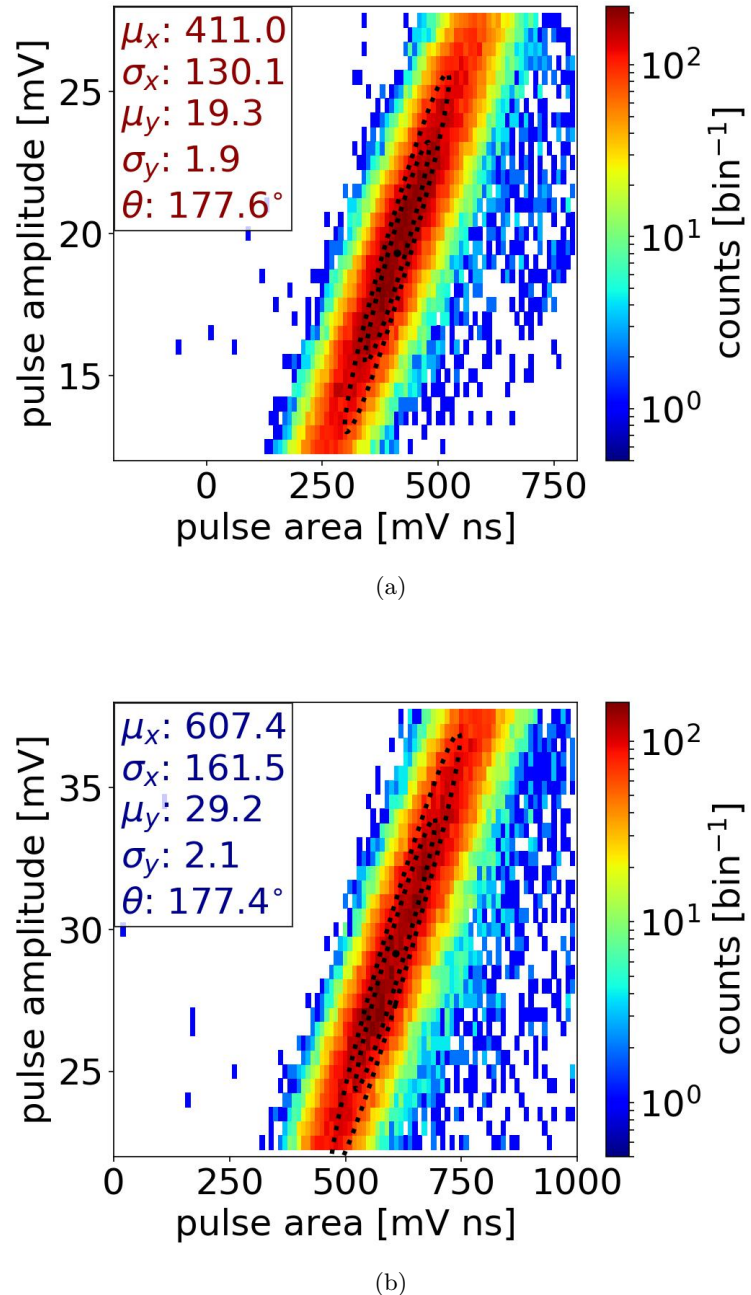


Figure 1.7: PMT SPHE pulse amplitude vs. pulse area distribution: (a) top PMT (b) bottom PMT. The black dot, and the dashed line are mean, 68 %, and 95 % contours of the Gaussian fits. Data were taken at 2018-03-12 11:41.

563 important to understand the overall sensitivity of the detector.

$$\text{light collection efficiency} = \frac{\# \text{ photoelectrons observed for an event}}{\# \text{ photon created during an event}} \quad (1.4)$$

564 Light collection efficiency includes geometric collection efficiency and PMT overall quantum effi-
 565 ciency. Geometric collection efficiency describes the efficiency of photon propagation to reach PMT
 566 photocathode surfaces, which includes photon propagation in the gas medium, photon reflection by
 567 the detector material surfaces, and photon propagation in PMT window materials. PMT overall
 568 quantum efficiency describes the efficiency of how many photons are absorbed by the photocathode
 569 surfaces and turn into measurable current or voltage signals.

570 **Geometric collection efficiency** Geometric collection efficiency is studied by photon propaga-
 571 tion simulation software Light Guide, as described in Ref. [5]. In the simulation software, a simplified
 572 *Gas Test* detector boundary with cylindrical symmetry is drawn to represent the real detector ma-
 573 terial surfaces. This simplified geometry includes the photocathode surfaces of PMTs, inner surfaces
 574 of the PTFE cones, and surfaces of the grid rings. In addition, each grid is represented by two
 575 planes of parallel wires with the same diameter and the same pitch distance as in the real detector.
 576 The two planes are parallel to each other and close in distance to represent two distinct sets of
 577 wires interlacing each other. Photon absorption and reflection, which takes into account the proba-
 578 bility of specular reflection and Lambertian diffusion reflection, are simulated at material surfaces.
 579 The empty space inside the simplified detector geometry is filled with a transparent or translu-
 580 cent medium. The simulation of photon propagation through the medium includes scattering and
 581 absorption effects.

582 The uncertainty of the reflectivity of detector surface materials has a major influence on the total
 583 light collection. Among these materials, PTFE reflectivity has the largest uncertainty reported, the
 584 value of which for xenon scintillation photons at room temperature are in the range of 0.4 to 0.75.
 585 This difference in reflectivity may be a result of different fabrication processes or different material
 586 density, as discussed in Ref. [6].

587 The geometric collection efficiency is evaluated as a function of (r, z) in the detector. To under-
 588 stand geometric collection efficiency at one specific location, 10^5 to 10^7 simulations of single photons
 589 are generated from this specific location. Each simulated photon is stepped either to transport
 590 through the detector medium or to interact with the detector surface materials. Each simulation
 591 ends when the simulated photon is absorbed by either the detector medium or detector surface ma-
 592 terials. The counts of photons reaching PMT photocathode surfaces are used to estimate geometric
 593 collection efficiency,

$$\text{Geometric collection efficiency} = \frac{\# \text{ photons reaching PMT photocathode surfaces}}{\# \text{ photons simulated}} \quad (1.5)$$

594 **PMT overall quantum efficiency** The overall quantum efficiency of a PMT includes (1) the
595 PMT photocathode quantum efficiency (QE), (2) the PMT electron collection efficiency, and (3) the
596 PMT electron gain.

597 The PMT photocathode QE is the probability per incident photon to produce a photoelectron.
598 For 175 nm xenon scintillation light, there is a $\sim 20\%$ probability for 2 photoelectrons to be produced
599 rather one, so called the double photoelectron effect. We use the term photons detected (PHD) to
600 refer to the number of photons that produced at least one photoelectron. The term PHE refers to
601 the number of photoelectrons produced at the photocathode. The photocathode quantum efficiency
602 for the top and bottom PMTs, as quoted by Hamamatsu, are 36.3% and 36.0%, respectively, for
603 175 nm light, see Table 1.1. The Hamamatsu QE does not account for the double photoelectron
604 effect; that is, it is the average number of photoelectrons produced per incident photon, different
605 from the average number of photons that produce a measurable signal per incident photon.

606 PMT electron collection efficiency is the probability that these output photoelectrons land on the
607 effective area of the first dynode; the mechanism of how the PMT works is described in Section 1.1.
608 PMT electron collection efficiency depends on the mechanical design of a PMT and the voltage
609 difference between the PMT photocathode and the PMT first dynode. The exact value of electron
610 collection efficiency of the PMTs used in *Gas Test* at their operating voltage are not measured. We
611 estimate PMT electron collection efficiency to be 90% based on measurement of other PMTs of the
612 same model at a higher PMT operating voltage, as described in Ref. [7].

613 PMT electron gain describes the multiplication process of the output photoelectrons in dynode
614 stages. The current that results from this multiplication process is translated to voltage using a
615 50Ω load resistor. The multiplication process amplifies the useful signal and eases the signal noise
616 selection. The voltage then is digitized by the DAQ, as described in Section 1.2. The digitized
617 voltage is the measured PMT signals. Observed signals are translated to units of PHE by dividing
618 out the mean SPHE area for each PMT. The coefficient of variation (CV, the ratio of the standard
619 deviation to the mean value) of PHE is $\sim 30\%$, as described in Section 1.5.

620 Therefore, to understand the spatial dependence of light collection efficiency in the ELD, we
621 start with 500 000 simulations of single photons every 5 mm in r and z dimension in the ELD, and
622 record the geometric collection efficiency of each location. This number is then multiplied by PMT
623 overall QE to obtain the total light collection efficiency. There are two light collection efficiency
624 estimation of two different grid wire configurations that we used for grid emission tests, labeled
625 grid configuration 1 (grid config. 1) and grid configuration 2 (grid config. 2). Run 4 to Run 9 use
626 grid configuration 1, and Run 10 to Run 17 use grid configuration 2. These two configurations are
627 identical everywhere else in the ELD except for the top grid wire pitches and diameters. Table 1.5
628 and Table 1.6 summarize the parameters in the simulation.

629 As expected, the geometric collection efficiency varies at different locations in the ELD, which
630 causes the light collection efficiency to vary, accordingly. The light distribution between the top

parameter		grid config. 1 Run 4-9	grid config. 2 Run 10-17
top grid	wire pitch [mm] wire diameter [μm]	2.5 100	5 150
bottom grid	wire pitch [mm] wire diameter [μm]	2.5 75	2.5 75
top/bottom cone (PTFE reflector)	cylinder 1 height [mm] cylinder 1 radius (frustum larger radius) [mm] frustum height [mm] cylinder 2 radius (frustum smaller radius) [mm] cylinder 2 height [mm]	1.17 65 98.8 32 10	1.17 65 98.8 32 10
top/bottom PMT	photocathode radius [mm]	32	32

Table 1.5: Light collection simulation geometry parameters

parameter	value
Xe (gas)	refraction index
	Rayleigh scatter length [m]
	absorption length [m]
Quartz (synthetic quartz)	refraction index
PTFE	reflectivity
	specular reflection ratio
	Lambretian diffusion reflection ratio
SS (SS304)	reflectivity
	specular reflection ratio
	Lambretian diffusion reflection ratio

Table 1.6: Light collection simulation material parameters

and bottom PMT also varies across the ELD. This light distribution helps discriminate the location where events happened. We use top-bottom asymmetry (TBA) to describe this light distribution, which is defined as:

$$\text{TBA} = \frac{\text{Top PMT light collection} - \text{Bottom PMT light collection}}{\text{Top PMT light collection} + \text{Bottom PMT light collection}}. \quad (1.6)$$

Results in Fig. 1.8 show the light collection efficiency and the TBA in the ELD. Locations that are in the top cone region usually have a positive TBA, and locations that are in the bottom cone usually have a negative TBA. TBA is close to zero in the EL region.

Among all different classes of events, our primary pulse of interest is electron emission events, which happen in the EL region. We estimate the light collection in this region with the same method mentioned before and finer binning. We start with 500 000 simulations of single photons every 2 mm in r dimension in the middle of the EL region. Results of the simulations are shown in Fig. 1.9.

641 Light collection efficiency in the EL region falls away at $r > 65$ mm, which is the inner radius of the
642 PTFE reflector cones. The average top and bottom PMT light collection efficiencies in the EL region
643 are ~ 0.0085 . The average TBA in the EL region is ~ 0 . The average total PMT light collection
644 efficiency in the EL region is ~ 0.017 . For most electron emission events in which photon production
645 is larger than 300, an average number of ~ 5 photoelectrons would be observed. Therefore, this light
646 collection efficiency is sufficient to allow us to detect electron emission events.

647 The uncertainty of PTFE reflectivity has a large influence on the total light collection, which is
648 shown in Fig. 1.10. Higher PTFE reflectivity results in a higher total light collection efficiency. The
649 actual value of reflectivity of the PTFE reflector cones has not been measured directly. We estimate
650 the actual PTFE reflectivity of xenon scintillation photons to be 0.4, according to the material
651 density .

652 1.7 Light production

653 The ELD measures primary scintillation photons and electroluminescence photons in gas. First, I
654 will introduce these two light production processes. Next, I will discuss the light production in noble
655 gas, e.g. xenon, which is the medium that the ELD normally operates in.

656 **Primary scintillation** Primary scintillation is the process in which photons are created directly by
657 energy deposition of external particle events. These photons have two sources: direct excitation, and
658 excitation from recombination after ionization. An external particle travels through the medium in
659 the ELD, transferring its energy to atoms in the medium, e.g. xenon, through exciting and ionizing
660 these atoms. The excited atoms will return to their ground states by emitting photons of series
661 energies corresponding to the energy level of the atoms, which is called relaxation of the excited
662 atom. These photons from direct excitation from external particles are the first source of primary
663 scintillation photons. The ionized atoms are not able to produce photons by themselves. However,
664 they can recombine with the electrons around them and form excited atoms, which deexcite in a
665 similar process as direct excited atoms, and emit photons simultaneously. These photons are the
666 second source of primary scintillation photons. The quantity of second source of primary scintillation
667 photons is dependent on the recombination process, which depends on properties of the atoms, and is
668 influenced by the detector environment, especially the electric field (or reduced electric field) on the
669 recombination site. A strong electric field forces electrons to quickly drift away from the ionization
670 site and reduce the probability of recombination, thus reducing the quantity of primary scintillation
671 light production.

672 **Electroluminescence** Electroluminescence (EL) is a phenomenon in which an electron drifts
673 through a strong electric field in a medium, collides with atoms in the medium, excites them which
674 will afterwards emit scintillation light. Since EL process is related to electrons in the medium, we

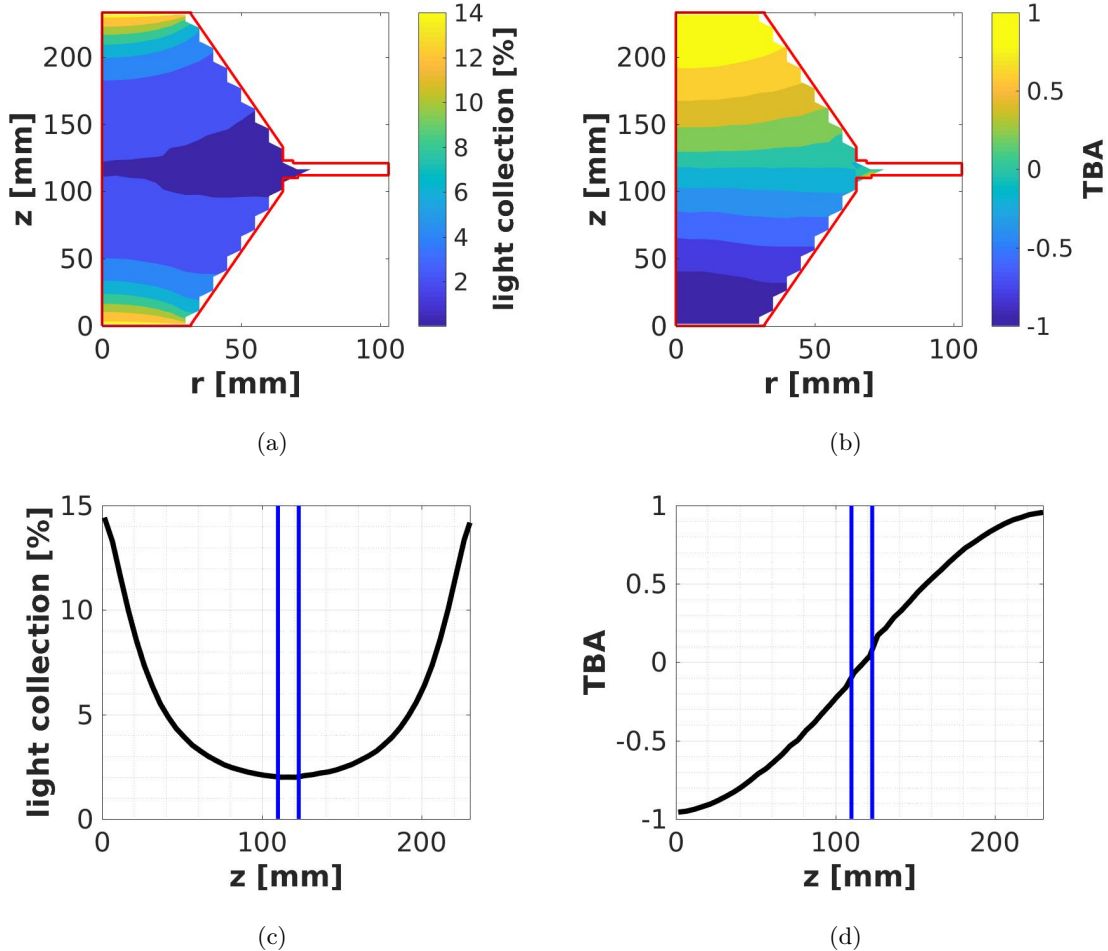


Figure 1.8: Light collection efficiency of (r, z) cross section in the ELD from simulation. (a) Total light collection efficiency. (b) Top-bottom asymmetry (TBA). (c) Total light collection efficiency at $r=0$. (d) TBA at $r=0$. The red solid curve is the edge of the active volume of the ELD. The blue solid curve is the edges of the EL region. This result uses configuration 1, PTFE reflectivity 0.40. $z=0$ is at the bottom PMT photocathode surface.

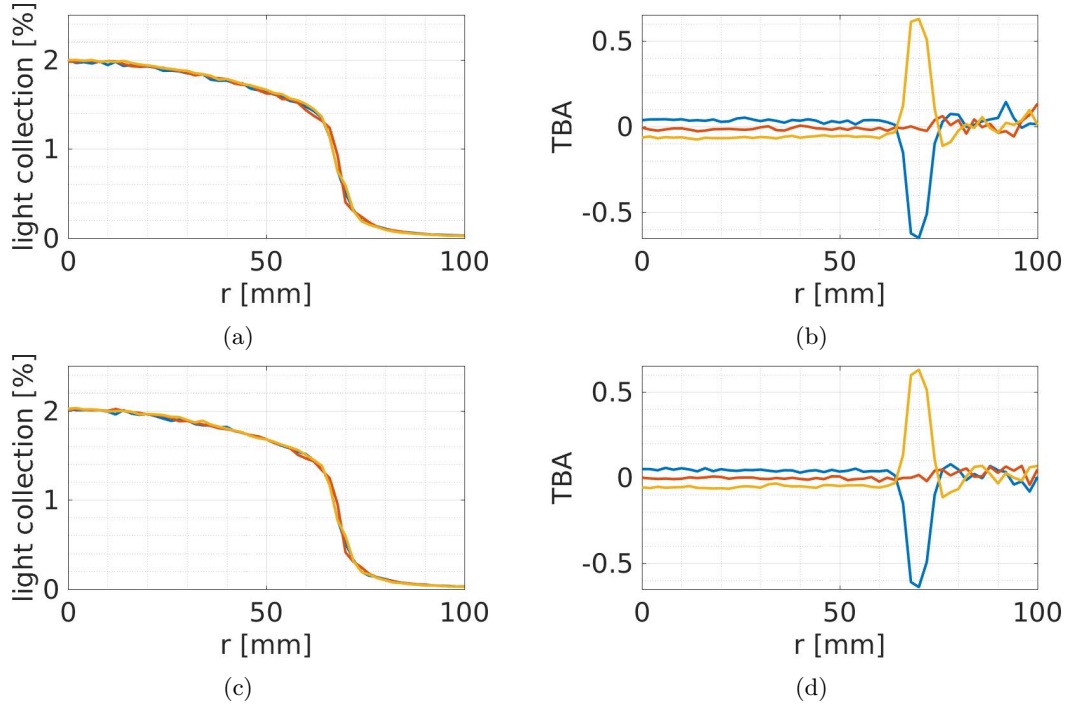


Figure 1.9: Light collection efficiency and TBA in the EL region in different grid configurations from simulation. (a) Total light collection efficiency in grid configuration 1. (b) TBA in grid configuration 1. (c) Total light collection efficiency in grid configuration 2. (d) TBA in grid configuration 2. The blue curve shows the value (light collection efficiency or TBA) as a function of r for fixed 2.09 mm below the top grid. The yellow curve shows the value as a function of r for fixed 2.09 mm above the bottom grid. The red curve shows the value as a function of r at the midpoint between the top and bottom grids. Light collection efficiency decreases and TBA has a sharp feature at $r=65$ mm, which is the inner diameter of the PTFE reflector cones. This result uses PTFE reflectivity 0.40.

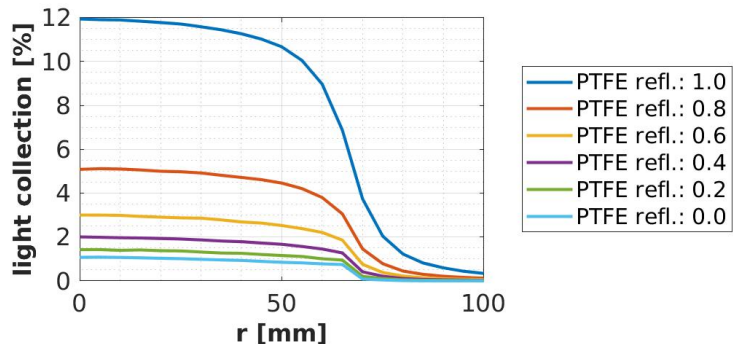


Figure 1.10: Light collection efficiency in the EL region with different PTFE reflectivity from simulation. Light collection efficiency decreases at $r = 65$ mm, which is the inner diameter of the PTFE reflector cones. This result uses grid configuration 1.

675 measure EL photons to study the electron production in the detector. The mechanism of EL is
 676 similar to primary scintillation; the electron gains energy from drifting through the strong electric
 677 field and simultaneously loses energy through exciting and ionizing medium atoms. Moreover, the
 678 ionization process are usually associated with electron multiplication (gas gain), which creates more
 679 electrons in the strong electric field region, and produces more EL scintillation light. The quantity of
 680 EL scintillation photons and the probability of electron multiplication, are related to the strength of
 681 reduced electric field of the medium. With proper strength of reduced electric field, EL can produce
 682 more photons than primary scintillation. Because of its association with electrons and its production
 683 quantity, EL photons are the most important signals measured in the ELD.

684 The primary scintillation photons are called S1, and the EL scintillation photons are called S2,
 685 because the primary scintillation photons are produced earlier than the other photons created by
 686 electroluminescence process of uncombined electrons. The same concepts of primary scintillation,
 687 as well as S1 and S2, are also used in liquid noble detectors, as described in Chapter. ??.

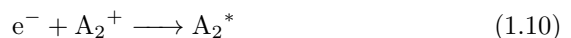
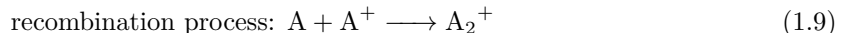
688 **Noble gas scintillation** For most noble gas atoms (A), e.g. neon, argon, krypton, and xenon, the
 689 scintillation process usually forms an intermediate excited excimer state (A_2^*). The emitted photons
 690 from the intermediate excimer state are almost monoenergetic, e.g. 7.1 eV (~ 175 nm) in xenon, which
 691 the medium is transparent to. Because of the existence of the intermediated excited excimer states, it
 692 creates appreciable quantity of monoenergetic photons from the deexcitation of these states. These
 693 features allow us to efficiently collect these monoenergetic photons with specialized devices, e.g.
 694 PMTs, and use these photons to study reactions between external particles and medium atoms.

695 The chemical processes of scintillation are:



696 where A is the noble gas atom; A^* is the noble gas excited state; A_2^* is the excimer state; γ is
 697 the monoenergetic photons from deexcitation of the excimers; and the low energy photons produced
 698 during the process are not shown.

699 The chemical processes of recombination are:



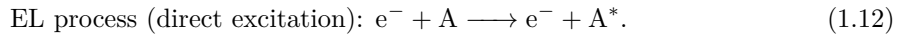
700 where A^+ is the noble gas ionized state; A_2^+ is the ionized dimer state; and the low energy photons
 701 produced during the process are not shown. The recombination process then leads to the same chan-
 702 nels as the primary scintillation, with monoenergetic photons as the output signals. These photons,

703 combined with photons from direct excitations, make primary scintillation light. The quantity of
 704 the monoenergetic photons is related to the reaction energy between external particles and medium
 705 atoms, and properties and physical environment of the medium (especially medium density and
 706 electric field).

707 These two primary scintillation processes rapidly occur in xenon, the duration of which is domi-
 708 nated by the excimers decay time. The excimers can be separated into two types, the singlet state
 709 (${}^1\sigma_u^+$, ${}^3\sigma_u^+$) and triplet state (${}^3\sigma_u^+$, 1_u), with separate decay times. The singlet state and the
 710 triplet state are known to be created from a three-body deconstruction of noble gas atom excited
 711 state ${}^2P_{1/2}$ state and ${}^2P_{3/2}$ state, which has a different initial quantity from the event. Because
 712 these creation processes are three body reactions, the creation rate of the these two states have
 713 strong dependence on the gas density of atoms. The decay time of both of these two states have
 714 a dependence on the gas density, as described in Ref. [9]. Some other materials also show that the
 715 decay time is very different between liquid noble gas and very dense noble gas. The decay time for
 716 the singlet state and the triplet state in liquid xenon are 4.3(6) ns and 22.0(20) ns, as measured in
 717 Ref. [10]. For dense xenon with pressure in the range of 2.7 atm to 32 atm, the decay time for singlet
 718 states varies from 15(3) ns to 5.5(10) ns. The decay time for triplet state is 96(5) ns in the same
 719 pressure range.

720 **think about should I take about ionization/scintillation ratio here?**

721 EL photons, produced in gaseous xenon from the energy-loss of fast-moving electrons, are one
 722 of the most important signals that we measure. This EL process is driven by the electrons gaining
 723 energy in the electric field. This chemical process is,



724 in which an electron directly excite a xenon atom. These excited-state atoms (A^*) then deexcite
 725 through the same chemical process as Eqn.1.7, Eqn.1.8 and emitted EL photons at a similar energy
 726 as scintillation photons.

727 The EL reduce photon production quantity (ratio of photon production quantity to gas density)
 728 per electron trajectory length of direct excitation has an approximately linear dependence on the
 729 reduced electric field (E_s/N), as described and summarized in Ref. [Santos1994, Fonseca2004,
 730 11, 12]:

$$\frac{dL_s}{dx} = a \frac{E_s}{N} + b, \quad (1.13)$$

731 where L_s is the reduced photon production quantity; x is the electron trajectory length; E_s is
 732 the electric field strength (at the scintillation site); N is the density of gas; a and b are constant

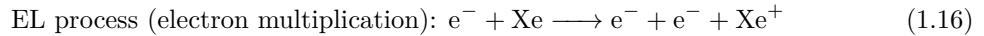
⁷³³ parameters, which are measured in Ref. [Fonseca2004, 12] to be:

$$a = 0.137(2) \text{ photon electron}^{-1} \text{ V}^{-1}, \quad (1.14)$$

$$b = -4.7(1) \times 10^{-18} \text{ photon cm}^2 \text{ electron}^{-1} \text{ atom}^{-1}. \quad (1.15)$$

⁷³⁴ The measurement also suggests that EL light is typically not produced below 3.4 Td¹, which is called
⁷³⁵ the EL threshold.

⁷³⁶ The EL process is usually associated with simultaneous electron multiplication. This process
⁷³⁷ describes an electric accelerated by electric field, collides with gas molecules, ionize them generating
⁷³⁸ additional free electrons. The chemical process is,



⁷³⁹ The probability of electron multiplication per electron per unit length is also quoted as the first
⁷⁴⁰ Townsend ionization coefficient (α), which depends on the strength of reduced electric field, as mea-
⁷⁴¹ sured in Ref. [Kruithof1940, Derenzo1974]. Conventionally, reduced first Townsend ionization
⁷⁴² coefficient is measured with E/p_0 instead of reduced electric field, where E is the electric field; p_0 is
⁷⁴³ pressure of the gas reduced to 0 °C. The reduced first Townsend ionization coefficient $\eta \equiv \alpha/E$ is also
⁷⁴⁴ frequently used. The measured reduced first Townsend ionization coefficient is shown in Fig. 1.11.

⁷⁴⁵ The duration of the EL process is related electron drift velocity (v), which also depends on reduced
⁷⁴⁶ electric field (E/n), as measured in Ref. [English1953, Pack1962, Brooks1982, Berghofer2004,
⁷⁴⁷ 13]. In the range of 5 Td to 25 Td, a naive linear fit from Ref. [Brooks1982] shows in xenon,

$$v [\text{mm } \mu\text{s}^{-1}] \approx 0.556E/n [\text{Td}] \quad (1.17)$$

⁷⁴⁸ Therefore, xenon is a good scintillation medium for its quantity of photon production and its
⁷⁴⁹ transparency to these photons. With its well-characterized quantities, we chose it as the major
⁷⁵⁰ operating medium for the ELD.

⁷⁵¹ 1.8 Signals

⁷⁵² A variety of processes can give rise to signals in the detector. Based on their source origin, signals
⁷⁵³ are separated to four different categories:

- ⁷⁵⁴ • electron emission (both from the grid wires and from the grid rings)
- ⁷⁵⁵ • particle radiation from radioactive materials (both from inside and from outside the ELD),
- ⁷⁵⁶ • cosmic ray,

¹A Townsend, or Td, is defined as $1 \text{ Td} = 10^{-21} \text{ V m}^2 = 10^{-17} \text{ V cm}^2$.

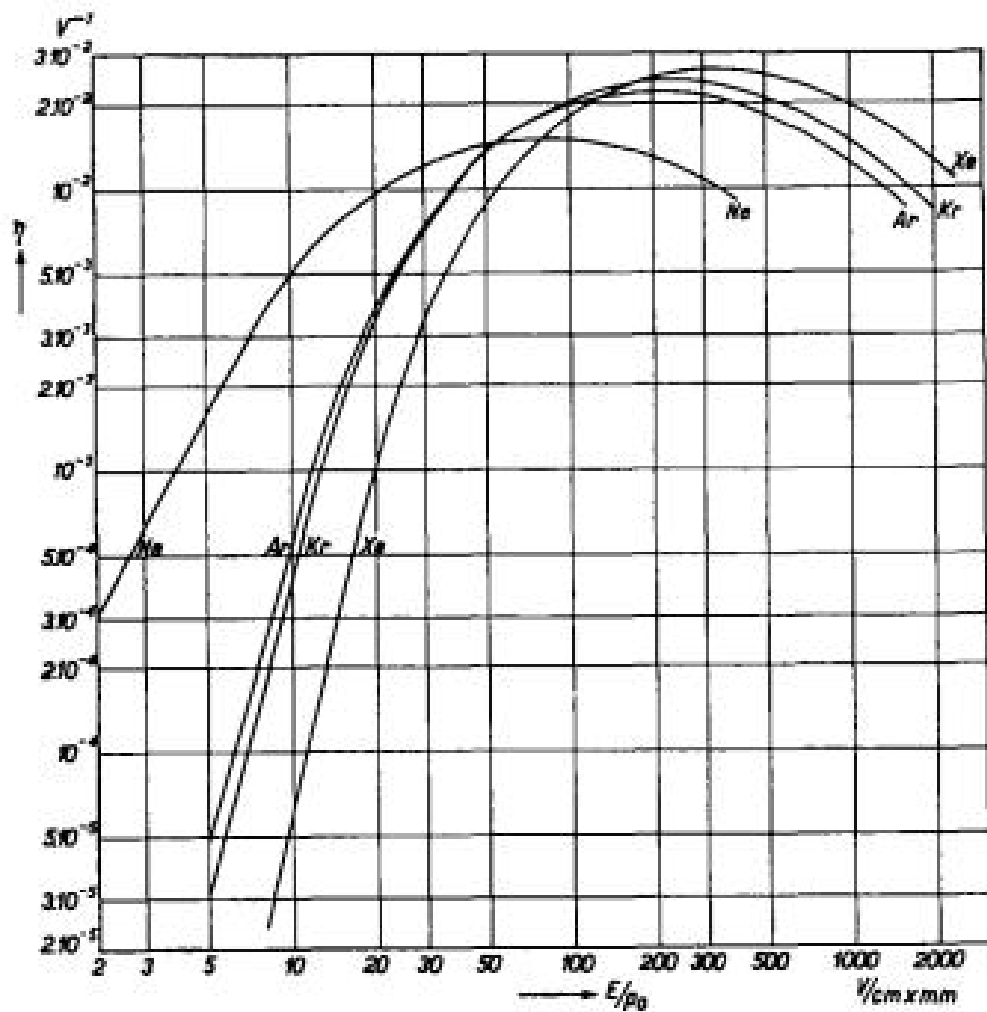


Figure 1.11: The reduced first Townsend ionization coefficient $\eta \equiv \alpha/E$ for neon, argon, krypton, and xenon, from Ref. [Kruithof1940].

- 757 • and other miscellaneous sources, which include:
- 758 – electronic noise
- 759 – PMT dark current,
- 760 – PMT afterpulsing,
- 761 – PTFE cone reflector fluorescence,
- 762 – Cherenkov radiation (in PTFE cone reflectors and PMT windows)
- 763 – discharge, as in a short-lived plasma in the medium, i.e., breakdown.

764 **1.8.1 Electron emission**

765 Electron emission signals, especially those from the grid wires, are our signals of interest. A cartoon
766 of the physical process and an example waveform of electron emission signals are shown in Fig. 1.12.
767 An electron leaves the cathodic electrode from various types of emission processes. After the electron
768 left the wire surface, the high electric field around the cathodic wire will quickly energize the electron.
769 The high energy electron then ionizes and excites the atoms around it. The process in which more
770 drifted electrons are produced is called electron multiplication; since in this particular case, the
771 electron multiplication process happens near the cathodic electrode, it is also called the cathodic gas
772 gain. In the high electric field region around the cathodic wire, more EL light is produced per unit
773 of time compared to a lower electric field region. This is the cause of the “peak” at the beginning
774 of the electron emission signal. Next, these electrons drift to the anodic electrode according to
775 the voltage difference between the two grids, producing EL light along the drift. This process is
776 responsible for the majority of EL light seen in the electron emission signal. There is a clear start
777 and stop time for the electron emission signal. The time difference between the two times (electron
778 emission signal duration) is approximate to the duration of this drift. Then, drifted electrons get
779 close to the high electric field region around the anodic electrode. Because of the high electric field,
780 drifted electrons also go through a similar electron multiplication process in this high electric field
781 region, which is also called the anodic gas gain. This process also creates more electrons and a
782 higher production rate of EL light, resulting in a “peak” at the ending of the electron emission
783 signal. The peak at the end of the signal is lower than the peak at the beginning of the signal. This
784 is resulting from the dispersion of the arrival times of drifted electrons on anodic electrode, because
785 the different microscopic trajectory each drifted electron takes to reach the anodic electrode. The
786 different arrival times of the drifted electrons cause the final increment of EL light production from
787 different electrons do not happen coincidentally. This lowers the height of the peak at the ending
788 of the electron emission signal. Another reason for the difference in height of the peaks is because
789 the electric field on the anodic wire is smaller than that of cathodic wire with regard to the wire
790 diameter of the anodic wire are larger, which therefore results in a smaller production of EL light.

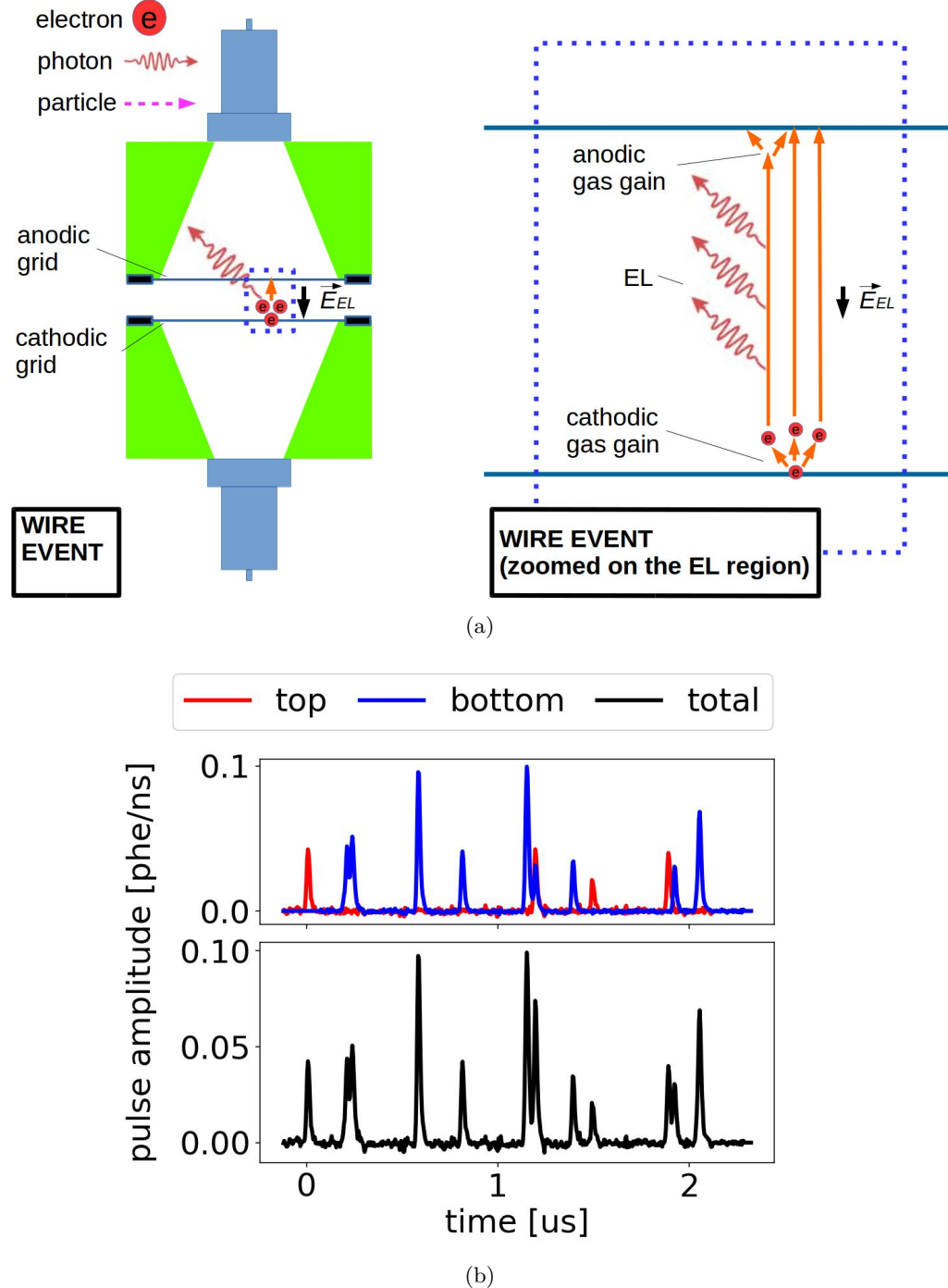


Figure 1.12: *Gas Test* electron emission event from grid wires. (a) Cartoon of the process. (b) An example waveform. Data were taken at 2017-12-8 14:02, with grid voltages V_T and V_B at +6 kV and -6 kV, operating gas density at 0.137 mol L^{-1} . See text for details.

791 Of the features described above, the most important features of the electron emission signal is
 792 the EL duration. The other signal shape features, such as the early and late gas gain peaks, are not
 793 apparent because the light collection efficiency is not high enough. The EL duration is approximately
 794 equal to the duration of electron drift between the two electrodes. The deviation of electric field
 795 between the two electrode is much smaller than its average value. Therefore, the drift duration can
 796 be roughly estimated by,

$$\text{drift duration} = \frac{\text{distance between two electrodes}}{\text{drift velocity at the average electric field between two electrodes}} \quad (1.18)$$

797 The other important feature of the electron emission signal is the quantity of its EL production.
 798 EL light production in the major part of electron emission signal is uniform, except for at the
 799 beginning and at the ending of the signal, because the deviation of the drift electric field is small.
 800 Since the electron multiplication around the cathodic wires happens early in the process before the
 801 major EL light production, the total counts of photons created in an electron emission signal can be
 802 estimated as,

$$\# \text{ EL photons} \approx \# \text{ EL photons per drifted electron} \times \text{cathodic gas gain} \quad (1.19)$$

803 where the number of EL photons per drifted electron and the cathodic gas gain are estimated below.

804 The number of EL photons per drifted electron and the cathodic gas gain are related to the
 805 reduced electric field in the EL region and surface reduced electric field on the cathodic wire. The
 806 value of both reduced electric field can be derived from the gas density and the electric field, which can
 807 be estimated from the voltages, wire diameters and wire pitches of the two grids. The electrostatic
 808 solution of the electric field in the ELD is solved by COMSOL, as described in Appendix ???. The
 809 results of the electric fields in the EL region (drift fields) and the average surface electric fields vs.
 810 ΔV_{T-B} are shown in Fig. 1.13a. The woven pattern of the grid cause that the surface electric field
 811 in the middle of the wire between two woven knots are higher than average by $\sim 16\%$, which is also
 812 discussed in Appendix ???. The average number of photon production per EL distance is a known
 813 function of reduced electric field, as discussed in Section 1.7.

814 With the known surface reduced electric field, electron multiplication (cathodic gas gain) is
 815 studied using gas simulation softwares. A simple geometry is build and meshed in GMSH, as
 816 described in Ref. [14]. This software is capable of defining 3D finite element mesh, which interfaces
 817 with softwares like ElmerSolver and Garfield++ to solve the electric field in a defined geometry.
 818 Fig. 1.14a shows the defined geometry. This geometry includes a thin cylindrical surface in the
 819 center representing the grid wire as the surface emitting electrons, and a thick cylindrical surface
 820 outside representing the cut-off distance of electron multiplication. This cut-off distance is chosen
 821 to be sufficiently long so that the electric field beyond this distance is too small to allow most

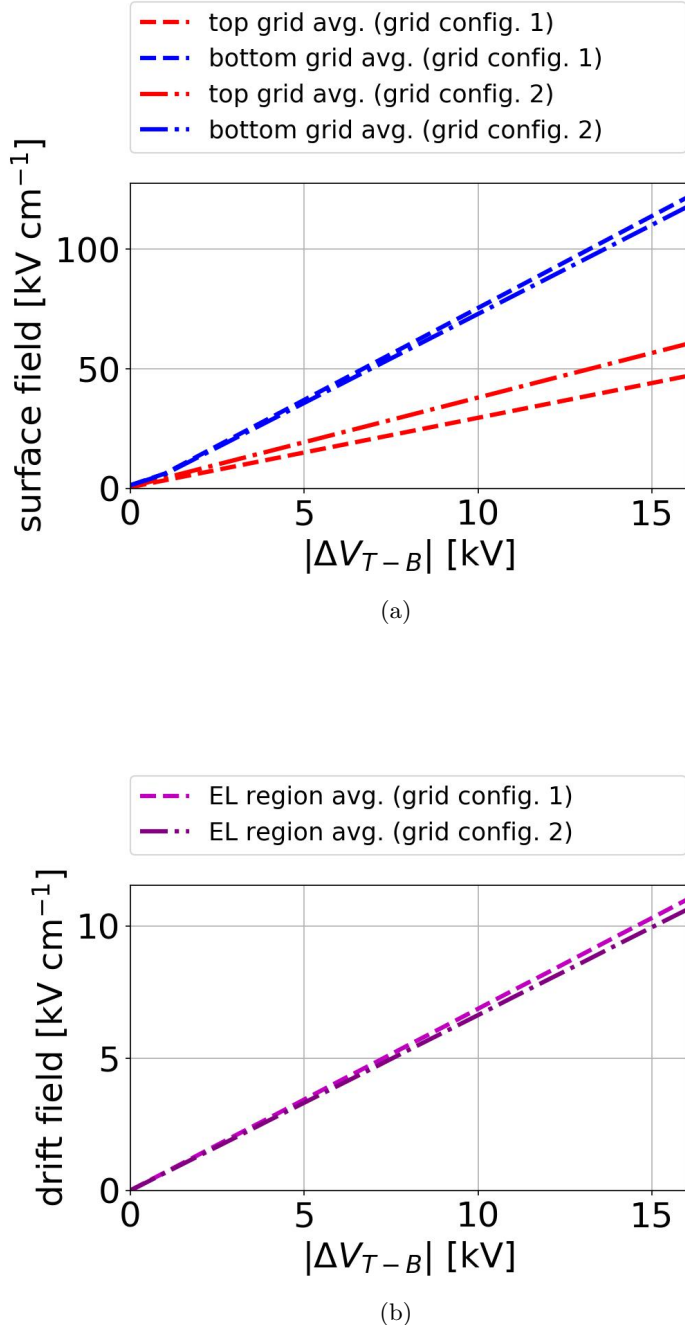


Figure 1.13: *Gas Test* detector electric field. (a) *Gas Test* wire surface electric field vs. ΔV_{T-B} for the top and bottom grid in different grid configurations. (b) *Gas Test* EL region drift electric field vs. ΔV_{T-B} in different grid configurations.

822 of the electron multiplication. The diameter of the two cylinders are $75\text{ }\mu\text{m}$ and 1 cm . Voltages
 823 are assigned to two cylinders to create a chosen electric field on the surface of the wire. Next, the
 824 electric field map in this full geometry is solved by Elmer, as described in Ref. [15, 16]. Then, the gas
 825 simulation under such electric field map is done with Magboltz in Garfield++ interface, as described
 826 in Ref. [17, 18]. These softwares implement light yield and charge yield, also known as the photon
 827 and electron production, for electrons moving in a gas medium as a function of reduced electron
 828 field. By including the electric field map and choosing the corrects gas density, these softwares are
 829 able to simulate the photon and electron production with an electron that initiate from the wire
 830 surface.

831 An example of electron multiplication simulation in the simple geometry is shown in Fig: 1.14b.
 832 As the electron moves further away from the wire surface, both light production and electron pro-
 833 duction reduce. Results of the counts of electron multiplication vs. surface electric field at different
 834 gas density is shown in Fig. 1.15. The number of collected EL photons of the electron emission
 835 signal signals are shown in Fig. 1.16. Together with the EL duration, this number of collected EL
 836 photons are the important features of electron emission signal signals that we used in the signal
 837 classification.

838 Therefore, electron emission signals have a known EL duration and EL photons production depen-
 839 dence on the detector operating gas density and $\Delta V_{\text{T-B}}$. We use these two important characteristics
 840 of signals to distinguish electron emission signals in the future signal classification.

841 1.8.2 Particle radiation

842 Particle radiation is the high energy particle originating from radioactive decay of unstable atoms in
 843 materials inside and outside the detector. The high energy particle enter the detector and deposit
 844 energy there through different processes. A high energy photon (gamma radiation) loses energy
 845 through thermal elastic scattering, photoelectric process, Compton scattering, and other particle
 846 energy loss processes; A high energy charged particle, e.g. electron (beta radiation), ${}^4_2\text{He}$ (alpha
 847 radiation), predominately loses it energy through ionizing atoms in detector materials, as described
 848 in Ref. [19]. These processes produce excited xenon atoms and free electrons, which later produce
 849 primary scintillation and EL photons. The primary scintillation photons (S_1) are collected and
 850 seen immediately. The EL photons, on the other hand, resulting from electrons drifting in the high
 851 electric field region in the detector, are usually produced later.

852 A high energy gamma event can enter the ELD since its energy loss in detector skin materials is
 853 small. The photon attenuation length, which characterizes how far a photon can go, usually decrease
 854 as we have denser materials, higher average atomic mass in the materials, and lower incident particle
 855 energy. The photon attenuation length in xenon is shown in Fig. 1.17. Along photon attenuation,
 856 high energy electrons can be produced from gamma radiation through some kind of energy loss
 857 process, like Compton scattering, Auger electron emission. These high energy electrons can be

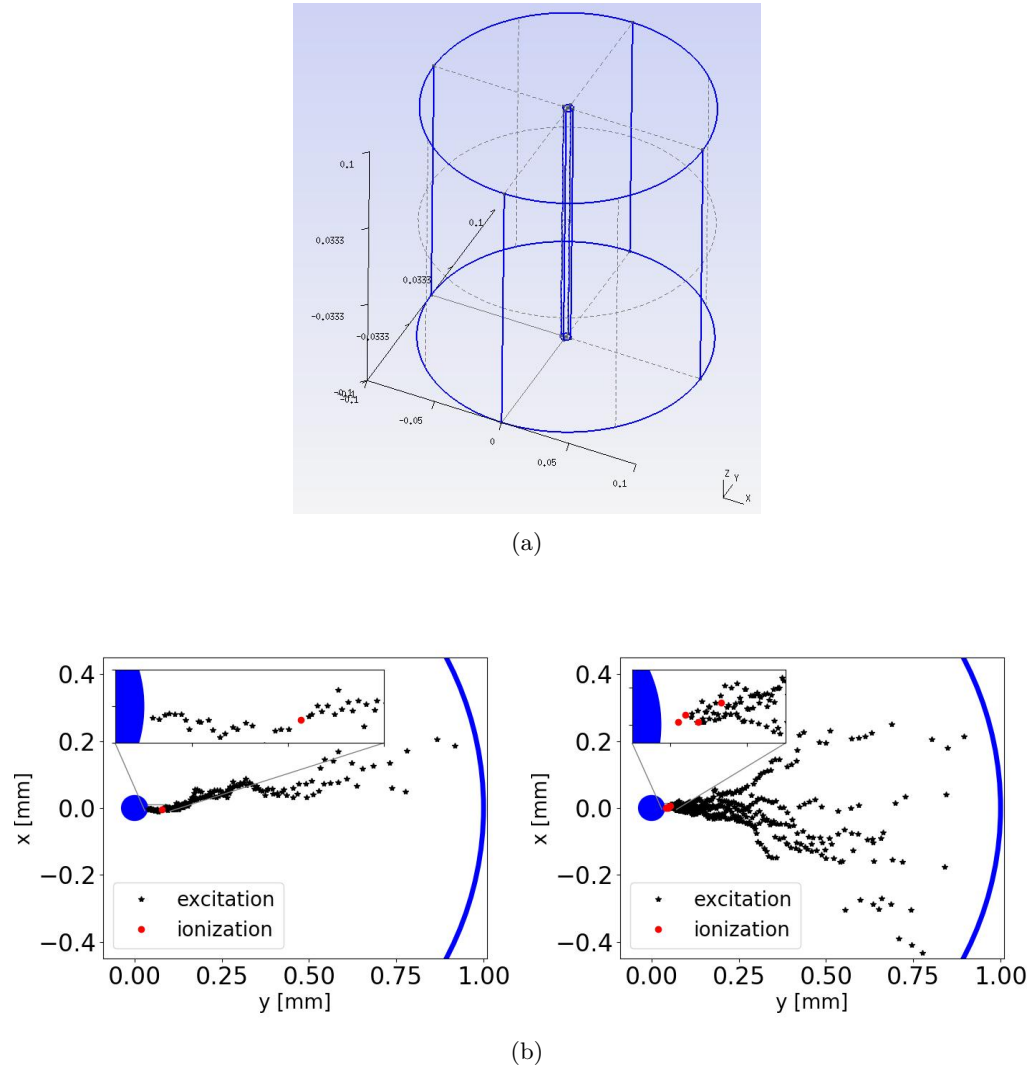


Figure 1.14: A 3D simulation of an electron drifting in an axial symmetric electric field in xenon gas. (a) Geometry defined in GMSH (unit in cm) [14]. Electrons are emitted at one point from the wire in the center. (b) Example simulation results, which is taken at operating gas density 0.137 mol L^{-1} ($T = 295 \text{ K}$, $P = 3.3 \text{ bara}$), showing the excitation and ionization sites. The blue curves are the boundary of the outer edge of simulation (diameter : 2 mm) and the wire surface (diameter: $75 \times 10^{-3} \text{ mm}$). Left: a simulated event with a single ionization site. Right: a simulated event with four ionization sites. This simulation is conducted with Elmer and Garfield++, as described in Ref. [15–18].

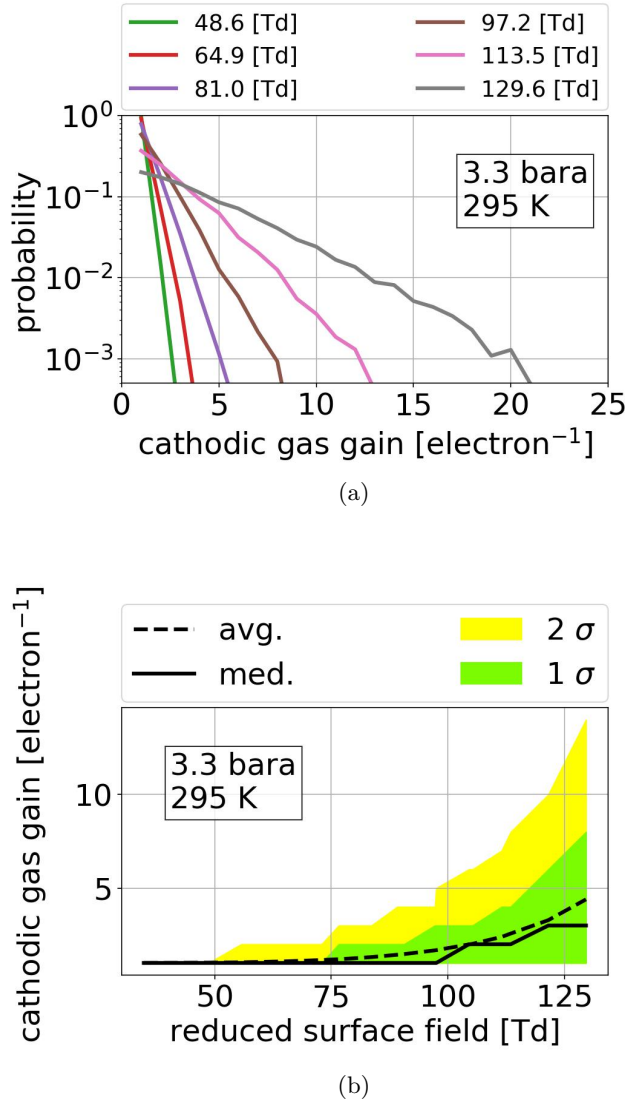


Figure 1.15: Simulated cathodic electron gas gain vs. reduced surface electric field. (a) Simulated cathodic gas gain probability distribution in different reduced surface electric fields. (b) The average, median, 1σ band (15.9 % to 84.1 %), and 2σ band (2.3 % to 97.7 %) of cathodic gas gain vs. the reduced surface electric field. Simulation is taken at operating gas density 0.137 mol L^{-1} ($T = 295 \text{ K}$, $P = 3.3 \text{ bara}$).

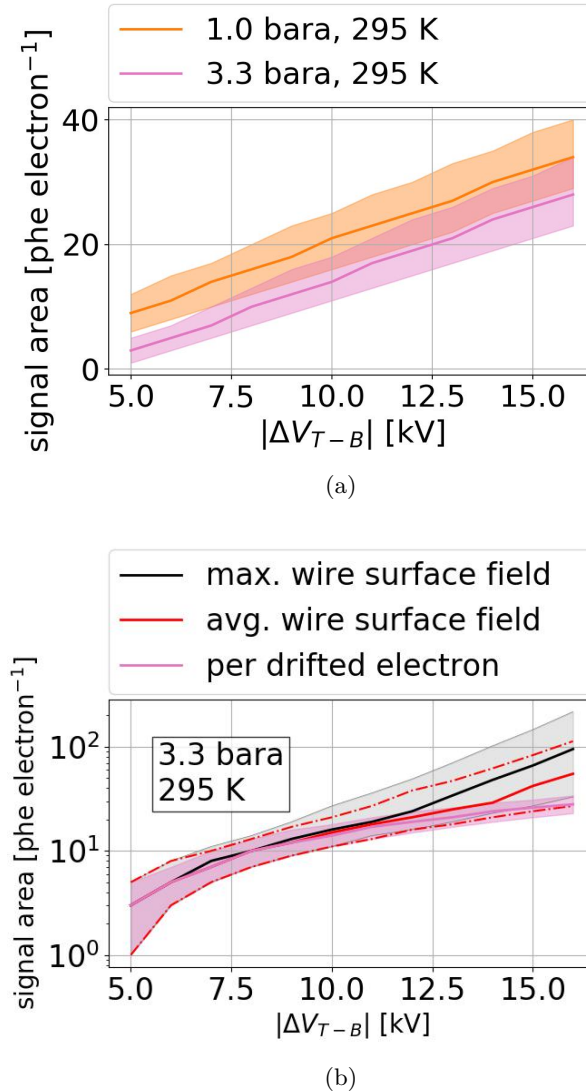


Figure 1.16: Simulated signal areas vs. ΔV_{T-B} . (a) Simulated signal area of a single drifted electron from the bottom grid at different gas densities. (b) Simulated signal area of an electron generated at different locations on the bottom grid. The black line corresponds to locations with maximum electric field on the grid. The red line corresponds to locations with average electric field on the grid. The green line shows the simulated signal area of a single drifted electron. Simulation is taken at operating gas density 0.137 mol L^{-1} ($T = 295 \text{ K}$, $P = 3.3 \text{ bara}$). The solid lines are the medians. The dashed lines, color shaded bands are 1σ bands (15.9 % to 84.1 %), respectively.

produced inside the ELD, deposit its energy, and raise signals in the detector. The energy deposition length depends on the material, especially its density and its average atomic mass, and the energy of the incident particle. Similar to the photon attenuation process, denser material, higher average atomic mass, and lower incident particle energy usually results in smaller energy deposition length. The energy deposition length in xenon is shown in Fig. 1.18. For an electron with energy in the range of 10 keV to 1000 keV, which is the common energy for beta radiation, the continuous slowing down approximation range (CSDA range), also known as the average path length traveled by the charged particle (electron), is in the range of $6 \times 10^{-4} \text{ g cm}^{-2}$ to 1 g cm^{-2} , corresponding to $1 \times 10^{-5} \text{ cm}$ to $2.0 \times 10^{-2} \text{ cm}$ with xenon gas density at 0.137 mol L^{-1} ($18.0 \times 10^{-3} \text{ g cm}^{-3}$). The number of free ionization electrons in this event is associated with the energy-loss of the incident particle. During the measurement, a population associated with xenon K shell X-ray (K_{α} : 29.8 keV, K_{β} : 33.6 keV, from Ref. [Dulieu2007, TabRadv8]) is observed to be one of the byproduct of particle radiation energy loss process, confirming that this type of signal is associated with external radiation.

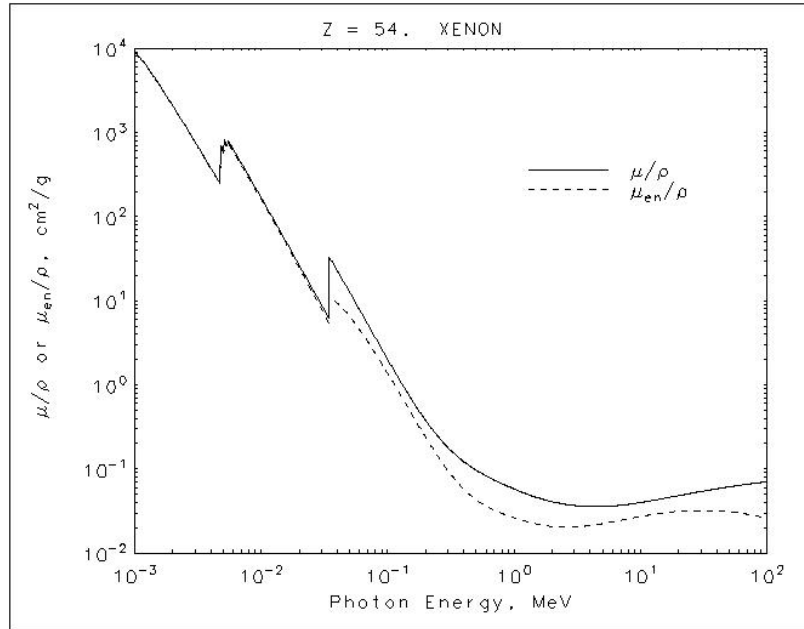


Figure 1.17: Attenuation length of photon in xenon, from Ref. ??.

A high energy external beta radiation, however, is less likely to enter the ELD compared to high energy gamma radiation because the beta radiation penetration length (approximate to the material CDSA range) is shorter than gamma radiation. Since the electron CDSA range is small compared to the thickness of xenon gas skin outside the ELD, with addition stopping power from dense PTFE reflector cone, the beta radiation would be stopped before it enters the ELD.

According to the location of energy deposition site, the high energy particle from radiation

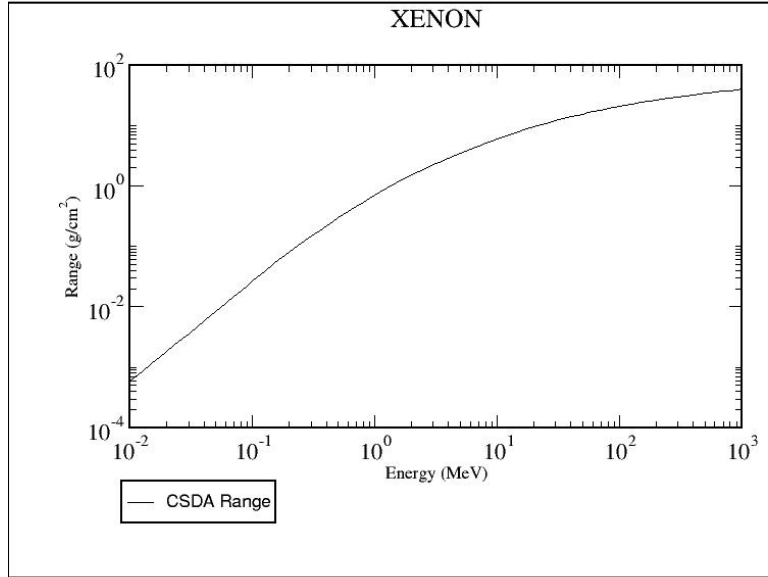


Figure 1.18: CSDA range of electrons in xenon, from Ref. ??.

produce different look of signals, which will be discussed separately.

Anode cone event Anode cone events are the particle radiation events which have energy deposition location in the PTFE reflector cone close to the anodic grid side (anode cone). A cartoon of the physical process and an example waveform of anode cone event, as well as two zoomed plots of the waveform in different parts of the process, are shown in Fig. 1.19. The cartoon part A in Fig. ?? shows an external particle entering the anode cone region and deposit energy there. This process produce scintillation photons, the signal of which are collected and seen immediately, shown in Fig. 1.19c. The primary scintillation signal normally has a TBA (top-bottom asymmetry) heavier in the anode side PMT than the cathode side, indicating this photon signal is produced in the anode cone (top cone in this case). The free electrons drift to the anodic grid according to the electric field in the anode cone . Even though the electric field in the cone region is too small to produce large quantity of EL light during electron drift, when these electrons get close to the anodic grid wire, the electric field around the anodic grid wires are big enough to produce EL light. This is the source of the secondary photon signal, which follows the preceding signal after the amount of time that it took electron to drift. The cartoon part B in Fig. 1.19a shows this process, and Fig. 1.19d shows the corresponding part of the signal. The pulse shape of the secondary photon signals has a comparably slower rising and falling edge at the beginning and the ending of it. It also has a higher TBA because EL around the anode wire primarily happens above the anodic wire. The bottom PMT is in the shadow of grid wires when the top PMT is not. This difference causes a ratio of ~ 2

896 increment on light collection ratio between the top PMT and the bottom PMT. These characteristic
 897 signatures are useful for veto large-area anode cone events. However, when their signal area get
 898 smaller (probably because of a lower energy deposition of external particles), it becomes difficult to
 899 find these signals by their shape. Therefore, a signal selection based on preceding signal is conducted
 900 to find the secondary signal from the primary scintillation signal. The time separation between these
 901 two signal is estimated by the known measured electron drift velocity in gaseous xenon, as described
 902 in Ref. ???. Electron drift velocity in gaseous xenon is approximately $0.556 \text{ mm } \mu\text{s}^{-1} \text{ Td}^{-1} \text{ E/N}$ for
 903 reduced electric field (E/N) in the range of 5 Td to 25 Td. The maximum separation time for this
 904 detector at xenon gas density 0.137 mol L^{-1} , top grid voltage V_T in the range of +4 kV to +8 kV is
 905 approximately $85 \mu\text{s}$ to $75 \mu\text{s}$. The value of this maximum separation time decreases as decreasing
 906 the operation pressure in the detector. The value of maximum separation time drives the choice of
 907 $100 \mu\text{s}$ preceding signal selections of this type of signals.

908 **Cathodic cone event** Cathode cone events are the particle radiation events which have energy
 909 deposition location in the PTFE reflector cone close to the cathodic grid side (cathode cone). A
 910 cartoon of the physical process and an example waveform of cathode cone event are shown in
 911 Fig. 1.20. Similar to anode cone events, this process produce scintillation photons. However, the
 912 ionization electrons produced drift to cathode PMT. Therefore, EL light typically is produced during
 913 along their trajectories because the electric field in such region is much lower than the EL threshold.
 914 The primary scintillation signal normally has a TBA heavier in the cathode side PMT than the
 915 anode side PMT, indicating this photon signal is produced in the cathode cone (bottom cone in this
 916 case), as expected.

917 **S1 S2 event in the cathode corner** S1 S2 events in the cathode corner (cathode corner events)
 918 are the particle radiation events which have energy deposition location either outside EL region and
 919 very close to the cathodic grid or in the corner between the cathodic grid and the cathodic cone.
 920 A cartoon of the physical process and an example waveform of cathode corner event are shown in
 921 Fig. 1.21. Similar to anode cone events, this process produce scintillation photons, which is shown
 922 in Fig. 1.21a (left) and the waveform of which is shown in the first $0.3 \mu\text{s}$ in Fig. 1.21b. Since the
 923 free electrons produced in this event is really close to the cathodic grid, according to electrostatic
 924 study using COMSOL software described in Ref. [20], these electrons drift to cathodic grid, pass
 925 it, then drift in the EL region, the process of which produces EL photons along the trajectories of
 926 the electrons, and finally land on the anodic grid. This EL light production process is illustrated in
 927 Fig. 1.21a (right), which corresponds to the waveform after $0.5 \mu\text{s}$ in Fig. 1.21b. The static electric
 928 field from COMSOL solution is shown in Fig. 1.22. Both the primary scintillation signal and the
 929 secondary EL signal has a balanced TBA, indicating these photon signals are produced either in or
 930 really close to the EL region.

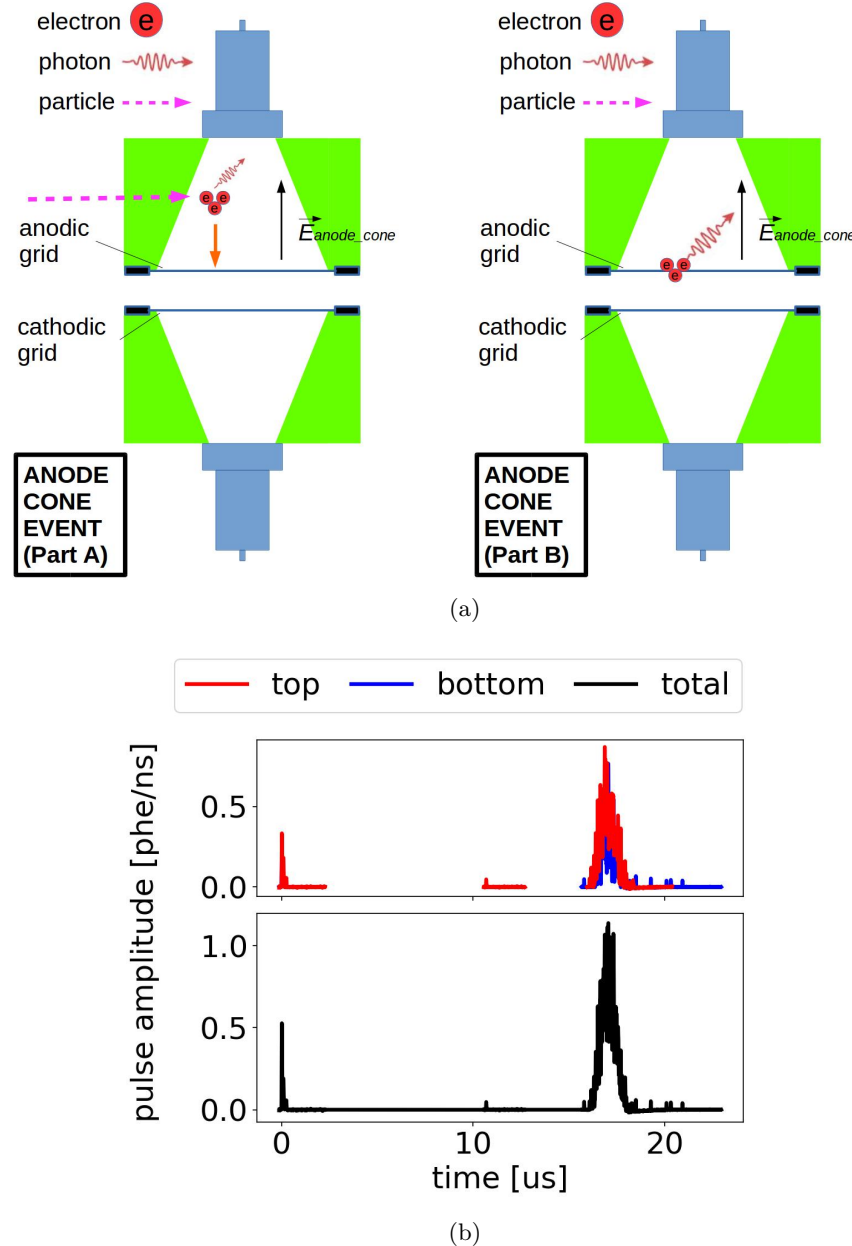


Figure 1.19: *Gas Test* signal: anode cone event. (a) Cartoon of the process. Left: Primary scintillation light ionization electrons are produced from the particle interaction, and the ionization electrons drift to the anodic grid (part A). Right: EL light is produced in the high electric field region around the anodic grid wires (part B). (b) An example waveform of an anode cone event. Data were taken at 2017-12-8 14:02, with grid voltages V_T and V_B at +6 kV and -6 kV, operating gas density at 0.137 mol L^{-1} .

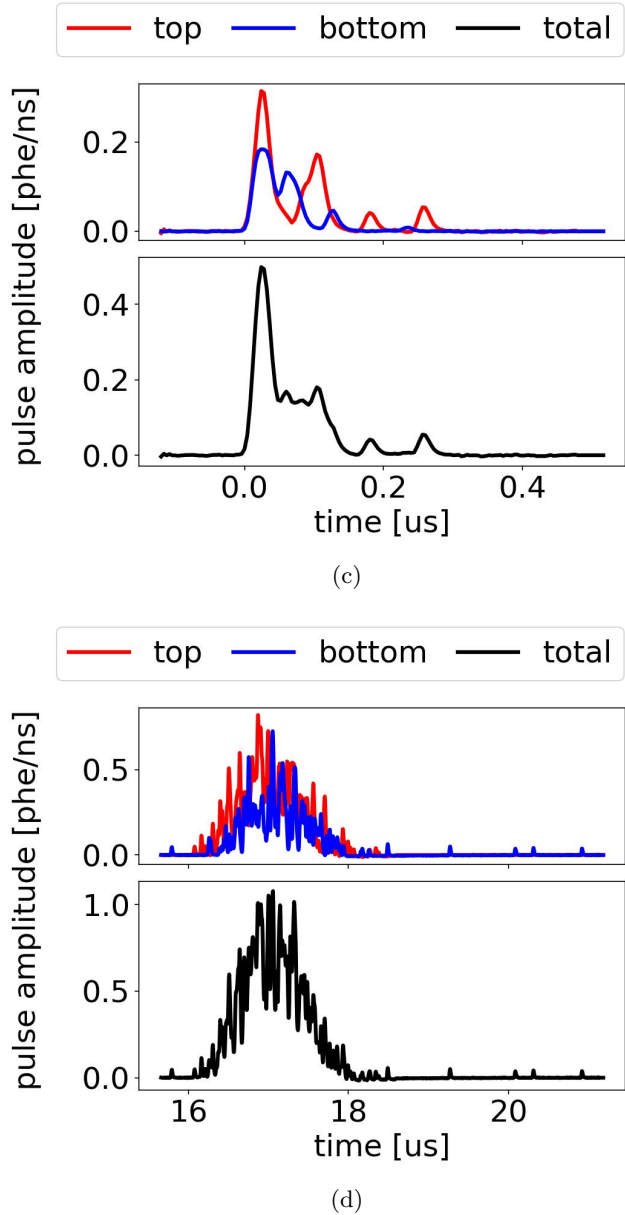


Figure 1.19: *Gas Test* signal: anode cone event (cont.). (c) An example waveform of an anode cone event, zoomed in the range of $0 \mu\text{s}$ to $0.5 \mu\text{s}$, which shows the primary scintillation light (cartoon part A). (d) An example waveform of an anode cone event, zoomed in the range of $15 \mu\text{s}$ to $21 \mu\text{s}$, which shows the EL light produced around the anodic grid wires (cartoon part B).

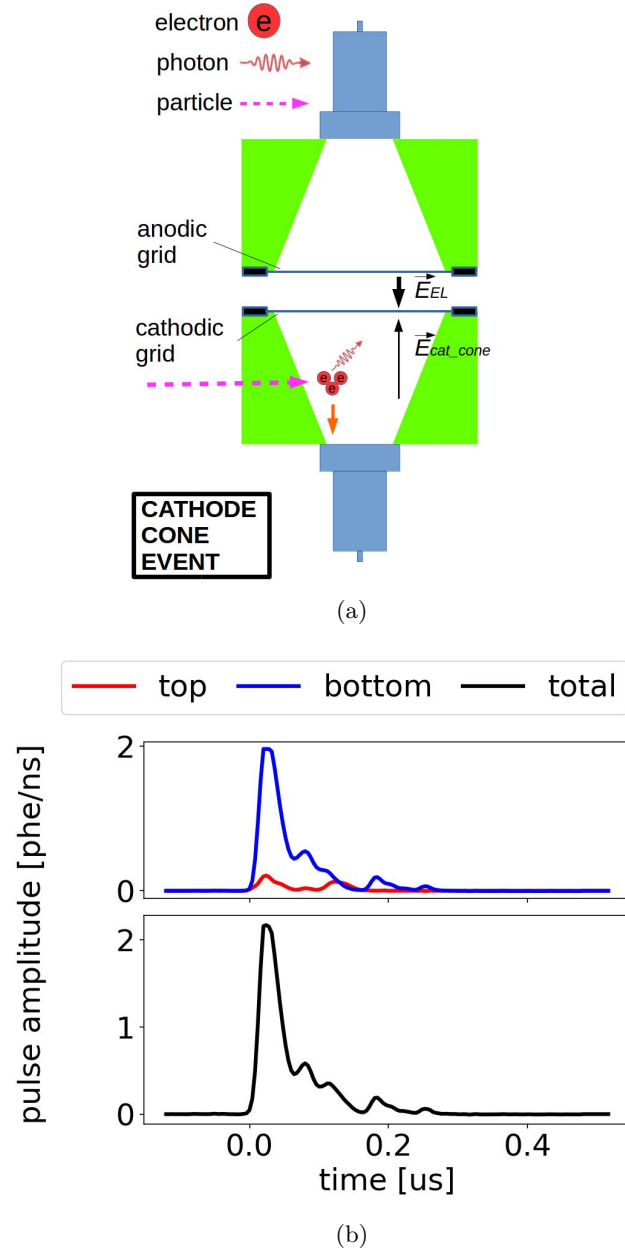


Figure 1.20: *Gas Test* signal: cathode cone event. (a) Cartoon of the process. Primary scintillation light ionization electrons are produced from the particle interaction, and the ionization electrons drift toward the bottom PMT. EL light is typically not produced along the trajectories of the electrons because the electric field in such region is lower than the EL threshold. (b) An example waveform of a cathode cone event. Data were taken at 2017-12-8 14:02, with grid voltages V_T and V_B at +6 kV and -6 kV, operating gas density at 0.137 mol L^{-1} .

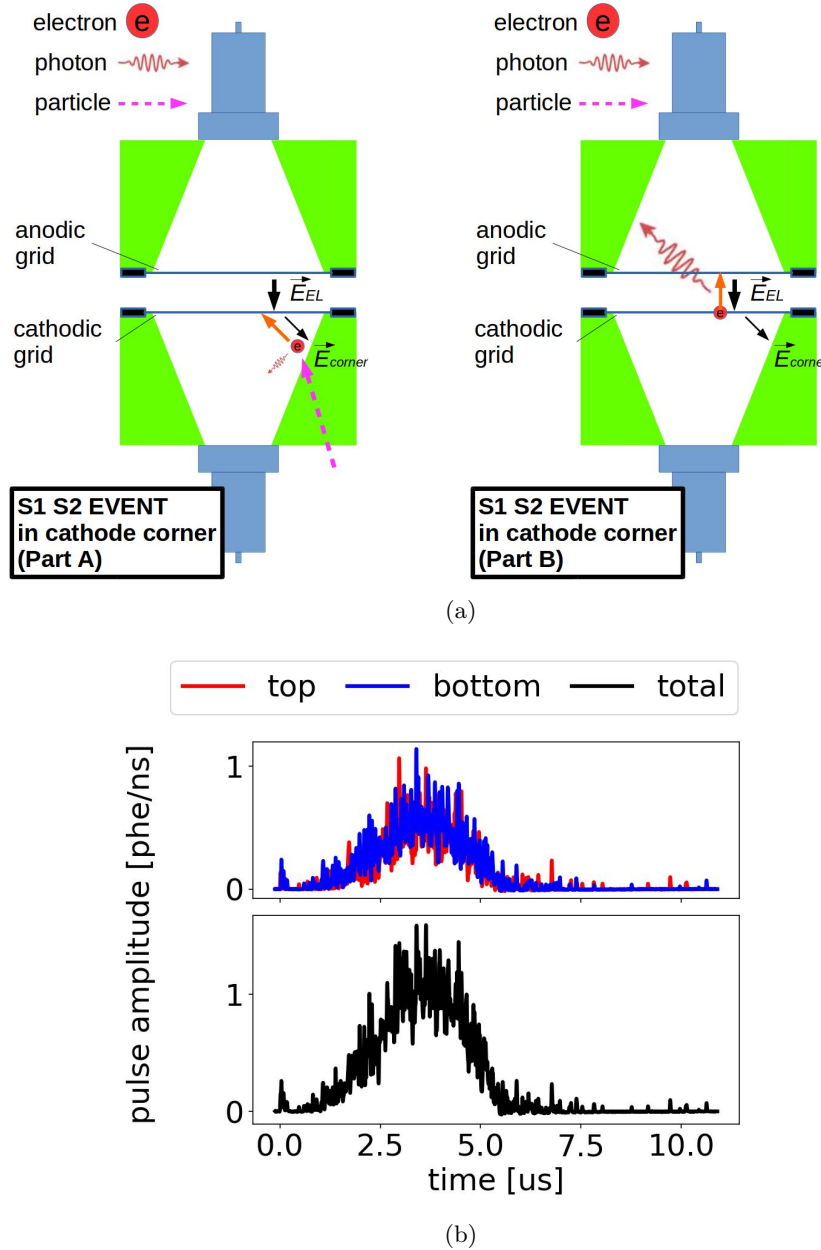


Figure 1.21: *Gas Test* signal: S1 S2 event in the cathode corner. (a) Cartoon of the process. Left: Primary scintillation light and ionization electrons are produced from the particle interaction, and the ionization electrons drift to the cathodic grid (part A). Right: EL light is produced in the EL region during electrons drifting to the anodic grid (part B). (b) An example waveform of an S1 S2 event in the cathode corner. Data were taken at 2017-12-8 14:02, with grid voltages V_T and V_B at +6 kV and -6 kV, operating gas density at 0.137 mol L^{-1} .

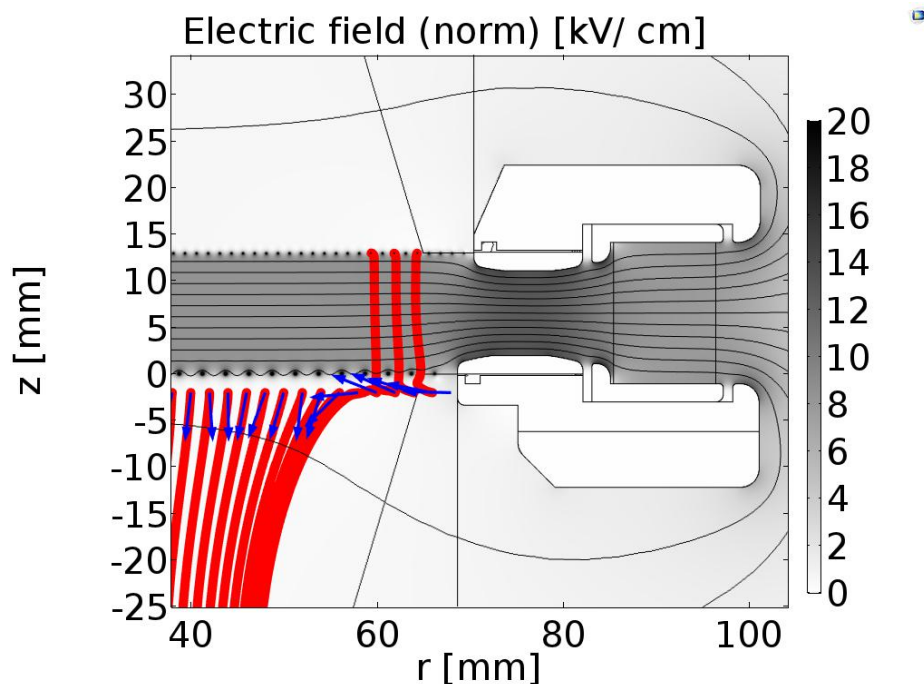


Figure 1.22: Electrostatic solution of the *Gas Test* detector (grid ring region). This result is solved with grid voltages V_T and V_B at +6 kV and -6 kV using COMSOL. The white metal structures in the middle of the figure are the cross sections of the grid rings. The contours show the electric potential; the color scales show the norm of electric field; the blue arrows shows the directions of the initial electron drift; the red lines shows the trajectory of electrons that start drifting at 2 mm below the bottom grid: electrons starting at $r < 60$ mm drift downward, when electrons starting at $r > 60$ mm drift into the EL region (cathode corner event).

S1 S2 event in the EL region S1 S2 events in the EL region (EL region events) are the particle radiation events which have energy deposition location either in EL region. The process and an example waveforms is shown in Fig. 1.23. Since the electrons are produced in the energy deposition location in the EL region, these electrons drift in the EL region toward the anodic grid, producing EL photons. The duration of these signals are shorter compared to the electron emission signals because of the shorter drift length. The total quantity of photon production in this type of events is usually higher than that of an electron emission event, an anode cone event, and a cathode cone event, because of the free drifted electrons inside the EL region.

High photon count events High photon count events are those particle radiation events that are extremely high on energy, therefore producing plenty primary scintillation photon, free drifted electrons, and EL photons during the events. The photon production rate is so high that it exceeds the digitizing ability of the DAQ system (also called saturate the DAQ), causing distortion on waveform recording thus resulting in difficulty of signal classification. These signals may have various origins. Some of these signals have comparable or shorter duration than electron emission signals, two example waveforms are shown in Fig. 1.24 and Fig. 1.25. These events might be related to the EL region events, described in Section 1.8.2, or grid wire radiation and ring radiation, which are the particle radiation events originated from radioactive elements in grid wire and ring materials.

The radioactive elements in the ring material can be both from the impurities in the material, e.g. ^{238}U , ^{232}Th , and ^{235}U and from the absorption of air on the material surfaces, e.g. ^{222}Rn . Among these sources, air radon absorption draw the most concern because of its abundance. The decay activity of radon induced radiation plating per unit of surface area per unit of time ($RA_{\text{Rn-rad}}$) is estimated as,

$$RA_{\text{Rn-rad}} = RV_{\text{Rn}} h_{\text{eff}} T_{\text{exposure}} \frac{1}{\tau_{\text{eff}}} \quad (1.20)$$

where RV_{Rn} is the radon decay activity in the air per unit of volume per unit of time; h_{eff} is the effective height of radiation plating, in which the radon decay daughter nuclei will plate on material surface; T_{exposure} is the exposure time of plating; and τ_{eff} is the effect decay time constant of radon decay daughter nuclei. With regard to RV_{Rn} 48 Bq m^{-3} , from Ref. [21], $h_{\text{eff}} \sim 1 \text{ m}$, $\tau_{\text{eff}} \sim 32 \text{ yr}$, from the decay time constant of ^{210}Pb , the typical daughter nucleus from the radon decay, in Ref. [Dulieu2008], and T_{exposure} 1 d, $RA_{\text{Rn-rad}}$ is $\sim 4 \times 10^{-3} \text{ Bq m}^{-2}$. For a $\sim 40 \text{ cm}^2$ grid wire and grid ring total surface area, The total decay activity of radon induced radiation from the ring surface is $\sim 10^{-5} \text{ Bq}$. These event rates should be relatively rare compared to other processes.

Multiple scattering events Multiple scattering events are those with more than one energy deposition location. The common source of these events are a high energy gamma radiation, since it can travel far distance in the detector. The multiple scattering events usually are combinations

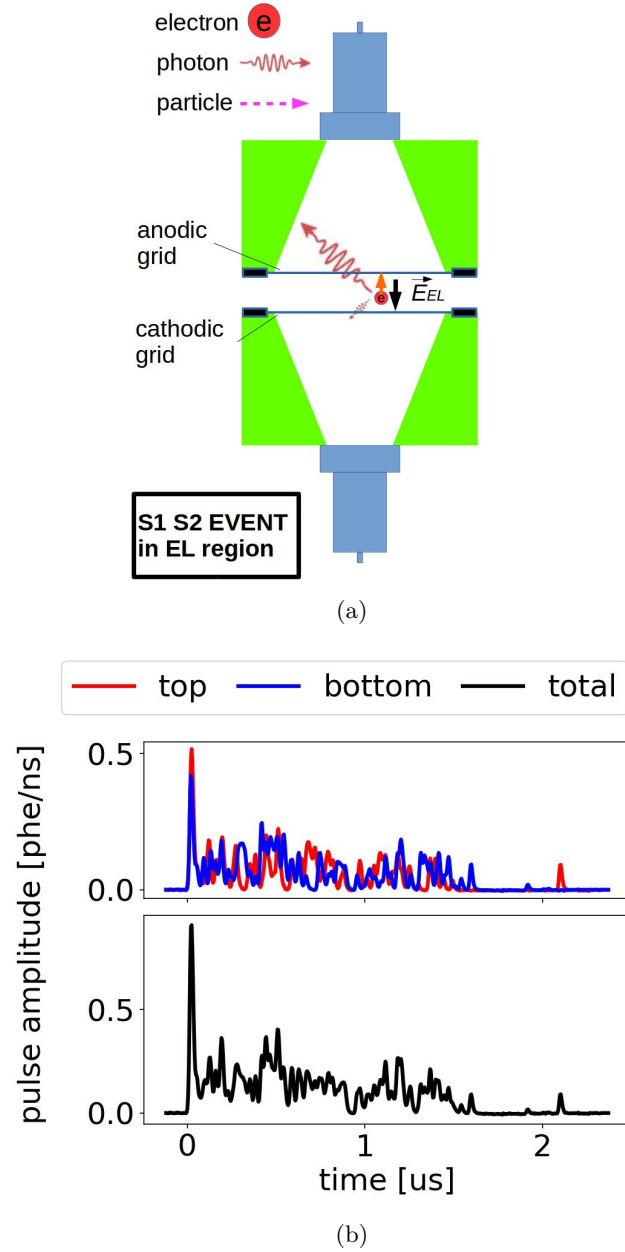


Figure 1.23: *Gas Test* signal: S1 S2 event in the EL region. (a) Cartoon of the process. Primary scintillation light and ionization electrons are produced from the particle interaction. The primary scintillation light and the EL light start to be produced simultaneously. (b) An example waveform of an S1 S2 event in the EL region. The primary scintillation light lies on top of the EL light. Data were taken at 2017-12-8 14:02, with grid voltages V_T and V_B at +6 kV and -6 kV, operating gas density at 0.137 mol L^{-1} .

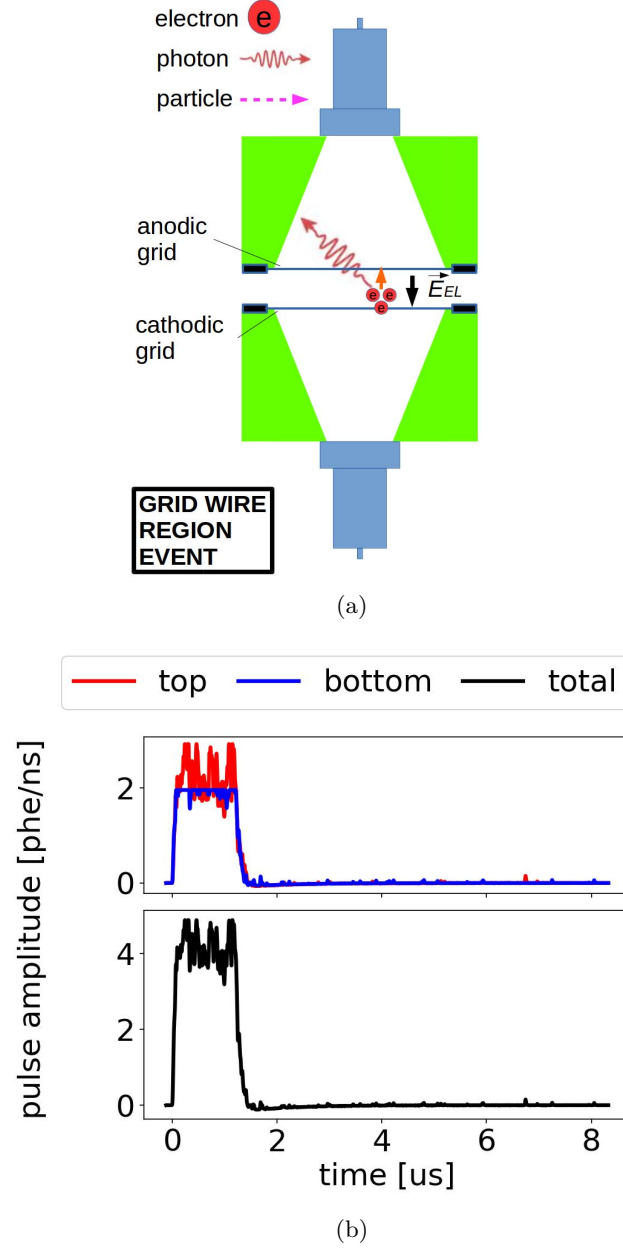


Figure 1.24: *Gas Test* signal: grid wire region event. (a) Cartoon of the process. (b) An example waveform. This might be an S1 S2 event in the EL region between the grid wires, when the primary scintillation light is clipped off because the signal amplitude exceeds DAQ dynamic range (PMT saturation). Data were taken at 2017-12-8 14:02, with grid voltages V_T and V_B at +6 kV and -6 kV, operating gas density at 0.137 mol L^{-1} .

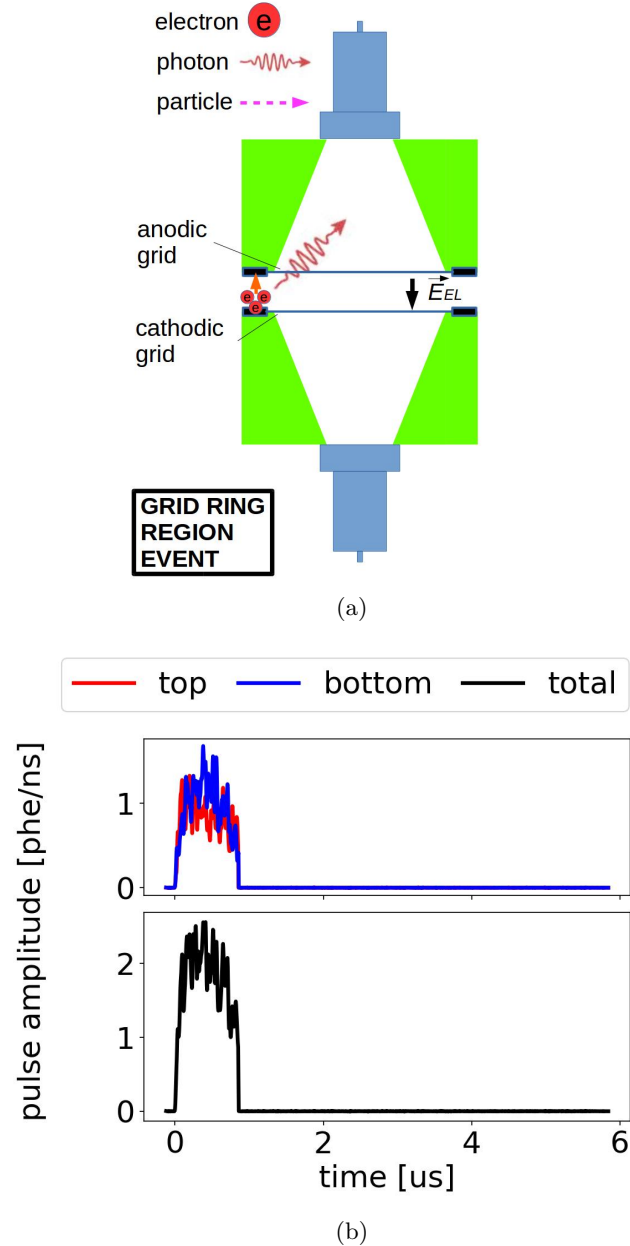


Figure 1.25: *Gas Test* signal: grid ring region event. (a) Cartoon of the process. (b) An example waveform. This might be an S1 S2 event in the EL region between the grid rings, when the primary scintillation light is not visible because the light collection efficiency is poor in this region. Data were taken at 2017-12-8 14:02, with grid voltages V_T and V_B at +6 kV and -6 kV, operating gas density at 0.137 mol L⁻¹.

of the previous mentioned type of events. Two example waveform are shown in Fig. 1.26: the first one is a multiple scattering event in the anode cone region; the second one is a multiple scattering event in the anode cone region and the EL region.

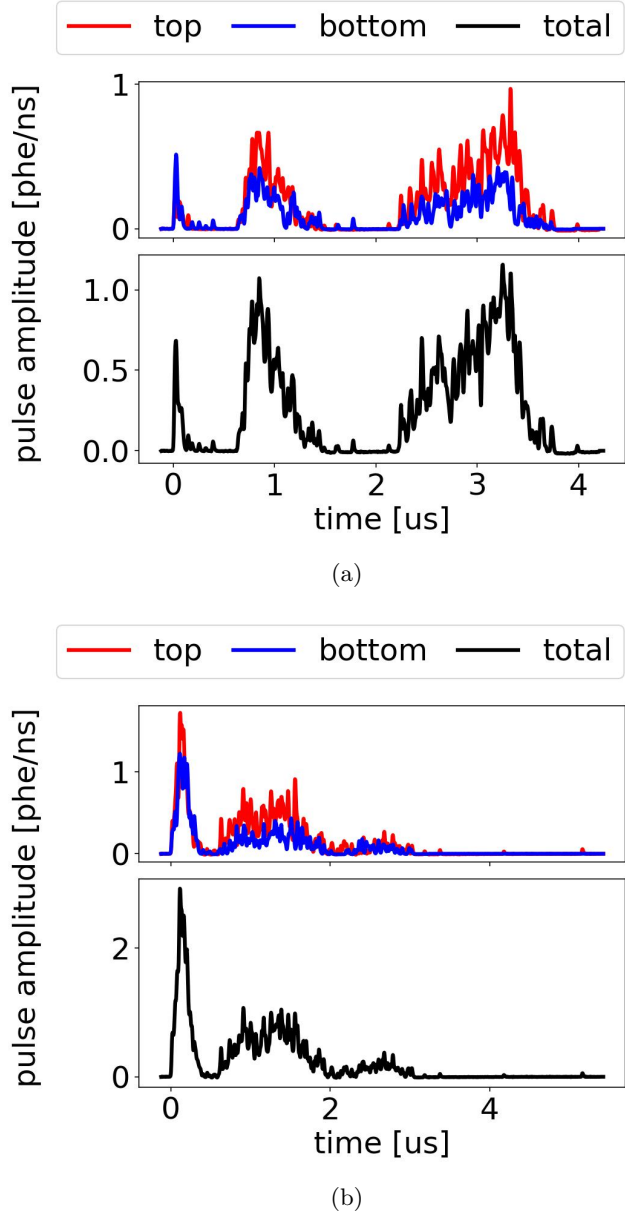


Figure 1.26: *Gas Test* signal: multiple scattering event. (a) An example waveform of a multiple scattering event in the anode cone region. (b) An example waveform of a multiple scattering event in the anode cone region and the EL region. Data were taken at 2017-12-8 14:02, with grid voltages V_T and V_B at +6 kV and -6 kV, operating gas density at 0.137 mol L^{-1} .

967 **1.8.3 Cosmic ray**

968 Cosmic rays, originating outside Earth, are capable of producing showers of secondary particles that
 969 reach the *Gas Test* detector and giving rise to signals in the detector. Among all secondary particles
 970 that raise signals, muons are the most common one because of their abundance and high penetration
 971 length in earth atmosphere. Unlike alpha, beta, and gamma particle radiation, a cosmic ray muon
 972 has a longer ionization trajectory which travels crossing the whole detector.

973 The long ionization trajectory leads to a large quantity of primary scintillation light and free
 974 electron production, which results in a large light production. The minimum stop power of muon is
 975 $1.255 \text{ MeV g}^{-1} \text{ cm}^2$ in xenon, from Ref. [22]. In xenon gas, the reported average energy to produce
 976 a primary scintillation photon (W_{sci}) and electron-ion pair (W_{ion}) are $\sim 100 \text{ eV}$ ² and 22 eV ³,
 977 respectively. Therefore, with detector operating gas density at 0.137 mol L^{-1} , a muon event produce
 978 $\sim 2 \times 10^2$ primary scintillation photons and $\sim 10^3$ per centimeter length of muon trajectory. The
 979 large quantity of primary scintillation light and EL light production associated with free electrons
 980 results in large signal area detected for a muon event.

981 Therefore, a cosmic ray muon signal has a different appearance compared to other signals because
 982 of its long ionization trajectory and large quantity of primary scintillation light and electron-ion pair
 983 production. The appearance of muon signals also varies according to their different trajectories in
 984 the detector, which will be discussed below.

985 **EL region muon event** EL region muon events are those events that crosses the EL region, as
 986 well as the anode cone region and the cathode cone region. A cartoon and an example waveform
 987 are shown in Fig. 1.27. Like particle radiation events, at the very beginning of the signal, primary
 988 scintillation photons are produced in the first 500 ns. Simultaneously, during the first $2.5 \mu\text{s}$, the
 989 shown signal is dominated by EL photons, which decrease in time because the electrons in the EL
 990 region land on the anodic grid thus stopping EL photon production, illustrated in Fig. 1.27a (left).
 991 Since free electrons are generated all the way including the EL region, there is prompt EL light that
 992 masks the primary scintillation, causing difficulty to distinguish light from these two processes. At a
 993 higher absolute value of $\Delta V_{\text{T-B}}$, there is higher photon production per drifted electron, which results
 994 in an increase in the signal amplitude and signal area. This high signal amplitude can exceed the
 995 dynamic digitization range of the DAQ and results in a clip on the waveform, like in Fig. 1.27b. After
 996 all electrons in the EL region reach the anodic grid, the signal is dominated by electrons originally
 997 produced in the anode cone drift to the anodic grid and EL photons are produced in the high electric
 998 field around the anodic grid, illustrated in Fig. 1.27a (right), which is “long tail” part of the signal
 999 in the range of $2.5 \mu\text{s}$ to $10 \mu\text{s}$ in Fig. 1.27b.

1000 EL region muon events between grid rings are those events that crosses the EL region between

² W_{sci} is $111(16) \text{ eV}$ in Ref. [23], and $72(6) \text{ eV}$ in Ref. [24].

³ W_{ion} is 22 eV in Ref. [25–27].

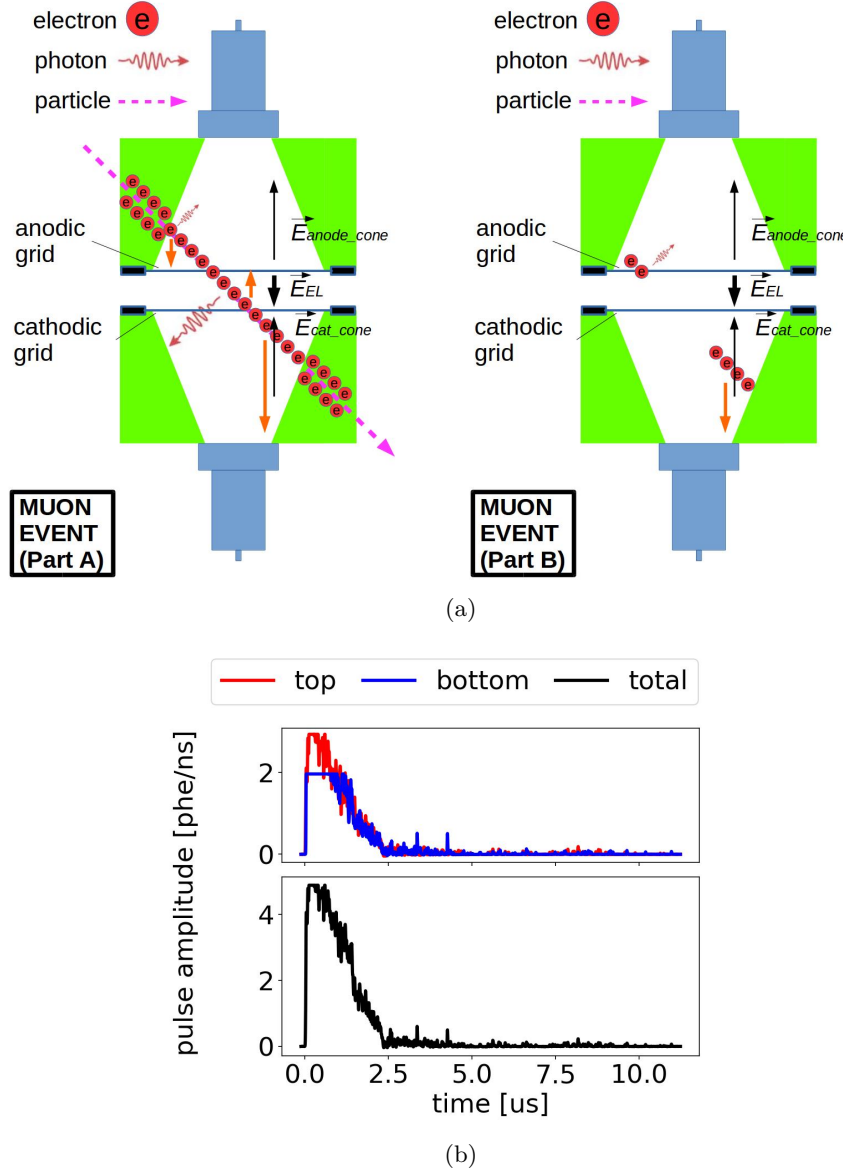


Figure 1.27: *Gas Test* signal: EL region muon event. (a) Cartoon of the process. Left: Primary scintillation light and ionization electrons are produced along the muon trajectory, and ionization electrons drift according to the direction of the electric field. EL light also start to be produced by the ionization electrons in the EL region (part A). Right: EL light is produced in the high electric field region around the anodic grid wires (part B). (b) An example waveform of an EL region muon event. The right-angled triangle shape waveform before $2.5 \mu\text{s}$ is the EL light produced in the EL region (cartoon part A). The primary scintillation light is clipped off because of the PMT saturation. The “long tail” after $2.5 \mu\text{s}$ is the EL light produced around the anodic grid wires (cartoon part B). Data were taken at 2017-12-8 14:02, with grid voltages V_T and V_B at $+6 \text{ kV}$ and -6 kV , operating gas density at 0.137 mol L^{-1} .

1001 the grid rings, without crossing the anode cone region. The cartoon of this process is shown in
 1002 Fig. 1.28a. Similar to other EL region muon events, these events produce primary scintillation light
 1003 and EL light between the grid rings. However, since the muon trajectory does not cross the anode
 1004 cone region, there are no free electrons produced in such region, which leads to the absence of the
 1005 “long tail” in the signal, as shown in Fig. 1.28b.

1006 **Anode cone muon event** Anode cone muon events are those events that cross only the anode
 1007 cone region. A cartoon and an example waveform are shown in Fig. 1.29. At the very beginning of
 1008 the signal, primary scintillation photons are produced in the first 500 ns, the process and waveform
 1009 of which are shown in Fig. ?? and Fig. 1.29c. Next, electrons originally produced in the anode cone
 1010 drift to the anodic grid and EL photons are produced in the high electric field around the anodic
 1011 grid, the process and waveform of which are shown in Fig. 1.29a and Fig. 1.29d.

1012 **Cathode cone muon event** Cathode cone muon events are those events that cross only the
 1013 cathode cone region. A cartoon and an example waveform are shown in Fig. 1.30. At the very
 1014 beginning of the signal, primary scintillation photons are produced in the first 500 ns, the process and
 1015 waveform of which are shown in Fig. 1.30a and Fig. 1.30b. Next, electrons originally produced in
 1016 the cathode cone drift to the cathode PMT associated with few EL photons production in this low
 1017 electric field cathode cone region.

1018 1.8.4 Other miscellaneous sources

1019 **Electrical noise** Electrical noise are the disturbance in an electrical system during signal transfer.
 1020 Electrical noise can come from both internal and external sources to the system, and can add to
 1021 the systematic fluctuation of other signals from the *Gas Testdetector*. This systematic fluctuation
 1022 is characterized by the baseline fluctuation, whose amplitude is ~ 0.36 mV, which is very small
 1023 compared to signal amplitude of the wanted signals.

1024 Electrical noise from the external electrical grounding of the infrastructures and the KNF pump,
 1025 however, has an amplitude up to 5 mV and is capable of start a separate pulse recording sometimes;
 1026 this type of electrical noise is called electrical noise signals. An example waveform of electrical noise
 1027 signal is shown in Fig. 1.31. As shown in this figure, an electrical noise signal is likely to have the
 1028 waveforms in both PMTs overlapping. The waveform in each PMT is bipolar and symmetric; that
 1029 is, the positive and negative maxima of the waveform amplitude are about the same. The bipolar
 1030 and symmetric aspect of the waveform leads to a near-zero integral of the signal area, which don't
 1031 give a meaningful waveform shape RQs because these RQ algorithms are designed for a unipolar
 1032 signal. Therefore, to reduce the influence of these electrical noise signals, the KNF pump is turn off
 1033 during all measurements and we improved on the electrical grounding of infrastructure. After this
 1034 improvement, electrical noise signals occur at a rate of ~ 2 Hz, which are further addressed by signal

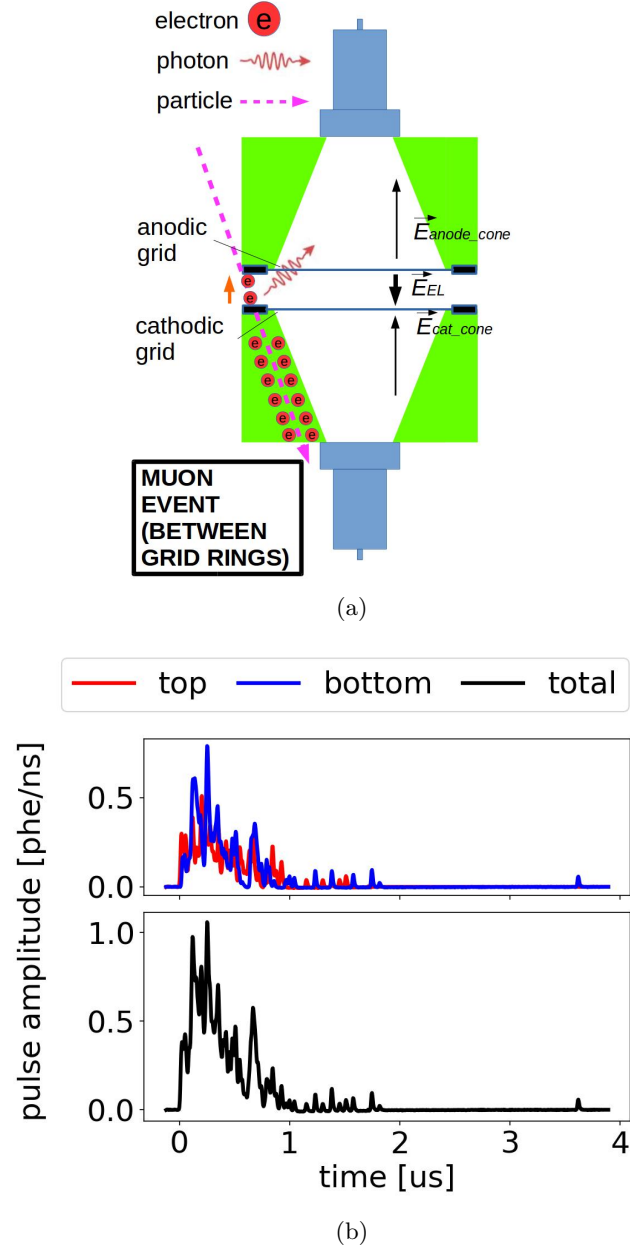


Figure 1.28: *Gas Test* signal: muon event between the grid rings. (a) Cartoon of the process. This process is similar to that of the EL region muon event except there are no electrons produced in the anode cone region. (b) An example waveform. The absence of “long tail” is because of the absence of electrons produced in the anode cone region. Data were taken at 2017-12-8 14:02, with grid voltages V_T and V_B at +6 kV and -6 kV, operating gas density at 0.137 mol L^{-1} .

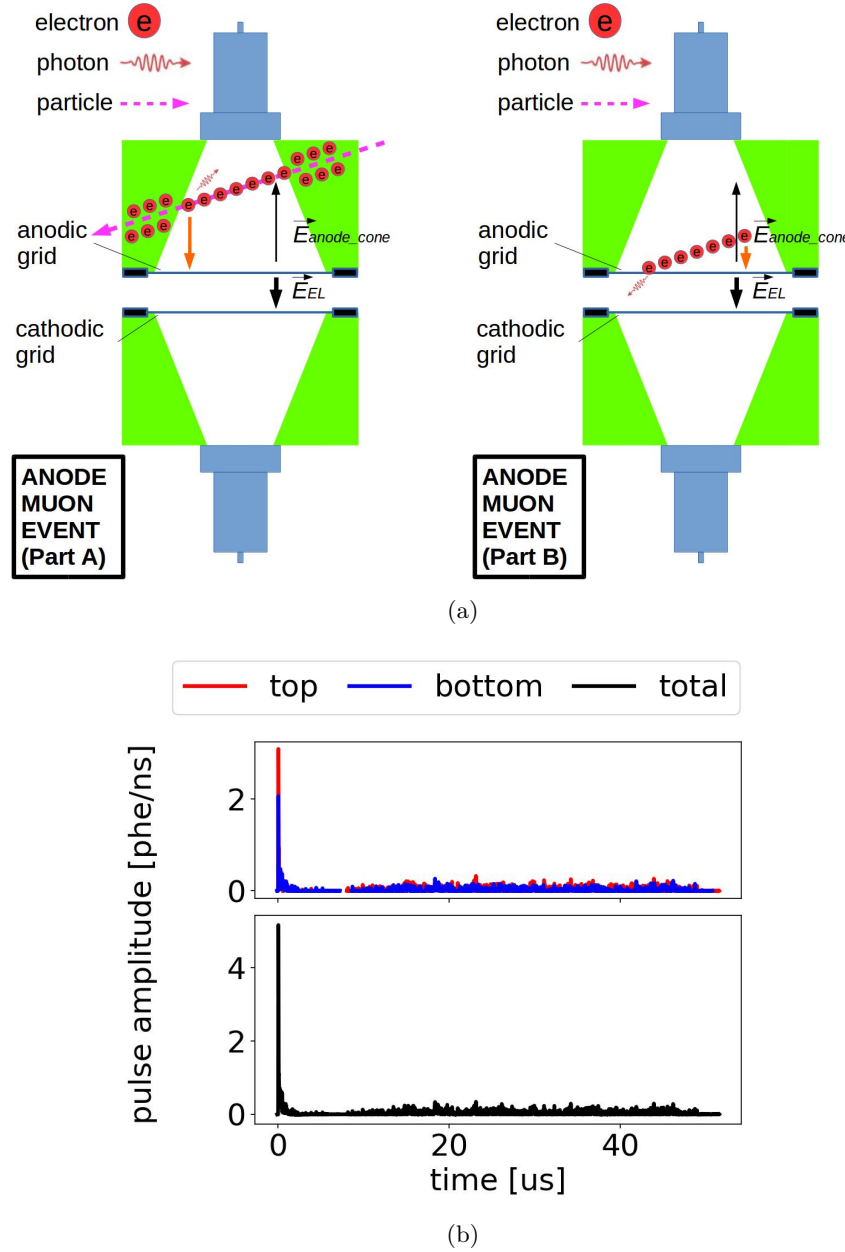


Figure 1.29: *Gas Test* signal: anode cone muon event. (a) Cartoon of the process. This process is similar to that of the EL region muon event except for there are no electrons produced in the EL region. (b) An example waveform of an anode muon cone event. The absence of the “right-angled triangle shape waveform” is because of the absence of electrons produced in the EL region. Data were taken at 2017-12-8 14:02, with grid voltages V_T and V_B at +6 kV and -6 kV, operating gas density at 0.137 mol L^{-1} .

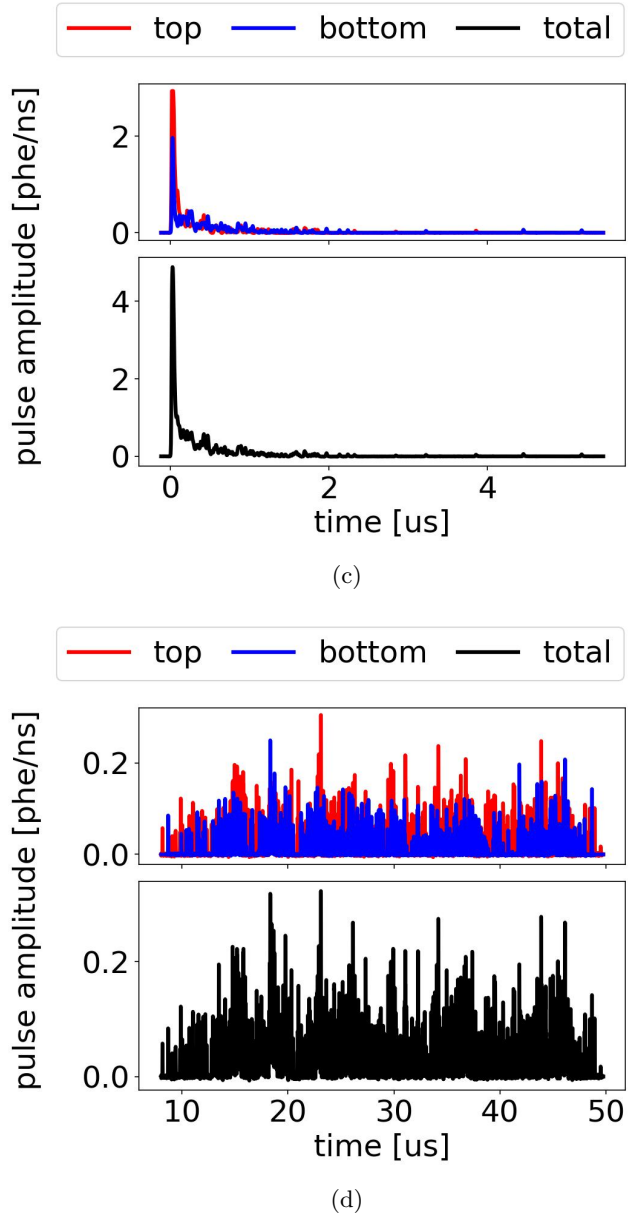


Figure 1.29: *Gas Test* signal: anode muon cone event (cont.). (c) An example waveform of an anode muon cone event, zoomed in the range of $0 \mu\text{s}$ to $5 \mu\text{s}$, which shows the primary scintillation light (cartoon part A). (d) An example waveform of an anode cone muon event, zoomed in the range of $6 \mu\text{s}$ to $50 \mu\text{s}$, which shows the EL light produced around the anodic grid wires (cartoon part B).

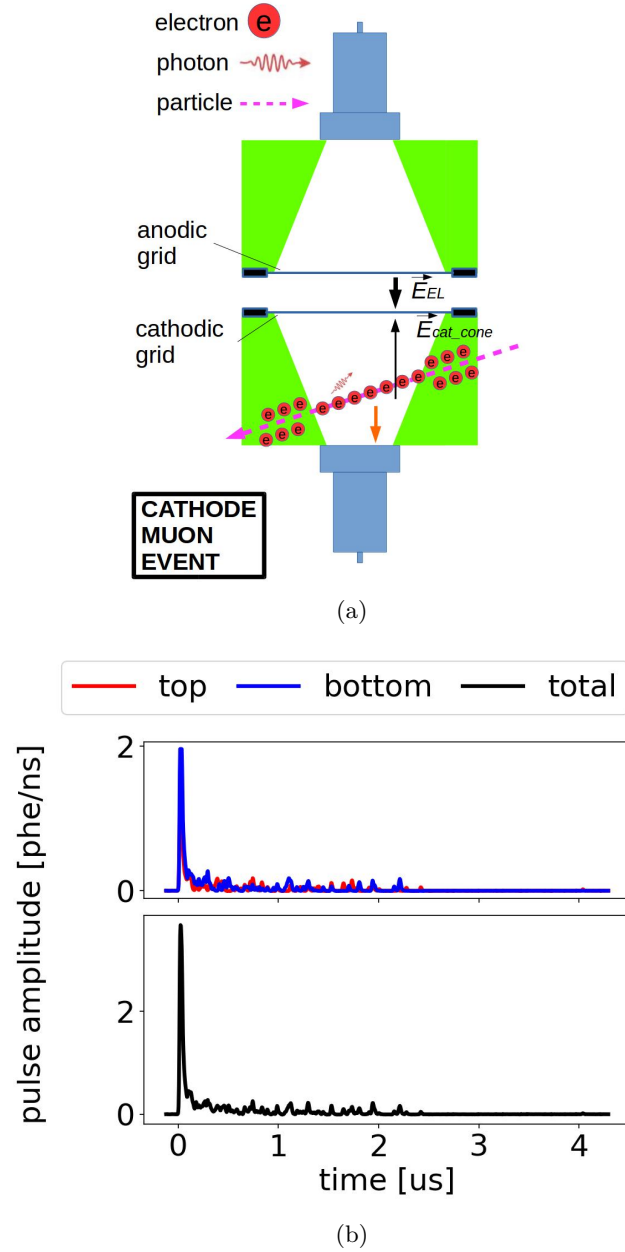


Figure 1.30: *Gas Test* signal: cathode cone muon event. (a) Cartoon of the process. This process is similar to that of the EL region muon event except for there are no electrons produced in the EL region or the anode cone region. (b) An example waveform of a cathode muon cone event. The absence of the “right-angled triangle shape waveform” and the “long tail” is because of the absence of electrons produced in the EL region and the anode cone region. Data were taken at 2017-12-8 14:02, with grid voltages V_T and V_B at +6 kV and -6 kV, operating gas density at 0.137 mol L^{-1} .

1035 selections based on the bipolar feature of the noise signals.

1036 **PMT dark current** PMT dark current usually refers to the signal from the thermal electron
 1037 emission from the photocathode and dynode surfaces, which are charges generated in the PMT
 1038 when no photon ejects photoelectrons from the photocathode surface. The thermal electrons from
 1039 the photocathode surface, like photoelectrons, if landing on the effective area of the first dynode, will
 1040 be amplified by the PMT and produce a SPHE-like signal. Such SPHE-like signals of the PMT dark
 1041 current are a major concern, since they are not distinguishable from SPHEs in signals of interest.
 1042 The thermal electrons from other surfaces may also be amplified by the PMT dynode chain and
 1043 produce signals that are distinguishably smaller than SPHE, thus drawing less concern.

1044 A random coinciding of SPHE-like signals (dark current is one of the most common sources of
 1045 SPHE-like signals) between two PMTs, is called an accidental coinciding signal. The PMTs that
 1046 are used in this study have a ~ 1 kHz dark current rate. This rate leads to a ~ 3.4 Hz rate of the
 1047 accidental coinciding signals with regard to CCW of $1.7\ \mu s$.

1048 **should I talk about PMT afterpulsing?**

1049 **PTFE fluorescence** PTFE fluorescence is the phenomenon in which PTFE emits photons that
 1050 it absorbed. This delay emission normally appears in forms of SPHEs following a high quantity
 1051 of photon production, and increase the SPHE rate succeeding. The rate of after emission photons
 1052 (fluorescence rate) roughly follows an exponential decay model:

$$\text{fluorescence rate} = f_{\text{FR}} A \frac{1}{\tau} \exp\left(-\frac{t}{\tau}\right) \quad (1.21)$$

1053 where τ is the decay time constant; t is the time since the previous photon production; A is quantity of
 1054 photons in the previous photon production that are absorb by the PTFE; and f_{FR} is the fluorescence
 1055 ratio, which is the ratio of the number of photons emitted after by the PTFE material to the number
 1056 of photons absorbed by the PTFE material.

1057 Measurements show that fluorescence rates, decay times τ , and fluorescence ratio f_{FR} have a vari-
 1058 ous range. This might be caused by different conditions of synthesis, as described in Ref. [Gachkovskii1969].
 1059 This effect is also believed to cause the slow decay of electron signal in liquid xenon TPCs. A decay
 1060 time of 2.3 ms is reported in Ref.[28]. A decay time of 10 ms is reported in internal review in LUX.

1061 To illustrate the large rate of SPHEs that follows a large-area signal, we look at 1-ms windows
 1062 before and after a large photon production. In the succeeding 1-ms window after $t = 0$, which is the
 1063 time when the selected large signal happened, as shown with the selected large signal in Fig. 1.33a,
 1064 Fig. 1.33b, we see 33 SPHEs. In comparison, we see only 1 SPHE in the earlier 1-ms window, as
 1065 shown in the same figure before $t = 0$. This increasing rate of SPHE increases the probability of
 1066 accidental coinciding between two PMT channels, as shown in Fig. 1.33c; given the practical choice
 1067 of our CCW, this random accidental coinciding, like PMT dark current, is a potential source of

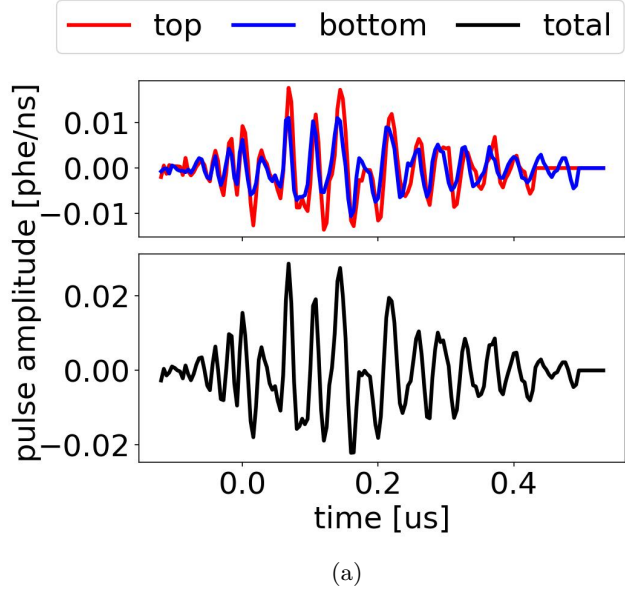


Figure 1.31: *Gas Test* signal: electronic noise signal. (a) An example waveform. Data were taken at 2017-12-8 14:02, with grid voltages V_T and V_B at +6 kV and -6 kV, operating gas density at 0.137 mol L^{-1} .

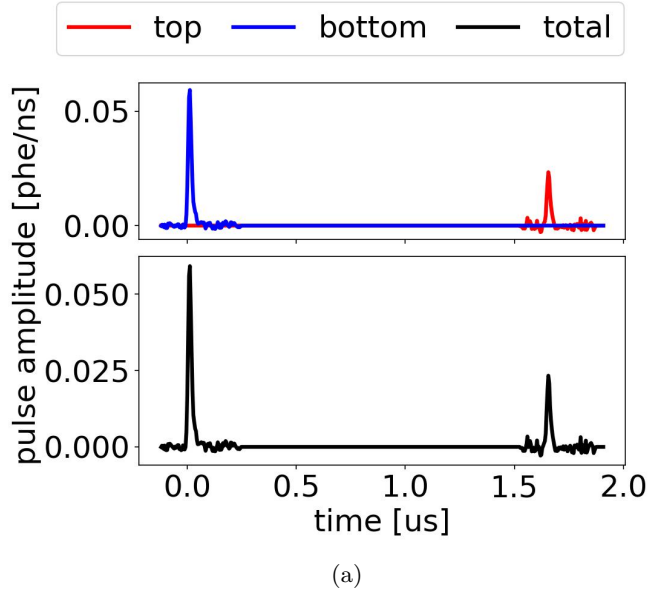


Figure 1.32: *Gas Test* signal: PMT dark current accidental coinciding. (a) An example waveform. Data were taken at 2017-12-8 14:02, with grid voltages V_T and V_B at +6 kV and -6 kV, operating gas density at 0.137 mol L^{-1} .

1068 background that looks like electron emission signals.

1069 With these examples in mind, we can quantify the fluorescence process by looking at the delayed
 1070 SPHE rate follow large-area signals over different characteristic timescales. The SPHE rate of this
 1071 PTFE fluorescence increase if the ELD has a recent large photon production. Fig. 1.34 shows the
 1072 photon rate after source signals: This photon fluorescence rate increases as the signal area of source
 1073 signals increases; and this photon fluorescence rate decreases over time.

1074 An estimation of fluorescence rate, decay time τ , and fluorescence ratio f_{FR} is carried out by
 1075 studying the photon rate in the waveform after a signal production of larger than 10^4 phe in the range
 1076 of $200\ \mu\text{s}$ to $600\ \mu\text{s}$ after the end time of signal. The choice of the smaller value of the succeeding
 1077 window is to avoid the influence from the anode cone events correlating signals, whereas the choice
 1078 of the later time of the succeeding window is to avoid the influence the background rate, which is
 1079 mostly contributed by dark current. In the chosen signal ranges, the background rate is $\sim 1\ \text{kHz}$ per
 1080 PMT, mostly contributed by PMT dark current. This rate is small compared to fluorescence rate
 1081 (median $\sim 20\ \text{kHz}$) per PMT, thus negligible in this estimation. Therefore,

$$\text{photon rate} \approx \text{fluorescence rate} (+ \text{background rate (dark current, etc.)}) \quad (1.22)$$

$$\propto \frac{1}{\tau} \exp\left(-\frac{t}{\tau}\right) \quad (1.23)$$

1082 To better estimate the photon rate profile and find the decay time τ , we fit this exponential decay
 1083 profile to binned data in the succeeding window. To combine multiple events to reduce the statistical
 1084 error, individual events are normalized by their signal areas in the range of $0\ \mu\text{s}$ to $1000\ \mu\text{s}$ and then
 1085 co-added by bin; the resulting graph is fitted, and shown in Fig. 1.35: τ of $(407 \pm 35)\ \mu\text{s}$.

1086 The fluorescence ratio f_{FR} is defined as,

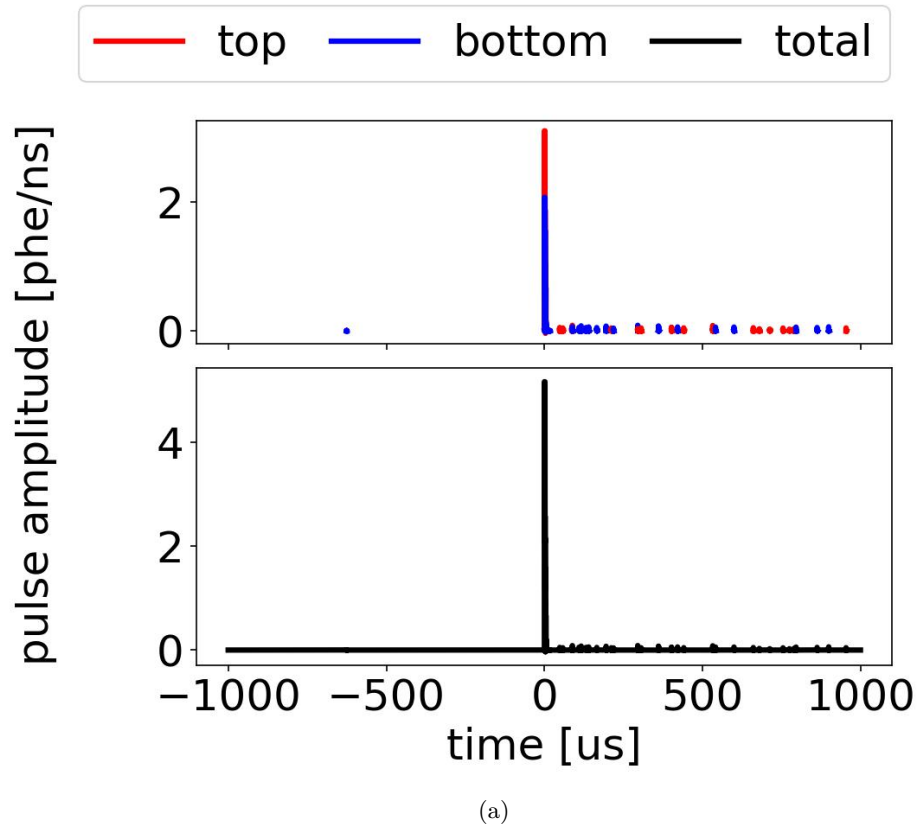
$$f_{\text{FR}} = \frac{\# \text{ photons reemitted}}{\# \text{ photons absorbed}} \quad (1.24)$$

1087 which is the ratio of the number of photons that are reemitted from the PTFE after a large-area
 1088 event to the number of photons that are absorbed by the PTFE in a large-area event.

1089 The number of photons reemitted is estimated from the exponential decay profile defined above
 1090 and the number of photons in the succeeding $200\ \text{ns}$ to $600\ \text{ns}$ window after the end of the large-
 1091 area signal. From the estimated decay time, the ratio of the number of reemitted photons in the
 1092 succeeding window (N_{SW}) to the total number of reemitted photons is derived, noted as P_{SW} :

$$P_{\text{SW}} \approx \frac{N_{\text{SW}}}{\# \text{ photons reemitted}}. \quad (1.25)$$

1093 The number of reemitted photons in the succeeding window is estimated from the number of
 1094 photons reemitted detected in the succeeding window (A_{SW}) and the light collection efficiency for



(a)

Figure 1.33: *Gas Test* signal: PTFE fluorescence after an event with large photon production. (a) An example waveform 1000 μs before and after a large-area signal. There are more SPHEs after an event with large photon production than before. The SPHE rate before this large-area event is representative of the average SPHE rate. Data were taken at 2017-12-8 14:02, with grid voltages V_T and V_B at +6 kV and -6 kV, operating gas density at 0.137 mol L $^{-1}$.

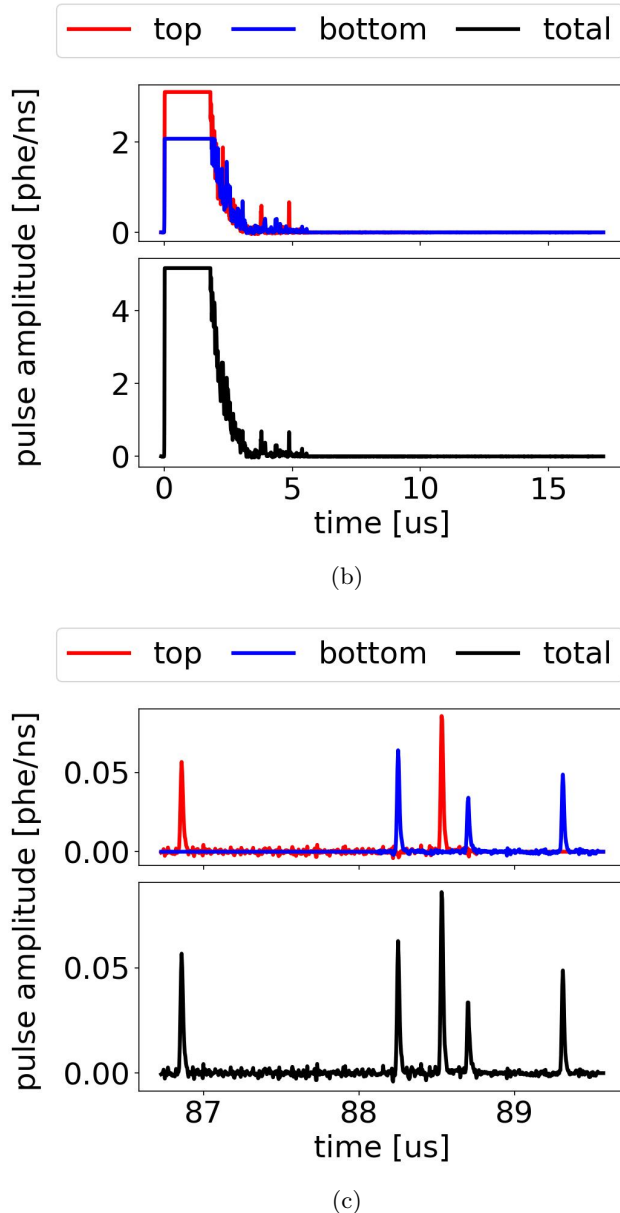


Figure 1.33: *Gas Test* signal: PTFE fluorescence after an event with large photon production (cont.). (b) An example waveform, zoomed in the range of $0\ \mu\text{s}$ to $17\ \mu\text{s}$, which shows the signal with large photon production. (c) An example waveform, zoomed in the range of $87\ \mu\text{s}$ to $89\ \mu\text{s}$, which shows PTFE fluorescence induced SPHEs accidental coinciding between the two PMTs. This accidental coinciding signal looks like an electron emission signal.

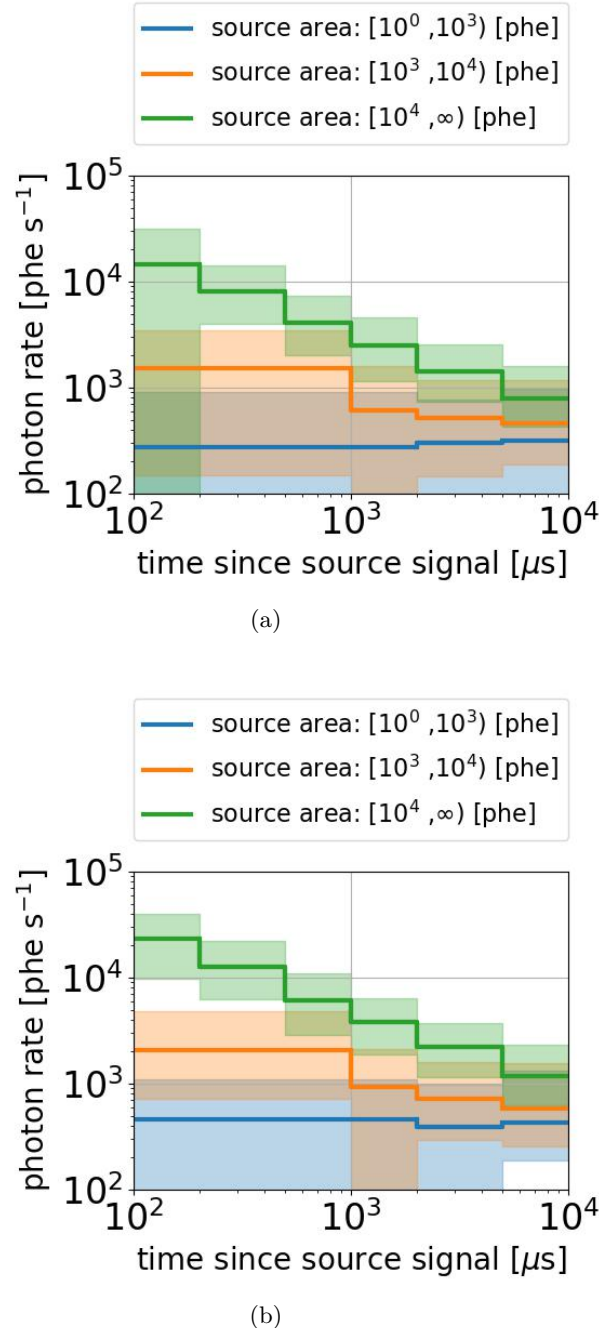


Figure 1.34: Photon fluorescence rate after photon production in the ELD: (a) top PMT; (b) bottom PMT. The solid lines show the medians. The color bands show the 25 % to 75 % bands. The choice of bin edges is made to get enough statistics in each bin.

¹⁰⁹⁵ photons starting from PTFE surface:

$$A_{\text{SW}} \approx \text{LCE}_{\text{PTFE}} N_{\text{SW}}. \quad (1.26)$$

¹⁰⁹⁶ where LCE_{PTFE} is the average light collection efficiency for photons starting from PTFE surface.

¹⁰⁹⁷ On the other hand, the number of photons absorbed by PTFE is estimated from the total number
¹⁰⁹⁸ of photons the source large-area signal (N_{source}) and the light collection simulation of the fraction
¹⁰⁹⁹ of photons that PTFE absorbed:

$$\# \text{ photons absorbed} \approx \text{LCF}_{\text{EL-PTFE}} N_{\text{source}} \quad (1.27)$$

¹¹⁰⁰ where $\text{LCF}_{\text{EL-PTFE}}$ is the average fraction of photons absorbed by PTFE in the simulation with
¹¹⁰¹ photons starting in the EL region, the location where the source signals happen.

¹¹⁰² The total number of photons the source large-area signal (N_{source}) is related to the detected
¹¹⁰³ signal area (A_{source}) and light collection efficiency of the source signals in the EL region (LCE_{EL}).

$$A_{\text{source}} \approx \text{LCE}_{\text{EL}} N_{\text{source}} \quad (1.28)$$

¹¹⁰⁴ Therefore, from the measure ratio of signal area in the succeeding window (A_{SW}) to the source
¹¹⁰⁵ signal area (A_{source}), the result of which is shown in Fig. 1.36, we can derive the fluorescence ratio
¹¹⁰⁶ f_{FR} . P_{SW} is ~ 0.23 with regard to the decay time τ . LCE_{PTFE} is 2.85 % (top PMT: 1.35 %, bottom
¹¹⁰⁷ PMT: 1.50 %); LCE_{EL} is 1.70 % (top PMT: 0.85 %, bottom PMT: 0.85 %); and $\text{LCF}_{\text{EL-PTFE}}$ is 79.3 %
¹¹⁰⁸ (top cone: 39.0 %, bottom cone: 40.3 %), which are estimated by using the same method as described
¹¹⁰⁹ in Section 1.6 using PTFE reflectivity of 0.4. With the ratio of A_{SW} to A_{source} $\sim 0.5 \times 10^{-3}$, f_{FR}
¹¹¹⁰ is $\sim 1.6 \times 10^{-3}$. This result has a big uncertainty (up to 1×10^{-3}) due to statistic errors, and the
¹¹¹¹ systematic errors in the light collection efficiency and the absorption fraction, resulting from the
¹¹¹² uncertainty in the PTFE reflectivity value.

¹¹¹³ **Cherenkov radiation** think about gamma particle induced cherenkov, and whether the calcu-
¹¹¹⁴ lation is correct. Cherenkov radiation is the photon radiation process when a charged particle is
¹¹¹⁵ traveling through a medium with its speed higher than the speed of light in the medium. The
¹¹¹⁶ charged particle could be an external charged particle or electrons that originate from energy loss of
¹¹¹⁷ external particle in the medium. Because of the photon production in Cherenkov radiation process,
¹¹¹⁸ especially when this process happens in the PTFE materials (and the PMT windows), it is consid-
¹¹¹⁹ ered to one of the sources of the signals in *Gas Test*. A cartoon for the physical process and an
¹¹²⁰ example waveform of extremely narrow pulse are shown in Fig. 1.37.

¹¹²¹ The quantity of photon production in Cherenkov radiation process is estimated by its theoretical
¹¹²² spectrum following Frank–Tamm formula. A simplified approximation for Frank–Tamm formula

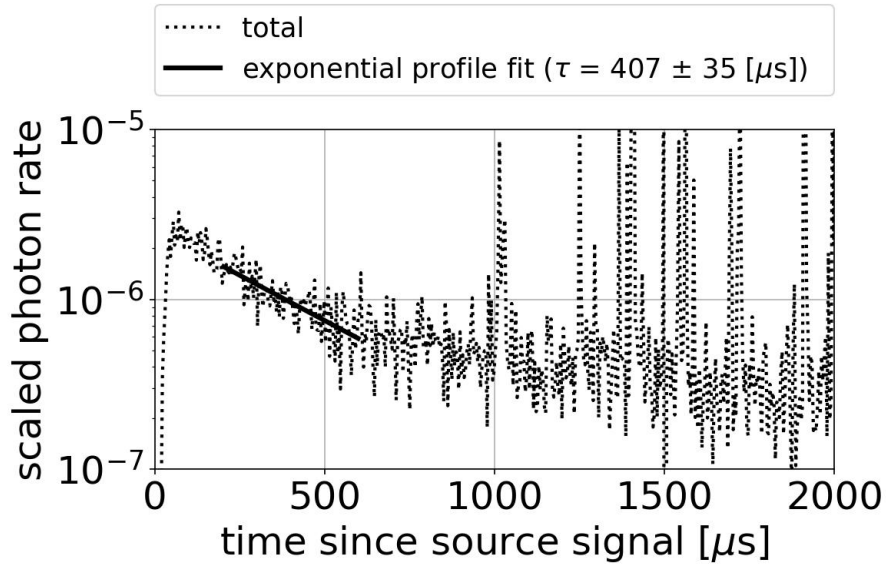


Figure 1.35: The average of scaled waveform in the range of $0 \mu\text{s}$ to $2000 \mu\text{s}$ since source signals. See text for details.

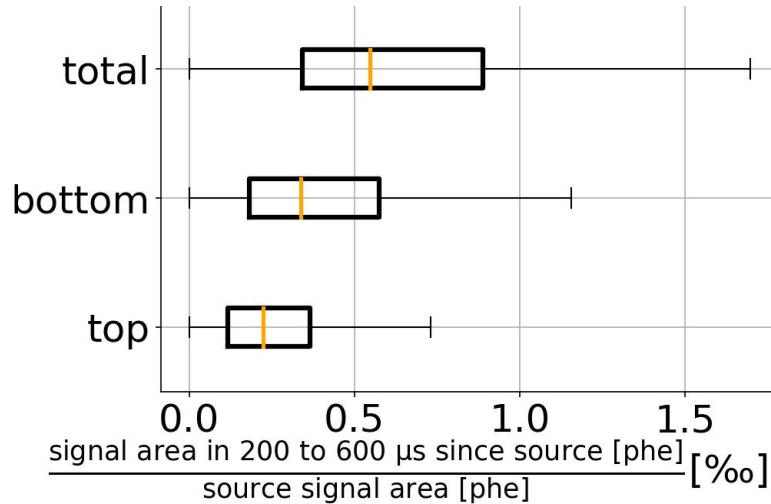


Figure 1.36: The ratio of the number of SPHEs in the range of $200 \mu\text{s}$ to $600 \mu\text{s}$ since source signals to the number of SPHEs in the source signal.

1123 from Ref. [Jackson1999] Eqn. 14.133 shows:

$$\frac{dI(\omega)}{dx} = \frac{e^2\omega}{c^2} \left[1 - \frac{1}{\beta^2\epsilon(\omega)} \right] \quad (1.29)$$

1124 where ω is the frequency of Cherenkov radiation, $I(\omega)$ is the energy intensity of frequency ω , $\epsilon(\omega)$ is
1125 the relative permittivity of the medium, and β is the speed of the charged particle. ω satisfies that
1126 $\beta^2\epsilon(\omega)$ is larger than one, so that the energy intensity is positive. The number intensity $N(\omega)$ can
1127 be derived from Eqn. 1.29

$$\frac{dN(\omega)}{dx} = \frac{\alpha}{c} \left[1 - \frac{1}{\beta^2\epsilon(\omega)} \right] \quad (1.30)$$

1128 where $\alpha \equiv e^2/\hbar c \approx 1/137$ is the fine structure constant. The total quantities of photons (N) is the
1129 integral over frequency and distance of Eqn. 1.30.

1130 A portion of these Cherenkov radiation photons can be seen by the PMTs, since PTFE is partially
1131 transparent to these photons. The duration of Cherenkov radiation event light production is the
1132 duration of charged particle energy loss process, which is typically very short (~ 1 ns to 10 ns). The
1133 number of photons (A_{Che}) detected by the PMTs for a typical 1 MeV electron is estimated using the
1134 following parameters:

$$A_{\text{Che}} \approx N_{\text{Che}} f_{\text{to-surface}} \exp(-d_{\text{to-surface}}/d_{\text{atten}}) \text{LCE}_{\text{PTFE}} \quad (1.31)$$

1135 where N_{Che} is the number of produced Cherenkov radiation photons which the PMTs are sensitive to;
1136 $f_{\text{to-surface}}$ is the fraction of Cherenkov radiation photons going toward the PTFE surface; $d_{\text{to-surface}}$
1137 is the distance from the location of Cherenkov radiation produce to the PTFE surface; d_{atten} is
1138 the attenuation length of PMT sensitive Cherenkov radiation photons; and LCE_{PTFE} is the light
1139 collection efficiency for photons exiting PTFE surfaces.

1140 N_{Che} is related to PMT sensitivity, we take the PMT sensitive photon wavelength in the range of
1141 160 nm to 650 nm (the spectral response range for PMT R11410-10, as described in Ref. [1]). N_{Che}
1142 is also related the PTFE refractive index, and electron stopping distance, which are approximately
1143 2 ($\epsilon \sim 4$), and $\sim 10^{-1}$ cm for a 1 MeV electron in PTFE, respectively. The attenuation distance of
1144 photons d_{atten} is ~ 7 cm for a 1 MeV electron for PTFE, from Ref. [29]. The light collection efficiency
1145 LCE_{PTFE} is in the range of 1.5 % to 15 %, as described in Section 1.6. Therefore, taking $d_{\text{to-surface}}$ to
1146 be 0 cm to 1 cm, and taking $f_{\text{to-surface}}$ to be 10 % to 50 %, N_{Che} is ~ 150 , and the estimated number
1147 of Cherenkov photons detected by the PMTs is in the range of up to ~ 10 phe. Even though this
1148 estimated number of photons is not very big, however it is large enough to be seen by both PMTs.
1149 For a muon, we can do a similar estimation with changing the stopping distance to the full length of
1150 muon trajectory in PTFE, which is ~ 5 cm. Therefore, the estimated number of Cherenkov photons
1151 detected by the PMTs in a muon event is in the range of up to ~ 500 phe. The exact number of

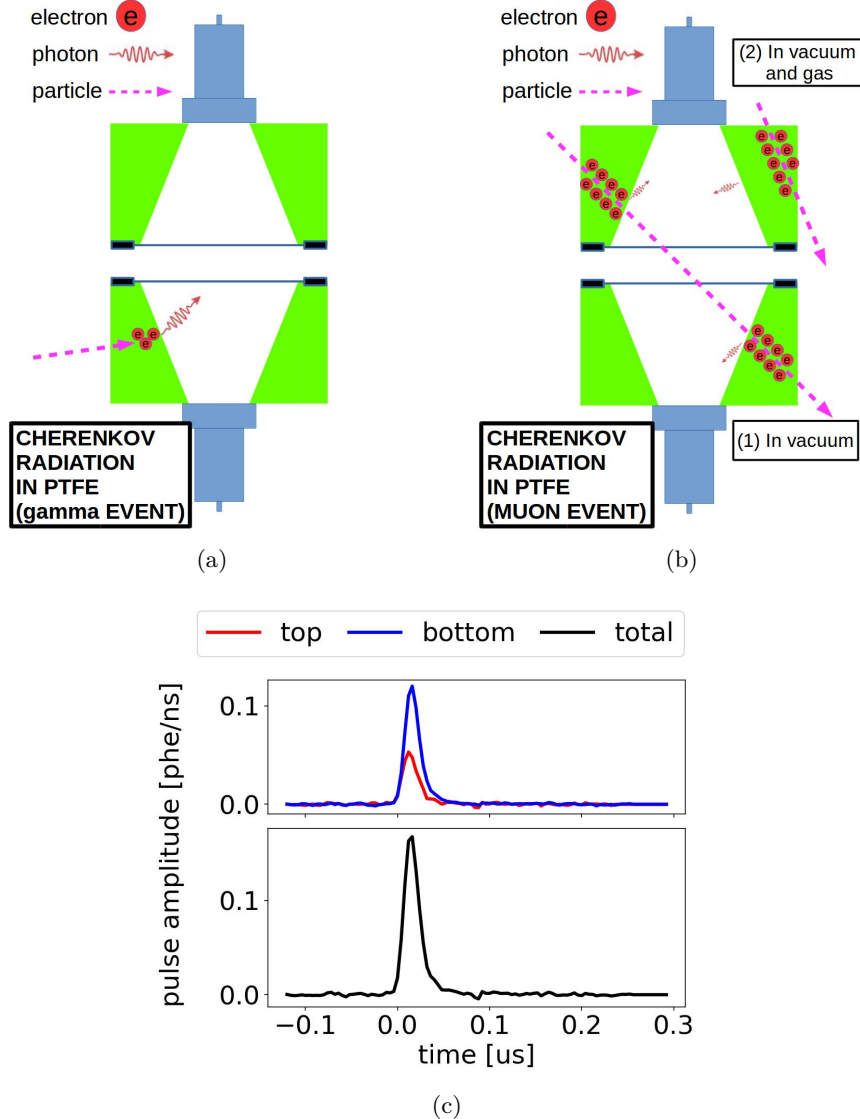


Figure 1.37: *Gas Test* signal: Cherenkov radiation in PTFE. (a) Cartoon of the process in which Cherenkov radiation is produced in PTFE. The Cherenkov radiation comes from the electrons created in a gamma particle event. (b) Cartoon of the process in which Cherenkov radiation is produced in PTFE after a muon particle crossing the detector. (1) If the detector is in vacuum, even though the muon particle crosses the cone regions, there is no primary scintillation or ionization inside the ELD active volume, and only Cherenkov radiation signals from this muon event in PTFE are observed. (2) A muon particle does not cross the cone regions. Cherenkov radiation signals from this muon in PTFE are observed. (c) An example waveform of a Cherenkov radiation event. Data were taken at 2017-12-8 14:02, with grid voltages V_T and V_B at +6 kV and -6 kV, operating gas density at 0.137 mol L^{-1} .

1152 detected Cherenkov photons is hard to predict precisely because of the complicated geometry of
 1153 ELD. However, these estimations conclude that Cherenkov events are one of the visible background
 1154 signals in our detector.

1155 One of the most convincing evidence is the existence of Cherenkov radiation events is that short-
 1156 duration signals are seen in the detector at vacuum condition. Fig. 1.38a shows the signal t_{01-99}
 1157 duration vs. signal area plot from a dataset with grid voltages V_T and V_B at 0kV, operating gas
 1158 density at vacuum. The black box shows the potential events which are considered to be associated
 1159 with Cherenkov radiation process. Since the detector is at vacuum condition, it is lack of other
 1160 photon production processes. These potential Cherenkov radiation events may source from both
 1161 external charged particles and energy loss of external particles, likely an external higher energy
 1162 photon (gamma radiation), or a cosmic ray muon. This process is described below: An external
 1163 particle travels through the PTFE cones, lose its energy, ionizes molecules in PTFE and radiates
 1164 photon along its trajectory. Since muon particles are usually more energetic than other external
 1165 particles like gamma radiation, the Cherenkov radiation from muon events is usually larger. This
 1166 is one explanation for the “hot spot” at $(10^2, 10^2)$ in Fig. 1.38a. When the detector is filled with
 1167 xenon gas, the muon particle can also ionize xenon gas atoms inside ELD active volume. This
 1168 process produces scintillation photons and ionization electrons, and the EL process associated with
 1169 ionization electrons usually increases signal duration. It explains the reason that this “hot spot”
 1170 shifts between vacuum data and xenon gas data. Details for explanations of muon events in xenon
 1171 gas data are in Section. ???. The signals with their area in the range of 0 phe to 10^2 phe and signal
 1172 duration in the range of 0 ns to 2×10^2 ns in Fig. 1.38a are likely to be Cherenkov radiation events
 1173 from muons that do not cross the ELD active region and external gamma radiation induced fast
 1174 electrons in PTFE (and PMT window). The gamma radiation can scatter electrons in PTFE. These
 1175 fast-moving scattered electrons can also produce Cherenkov radiation light. When the detector is
 1176 filled with xenon gas, the same physical processes of Cherenkov radiation from muon and gamma
 1177 radiation remain. Therefore, these processes explain why a similar population of Cherenkov radiation
 1178 events exist in both vacuum data (Fig. 1.38a) and xenon gas data (Fig. 1.38b).

1179 **Discharge** Discharges happen inside and outside the ELD could produce signals that can be seen
 1180 by the PMTs. In sparking tests, we observe discharges on the high voltage feed throughs and cables,
 1181 which are caused by the smoothness of the high voltage surfaces (especially metallic surfaces) are
 1182 imperfect. This imperfection creates a high field region, and initialized a high
 1183 ionization probability of the medium (especially gas medium) surrounding it and causes a discharge.
 1184 The quantity of light production of these discharges has a various range and usually are big. However,
 1185 depending on the location of the discharge, signals of the discharge have different appearances. The
 1186 discharges happening outside the ELD may end up having one or several SPHEs in each PMTs with
 1187 regard to the poor light collection at such location. However, the discharges happening inside the
 1188 ELD may look like electron emission signals.

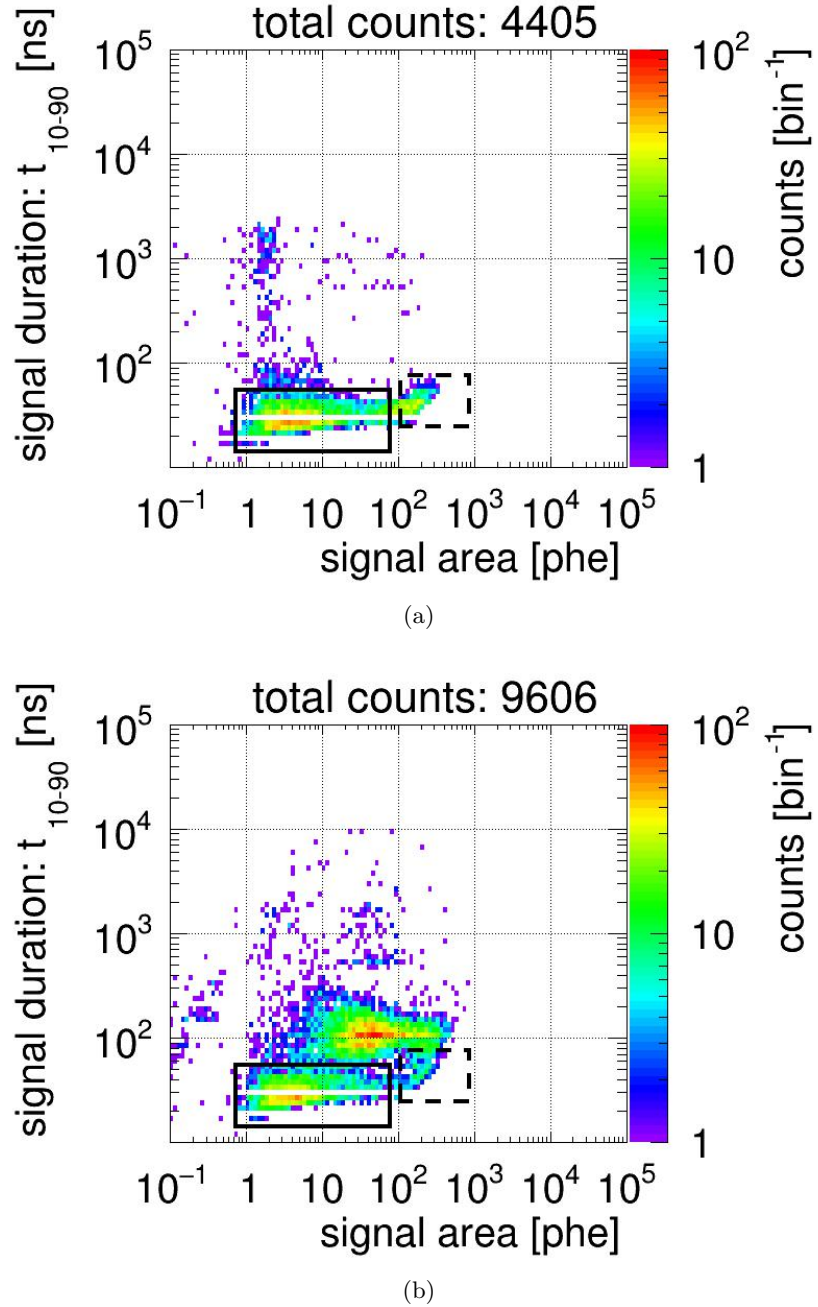


Figure 1.38: *Gas Test* signal t_{10-90} duration vs. signal area. (a) Vacuum data. Data were taken at 2018-03-12 11:41, with grid voltages V_T and V_B at 0 kV, operating gas density at vacuum. (b) Xenon gas data. Data were taken at 2017-12-8 13:12, with grid voltages V_T and V_B at 0 kV, operating gas density at 0.137 mol L^{-1} . The black solid line indicates the muon events which crosses the cone regions. The black dashed line indicates the muon events which do not cross the cone regions, and might also include gamma radiation events in PTFE.

1189 1.9 Signal selections

1190 This section discusses signal selections, also known as cuts, that are used in the *Gas Test* analysis.
 1191 The purpose of this analysis is searching for electron emission signals from tested grid wires, and
 1192 correctly estimating the rate of this process. For this purpose, signal selections on different parameter
 1193 spaces are carried out to identify background signals from electron emission signals. **For each signal**
 1194 **selection, the possibility of removing electron emission signalis evaluated.** The primary principle
 1195 of signal selections is to get a clean population of the electron emission signals to get a reliable
 1196 estimation of its rate. Other than that, since electron emission signals are in most situation rare in
 1197 the detector, signal selections of these electron emission signals are done conservatively; that is to
 1198 keep as many candidates for electron emission signals as possible.

1199 An electron emission signal should:

- 1200 • have the correct signal shape, and
- 1201 • be an uncorrelated signal from previous signals in time.

1202 Based on the characteristics we summarized previously about electron emission signal and other
 1203 different signals in the detector, a list of selections are applied successively to get the clean population
 1204 of the electron emission signals. The algorithm of each selection and the event populations each
 1205 selection removes are also discussed.

1206 1.9.1 Signal selections based on signal shape

1207 Signal shape is one of the most important signature for electron emission signals . It includes the
 1208 aspects of the signal area, the signal duration, and the SPHE rate at different time region during
 1209 the event.

1210 coinciding found

1211 **Definition:** Both PMTs have signals that occur within a time difference smaller than CWW.

1212 **Purpose:** This selection is to make sure that the signal of interest is unlikely to be from a dark
 1213 current signal in one PMT, or SPHE from other sources in one PMT (e.g. fluorescence light from
 1214 PTFE, or light from discharges).

1215 The process of coinciding finding and coinciding event building is discussed in the data processing
 1216 section in Section 1.4. An example result from coinciding event building is shown in Fig. 1.39a. The
 1217 signal area has a various distribution mostly in the range of 10^{-1} phe to 10^5 phe, when the signal
 1218 t_{10-90} duration, and the TBA, top-bottom asymmetry, are mostly distributed in the range of 10^1 ns
 1219 to 10^5 ns and -1 to 1. Several “hot spots” that are seen in the figure correspond to different activities
 1220 in the detector, which will be explained later in each separate section of signal selection. Among

1221 these “hot spots”, the horizontal strap shape spot at signal area in the range of 10^1 phe to 10^2 phe,
 1222 signal t_{10-90} duration in the range of 10^3 ns to 10^4 ns, is likely to contain the potential electron
 1223 emission signals. The locations and the counts of different “hot spots”, including the “hot spot” of
 1224 electron emission signals, change as varying ΔV_{T-B} and operating gas density, mainly because of the
 1225 changes of the duration and the intensity of the EL process.

1226 Coinciding finding and coinciding event building are the fundamental part of this analysis. Signal
 1227 selections defined later are based on the classification of coinciding-found signals.

1228 **Not a noise-like signal**

1229 **Definition:** A coinciding-found signal has a positive signal area in all PMT channels, a higher
 1230 than 0.5 positive to negative amplitude ratio, and a positive signal t_{10-90} duration.

1231 **Purpose:** This selection is to make sure the signal of interest is not an electrical noise signal,
 1232 which usually has a close to zero signal area, a close to unity positive to negative amplitude ratio,
 1233 or a zero signal t_{10-90} duration, as described in Section 1.8.4. The effect of this selection is shown
 1234 in Fig. 1.39b. Noise-like signals, mostly at signal area in the range of <1 phe, signal t_{10-90} duration
 1235 in the range of $<10^3$ ns, are rejected.

1236 **Not a narrow (S1-like) signal**

1237 **Definition:** A coinciding-found signal has a signal t_{25-75} width (time difference between the time
 1238 of 25th percentile of the signal waveform and the time of 75th percentile of the signal waveform)
 1239 larger than 250 ns, and a signal t_{50} width (time difference between the signal start time and the time
 1240 of 50th percentile of the signal waveform) larger than 320 ns; in other words, the major width of the
 1241 coinciding-found signal is not narrow.

1242 **Purpose:** This selection is to make sure the signal of interest is not a potential (1) Cherenkov
 1243 radiation event, or (2) primary scintillation light (S1) from an external particle (e.g. a γ -ray, or
 1244 a muon), as described in Sections 1.8.4, 1.8.2, and 1.8.3. The effect of this selection is shown in
 1245 Fig. 1.39c. The narrow signals can generally be separated to two categories, corresponding to the
 1246 two “hot spots” in the figure. The first “hot spot” at signal area in the range of 1 phe to 10^2 phe,
 1247 signal t_{10-90} duration in the range of $<5 \times 10^1$ ns, may results from Cherenkov radiation events and
 1248 primary scintillation light of low energy gamma radiation events. The second “hot spot” at signal
 1249 area 10^1 phe to 10^3 phe, signal t_{10-90} duration in the range of 5×10^1 ns to 2×10^2 ns are likely from
 1250 primary scintillation light of gamma radiation events and muon events.

1251 **Not a two-SPHE accidental coinciding signal**

1252 **Definition:** A coinciding-found signal has a signal area larger than 2.5 phe, and at least one PMT
 1253 has a signal t_{25-75} width larger than 35 ns, which is approximately twice the signal width of a SPHE.

1254 **Purpose:** This selection is to make sure the signal of interest is not a accidental coinciding of two
 1255 SPHEs, which are likely from PMT dark current and other SPHE sources, as described in Section ??.
 1256 The effect of this selection is shown in Fig. 1.39d. Two-SPHE accidental coinciding signals, mostly
 1257 at signal area in the range of <2.5 phe, signal t_{10-90} duration in the range of up to $\sim 2 \times 10^3$ ns (this
 1258 upper edge results from coinciding window width (CWW) in coinciding building), are rejected.

1259 **Not a top-heavy signal**

1260 **Definition:** A coinciding-found signal does not have a “top-heavy” TBA regarding its signal area.
 1261 A signal-area-dependent cut on TBA is used rather than a fixed TBA value is to account for the
 1262 statistically fluctuation of the TBA at low signal area region, because the counts of photons that
 1263 the top and bottom PMT detected are low.

1264 A “top-heavy” TBA is defined as assuming the photon counts in top PMT (T) has a binomial
 1265 distribution of parameter p (success probability in a single trial) and N (number of trials), the
 1266 survival function (SF) at $T = T_{\text{detected}}$ is smaller than 10^{-5} :

$$SF(T_{\text{detected}}) \equiv P(T > T_{\text{detected}}) = \sum_{T_{\text{detected}}}^{\infty} P(T) dT < 10^{-5} \quad (1.32)$$

$$P(T; p, N) = \binom{N}{T} p^T (1-p)^{N-T} \quad (1.33)$$

1267 where $p = B_{\text{detected}} \times 1.025/N$; T_{detected} , B_{detected} are the top and bottom PMT measured signal area
 1268 in phe; and N is a sufficiently large number, chosen to be 10^6 . A low $SF(T_{\text{detected}})$ indicates a high
 1269 TBA.

1270 **Purpose:** This selection is to make sure the signal of interest is not from (1)an anode cone event,
 1271 (2) an anode muon cone event, (3) a PMT saturation event, or (4) a signal which misses part of the
 1272 recording in the bottom PMT (likely because of PMT dead time), as described in Sections 1.8.2,
 1273 1.8.3, and 1.2. The effect of this selection is shown in Fig. 1.39e. The four categories of background
 1274 events correspond to the four “hot spots” in the figure.

1275 The “hot spot” at signal area in the range of 10^2 phe to 10^3 phe, signal t_{10-90} duration in the
 1276 range of $\sim 10^3$ ns to 10^4 ns, and TBA ~ 0.3 , results from EL light in the anode cone gamma radiation
 1277 events. This “hot spot” is a combination of two smaller “hot spots”. The “hot spot” on the left
 1278 (signal area $\sim 2 \times 10^2$ phe, signal t_{10-90} duration $\sim 2 \times 10^3$ ns, and TBA ~ 0.3) may result from xenon
 1279 X-rays events with typical energy of 33 keV in the anode cone . A xenon X-ray event in average can

1280 create $\sim 1.5 \times 10^3$ drifted electrons,⁴ which produce EL light in the high electric field region around
 1281 the anodic grid wires. The “hot spot” on the right corresponds to other higher energy gamma
 1282 radiation.

1283 The location of this “hot spot” in the figure moves as varying ΔV_{T-B} . As ΔV_{T-B} increases, the
 1284 electric field strength around the anodic grid wires also increases, which causes higher quantity of
 1285 EL light production and signal area. At a low ΔV_{T-B} , the small area signals cannot be rejected by
 1286 this selection. Therefore, another signal selection based on the time correlation between the signal
 1287 of primary scintillation and the signal of EL of these events, is carried out, as described later in
 1288 Section 1.9.2.

1289 The “hot spot” at signal area $\sim 10^4$ phe, signal t_{10-90} duration $\sim 10^4$ ns, results from EL light
 1290 in the anode cone muon events. Similar to anode cone event from gamma radiation, these events
 1291 also produce free drifted electrons, which produce EL light in the high elelctric field region around
 1292 the anodic grid wires. The duration of these muon events are much longer than that of gamma
 1293 events is because the longer ionization track of a muon event causes the drifted electrons created in
 1294 the muon event arrive the anodic grid and produce EL light in a wider time span, as described in
 1295 Section 1.8.3. The location of this “hot spot” in the figure moves to high signal area as increasing
 1296 ΔV_{T-B} . Therefore, the same argument holds for the signal selection based on the time correlation is
 1297 used to reject these signals.

1298 The “hot spot” strap at signal area $\sim 10^4$ phe, signal t_{10-90} duration $\sim 10^3$ ns, and TBA ~ 0.1
 1299 results from high energy particle and muon events which saturate the DAQ. Because the average
 1300 SPHE amplitude in the bottom PMT is higher, it exceeds the upper limit of the DAQ dynamic
 1301 range at a smaller counts of SPHE than the top PMT. Therefore, the reconstructed signal area in
 1302 the bottom PMT is lower after it reaches the DAQ saturation limit, which leads to a higher signal
 1303 TBA because of this DAQ saturation issue.

1304 The “hot spot” at TBA ~ 1 results from missing part of the recording in the bottom PMT ,which
 1305 is most likely because of PMT dead time. In these signals, the top PMT records the full event, when
 1306 the bottom PMT only records the beginning or the end of the event. This results in a close to unity
 1307 signal TBA.

1308 Not a bottom-heavy signal

1309 **Definition:** A coinciding-found signal does not have a “bottom-heavy” TBA regarding its signal
 1310 area.

1311 Similar to the “top-heavy” TBA, a “bottom-heavy” TBA is defined as assuming the photon
 1312 counts in bottom PMT (B) has a binomial distribution of parameter p (success probability in a
 1313 single trial) and N (number of trials), the survival function (SF) at $B = B_{\text{detected}}$ is smaller than

⁴The average energy to create an electron-ion pair in xenon gas (W_{ion}) is 22 eV for a gamma particle, estimated from W_{ion} for an alpha particle and a beta particle in Ref. [25–27].

₁₃₁₄ 10^{-5} :

$$SF(B_{\text{detected}}) \equiv P(B > B_{\text{detected}}) = \sum_{B_{\text{detected}}}^{\infty} P(B) dB < 10^{-5} \quad (1.34)$$

$$P(B; p, N) = \binom{N}{B} p^B (1-p)^{N-B} \quad (1.35)$$

₁₃₁₅ where $p = T_{\text{detected}}/0.825/N$; T_{detected} , B_{detected} are the top and bottom PMT measured signal area
₁₃₁₆ in phe; and N is a sufficiently large number, chosen to be 10^6 . A low $SF(B_{\text{detected}})$ indicates a low
₁₃₁₇ TBA.

₁₃₁₈ **Purpose:** This selection is to make sure the signal of interest is not a signal which misses part of
₁₃₁₉ the recording in the top PMT (likely because of PMT dead time), as described in Section 1.2, which
₁₃₂₀ is similar to the situation described in Section 1.9.1.

₁₃₂₁ The effect of this selection is shown in Fig. 1.39f. Signals with TBA close to -1 are rejected
₁₃₂₂ because they are likely to be a signal missing part of the recording in the top PMT.

₁₃₂₃ In reverse polarity operation when the top grid is cathodic and the bottom grid is anodic, the
₁₃₂₄ roles of “top-heavy” and “bottom-heavy” signal selections switches from normal polarity operation.

₁₃₂₅ Not a extremely long duration signal

₁₃₂₆ **Definition:** A coinciding-found signal has a signal t_{01-99} duration 1.5 times longer than the pre-
₁₃₂₇ dicted EL duration from the estimated average EL region electric field and Eqn. 1.17.

₁₃₂₈ **Purpose:** This selection is to make sure the signal of interest is not a muon event or a multiple
₁₃₂₉ scatter event, as described in Sections 1.8.3 and 1.8.2. The effect of this selection is shown in
₁₃₃₀ Fig. 1.39g. The “hot spot” at signal area $\sim 10^4$ phe, signal t_{10-90} duration $\sim 3 \times 10^3$ ns, and TBA
₁₃₃₁ ~ 0 results from EL region muon events.

₁₃₃₂ Not a right-angle triangle shape signal

₁₃₃₃ may be remove this cut.

₁₃₃₄ **Definition:** A coinciding-found signal does not have a large skewness of signal waveform and a
₁₃₃₅ higher photon rate at the beginning of the signal than that at the end of the signal.

₁₃₃₆ The skewness statistics of a electron emission signal waveform is close to zero because the shape is
₁₃₃₇ close to a uniform distribution, when the skewness of a right-angle triangle shape is ~ 0.96 . Therefore,
₁₃₃₈ this statistics is used to distinguish the right-angle triangle waveform. The skewness statistics
₁₃₃₉ between 5th percentile time and 95th percentile time (skew_{05-95}) and the skewness statistics between

1340 15th percentile time and 85th percentile time (skew_{15-85}) are used to effect from the outlier. A large
1341 skewness is defined as $\text{skew}_{05-95} > 0.2$ and $\text{skew}_{15-85} > 0.1$.

1342 Since the skewness statistics are sometimes effected by outlier, another method is carried out
1343 based on comparing the photon rate the beginning of the signal and that at the end of the signal
1344 as a supplement. A higher photon rate at region A than region B is defined below. The detected
1345 signal area and duration of region A and region B is noted as A_{detected} , B_{detected} , t_A , t_B . Assuming
1346 the photon counts in region A in a simulation (A_{sim}) has a binomial distribution of parameter p
1347 (success probability in a single trial) and N (number of trials), the survival function (SF) at $A_{\text{sim}} =$
1348 A_{detected} is smaller than 10^{-6} :

$$SF(A_{\text{detected}}) \equiv P(A_{\text{sim}} > A_{\text{detected}}) = \sum_{A_{\text{detected}}}^{\infty} P(A) dA < 10^{-6} \quad (1.36)$$

$$P(A; p, N) = \binom{N}{A} p^A (1-p)^{N-A} \quad (1.37)$$

1349 where $p = 1.2 \times B_{\text{detected}} \times t_A/t_B/N$; and N is a sufficiently large number, chosen to be 10^6 . A low
1350 SF (A_{detected}) indicates a higher photon rate at region A than region B. If the photon rate between
1351 the 5th and 15th time percentiles, or between 300 and 800 ns after the recording start time of the
1352 event, is higher than that between the 50th and 80th time percentiles, we say that the signal has a
1353 higher photon rate at the beginning than at the end.

1354 **Purpose:** This selection is to make sure the signal of interest is not a EL region muon event, or a
1355 S1 S2 event in the EL region, as described in Sections 1.8.3 and 1.8.2. The muon events happening
1356 between the grid rings has a lower light production and light collection than those happening between
1357 the grid wires. These grid-ring-region events usually does have a “long tail” in the signal because the
1358 muon track does not pass the anode region creating free drifted electrons. These two reasons make
1359 it hard to distinguish muon events happening between the grid rings by a long signal duration or a
1360 large signal area as that between the grid wires. The effect of this selection is shown in Fig. 1.39h.
1361 Therefore, this selection is used.

1362 **Not an S1 S2 like signal**

1363 **may be remove this cut.**

1364 **Definition:** A coinciding-found signal does not have a low photon rate in the range of 300 ns to
1365 800 ns since the recording start time of the signal.

1366 Since in this type of events, the photon rate is low between the S1 and S2 signal, we compare the
1367 photon rate in the time region immediately after S1 to other time region to distinguish these events.
1368 An S1 signal usually lasts less than 180 ns, therefore ending 300 ns after the recording start time of

1369 the signal, because of the pre-delay recording described in Sections 1.2 and 1.4. The compared region
1370 are between 800 ns since the recording start time of the signal and 90th percentile time, between
1371 25th percentile time and 90th percentile time, between 50th percentile time and 75th percentile
1372 time, and between 50th percentile time and 95th percentile time.

1373 **Purpose:** This selection is to make sure the signal of interest is not from an S1 S2 event in the
1374 cathode corner, as described in Section 1.8.2. The effect of this selection is shown in Fig. 1.39i.

1375 **Not a saturated signal**

1376 **Definition:** A coinciding-found signal does not have any PMT saturated.

1377 **Purpose:** This selection is to make sure the signal of interest is not from a particle or muon event
1378 that have large signal area, unlike electron emission signal which usually does not produce large
1379 signal that saturate any PMT. The effect of this selection is shown in Fig. 1.39j.

1380 **Not a long duration signal**

1381 **Definition:** A coinciding-found signal has a signal t_{10-90} duration 1.5 times longer than the pre-
1382 dicted electron emission signal signal t_{10-90} duration from the estimated average EL region electric
1383 field and Eqn. 1.17.

1384 **Purpose:** This selection is to make sure the signal of interest is not a muon event or a multiple
1385 scatter event, as described in Sections 1.8.3 and 1.8.2. The effect of this selection is shown in
1386 Fig. 1.39k.

1387 **Not a short duration signal**

1388 **Definition:** A coinciding-found signal has a signal t_{10-90} duration shorter than 0.64 times the
1389 predicted electron emission signal duration from the estimated average EL region electric field and
1390 Eqn. 1.17, and shorter than 5 sigma from the predicted electron emission signal signal t_{10-90} duration
1391 duration.

1392 **Purpose:** This selection is to make sure the signal of interest is not a grid ring region event (likely
1393 originating from muon or particle), as described in Sections 1.8.3 and 1.8.2. The effect of this
1394 selection is shown in Fig. 1.39l. An event happening in the grid ring region has low light collection
1395 efficiency and is therefore hard to be distinguished by its shape. However, it usually has a shorter
1396 duration, and can therefore be rejected by this selection.

1397 1.9.2 Signal selections based on previous signals

1398 Previous signals may correlate with the later signals. There are two major types of correlation signals.
1399 One type of correlation signals is between primary scintillation light and EL light from the ionization
1400 electrons. In an anode cone region event, primary scintillation light are produced immediately after
1401 a particle interaction, when the ionization electrons take time to drift to the anodic grid to produce
1402 EL light, as described in Sections 1.8.2 and 1.8.3. Therefore, we can the correlation between primary
1403 scintillation light and EL light to determine these events. The second type of correlation signals is
1404 fluorescence signals succeeding large-area signals, as described in Section 1.8.4. Since the fluorescence
1405 signals may look like electron emission signals, the correlation between the fluorescence signals and
1406 the large-area signals is the only method to distinguish these fluorescence signals. Therefore, we use
1407 signal selections based on the previous signal area to reject these background events.

1408 Moreover, previous signals also introduce PMT dead time issue, as described in Section 1.2.
1409 PMT dead time issue causes an incomplete recording of the signals immediately following another
1410 signal. To address this issue, we subtract a segment of time after each recorded pulse from the live
1411 time of study and eliminate all signals that is recorded in this time period. Therefore, we use signal
1412 selections based on the previous signal duration to reject these background events.

1413 These two signal selections previously mentioned may veto good candidate electron emission
1414 signals . Therefore, the survival ratio of the candidate electron emission signals from these signal
1415 selection need to be estimated.

1416 Previous signal area veto

1417 **Definition:** A coinciding-found signal (1) is not following another pulse in any PMT with pulse
1418 area larger than 3.5 phe within $150\ \mu s$, (2) is not following another pulse in any PMT with pulse
1419 area larger than 10^3 phe within $300\ \mu s$, and (3) is not following another pulse in any PMT with pulse
1420 area larger than 10^4 phe within $1000\ \mu s$.

1421 **Purpose:** The 150-us veto is to make sure that the signal of interest is not the EL light from an
1422 anode cone region event, as described in Sections 1.8.2 and 1.8.3. Primary scintillation light signals
1423 and EL signals are related in time in anode cone region events. Therefore, this veto can reject the
1424 anode cone region event EL signal which usually happens after the primary scintillation light signals.
1425 The time difference between the two signals is the time that takes ionization electrons to drift to
1426 the anodic grid, which is smaller than $150\ \mu s$ for anodic grid voltage V_A larger than 3 kV. Primary
1427 scintillation light signals mostly have their pulse area larger than 3 phe in at least one PMT, which
1428 drives the choice of pulse area value for this selection.

1429 The 200-us veto and the 1000-us veto are to make sure that the signal of interest is not fluorescence
1430 signals succeeding large-area signals, as described in Section 1.8.4. With the segment of time cut

1431 off, the fluorescence induced SPHE rate is below 10^4 Hz, therefore the rate of accidental coinciding
1432 with more than 3 phe is below 4 Hz for the chosen CWW.

1433 The effect of this selection is shown in Fig. 1.39m. Even though not shown in this figure, this
1434 selection is also effective in removing the “hot spot” at signal area in the range of 10^2 phe to 10^3 phe,
1435 signal t_{10-90} duration in the range of $\sim 10^3$ ns to 10^4 ns, and TBA ~ 0.3 , resulting from EL light in
1436 the anode cone gamma radiation events, which is shown in Fig. 1.39e. This selection is necessary
1437 when ΔV_{T-B} is small because the signal selection based on TBA is less effective in such ΔV_{T-B} , as
1438 discussed in Section 1.9.1 .

1439 **Previous signal duration veto**

1440 **Definition:** A coinciding-found signal (1) is not following another pulse in any PMT within $10\ \mu s$,
1441 (2) is not following another pulse in any PMT with pulse duration longer than $3\ \mu s$ within $20\ \mu s$, (3)
1442 is not following another pulse in any PMT with pulse duration longer than $10\ \mu s$ within $40\ \mu s$, and
1443 (4) is not following another pulse in any PMT with pulse duration longer than $30\ \mu s$ within $200\ \mu s$.

1444 **Purpose:** This selection is to make sure the PMT dead time issue is addressed. The effect of this
1445 selection is shown in Fig. 1.39n. Since this selection overlaps with other selections applied previously,
1446 in this particular example figure, few events are removed by this selection.

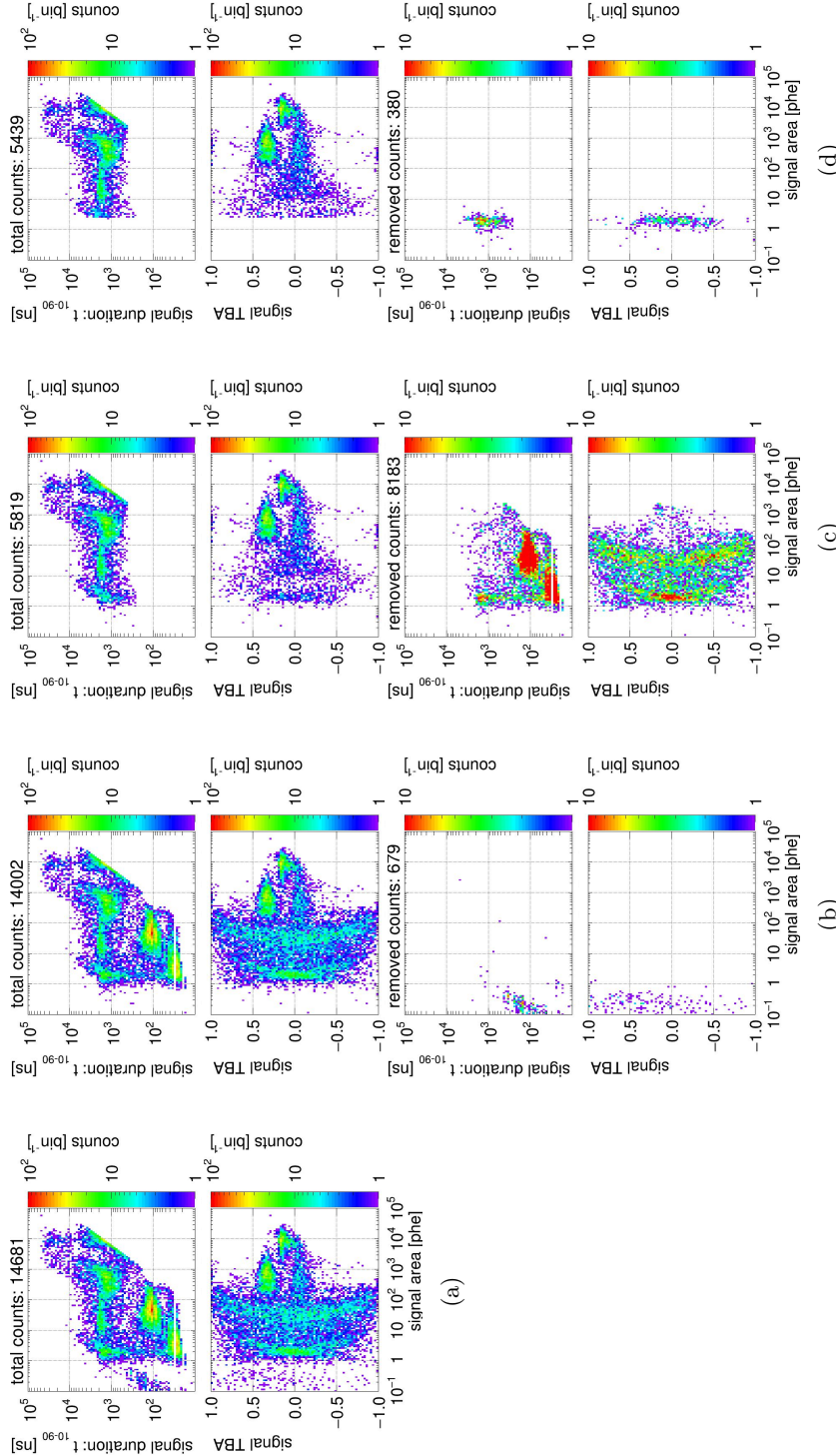


Figure 1.39: *Gas Test* signal selection (part 1): (row one) distribution of t_{10-90} duration vs area after signal selections; (row two) distribution of TBA vs area after signal selections; (row three) distribution of t_{10-90} duration vs area of removed signals; (row four) distribution of TBA vs area of removed signals; (a) coinciding event building; (b) applying signal selections up to “not a noise-like signal”; (c) applying signal selections up to “not a narrow (S1-like) signal”; (d) applying signal selections up to “not a two-SPHE accidental coinciding signal”. The cuts described in the text are applied successively from panel to panel. See the main text for detailed descriptions of the event populations. Data were taken at 2017-12-8 14:02, with grid voltages V_T and V_B at +6 kV and -6 kV, operating gas density at 0.137 mol L^{-1} . The duration of data taking is 180.09 s.

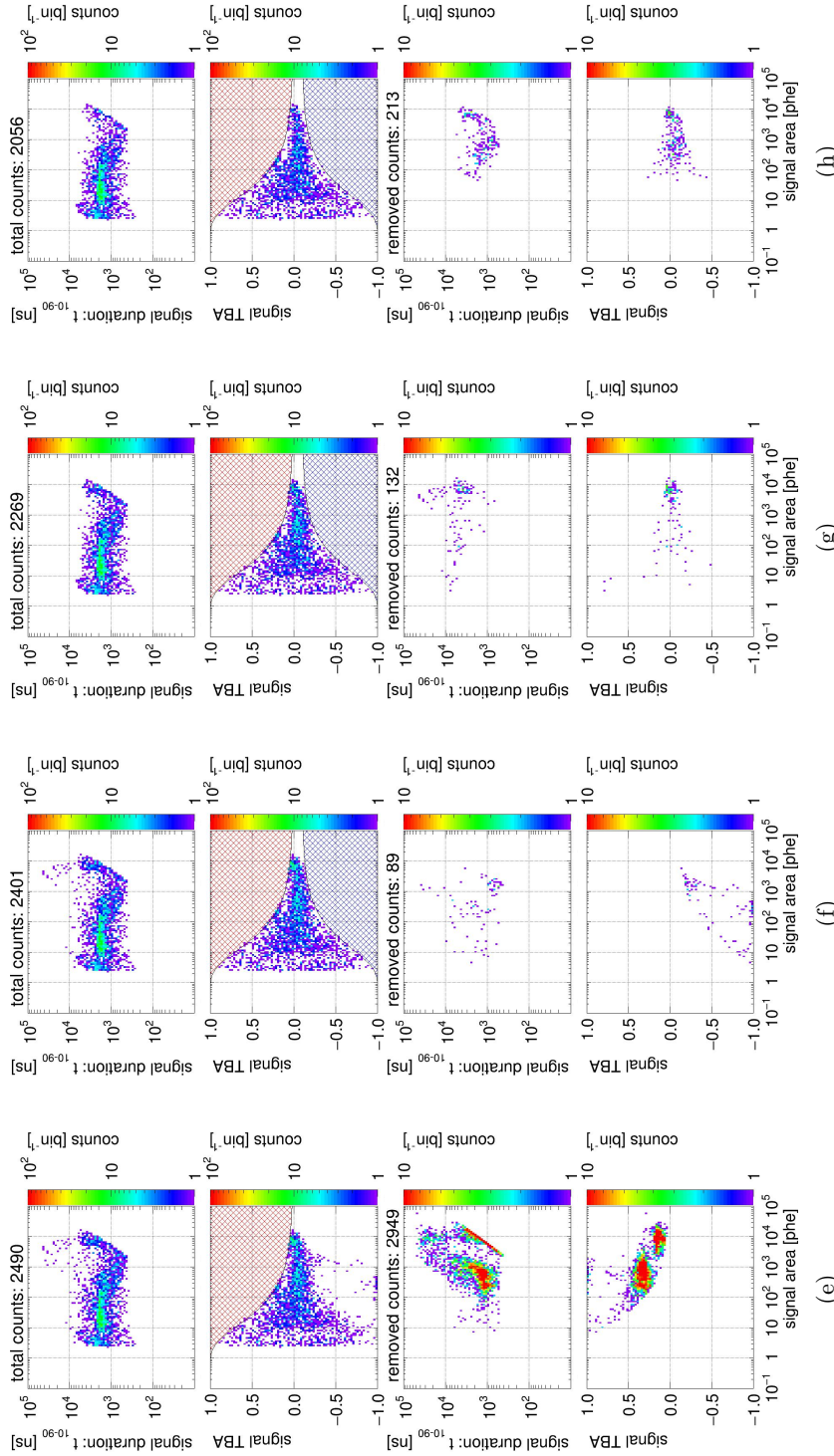


Figure 1.39: *Gas Test* signal selection (part 2): (row one) distribution of t_{10-90} duration vs area after signal selections; (row two) distribution of TBA vs area after signal selections; (row three) distribution of t_{10-90} duration vs area of removed signals; (row four) distribution of TBA vs area of removed signals; (e) applying signal selections up to “not a top-heavy signal”; (f) applying signal selections up to “not a bottom-heavy signal”; (g) applying signal selections up to “not a extremely long duration signal”; (h) applying signal selections up to “not a right-angled triangle shape signal”. The red hatched area indicates the “top-heavy” region. The blue shaded area indicates the “bottom-heavy” region. The cuts described in the text are applied successively from panel to panel. See the main text for detailed descriptions of the event populations. Data were taken at 2017-12-8 14:02, with grid voltages V_T and V_B at $+6\text{kV}$ and -6kV , operating gas density at 0.137 mol L^{-1} . The duration of data taking is 180.09 s.

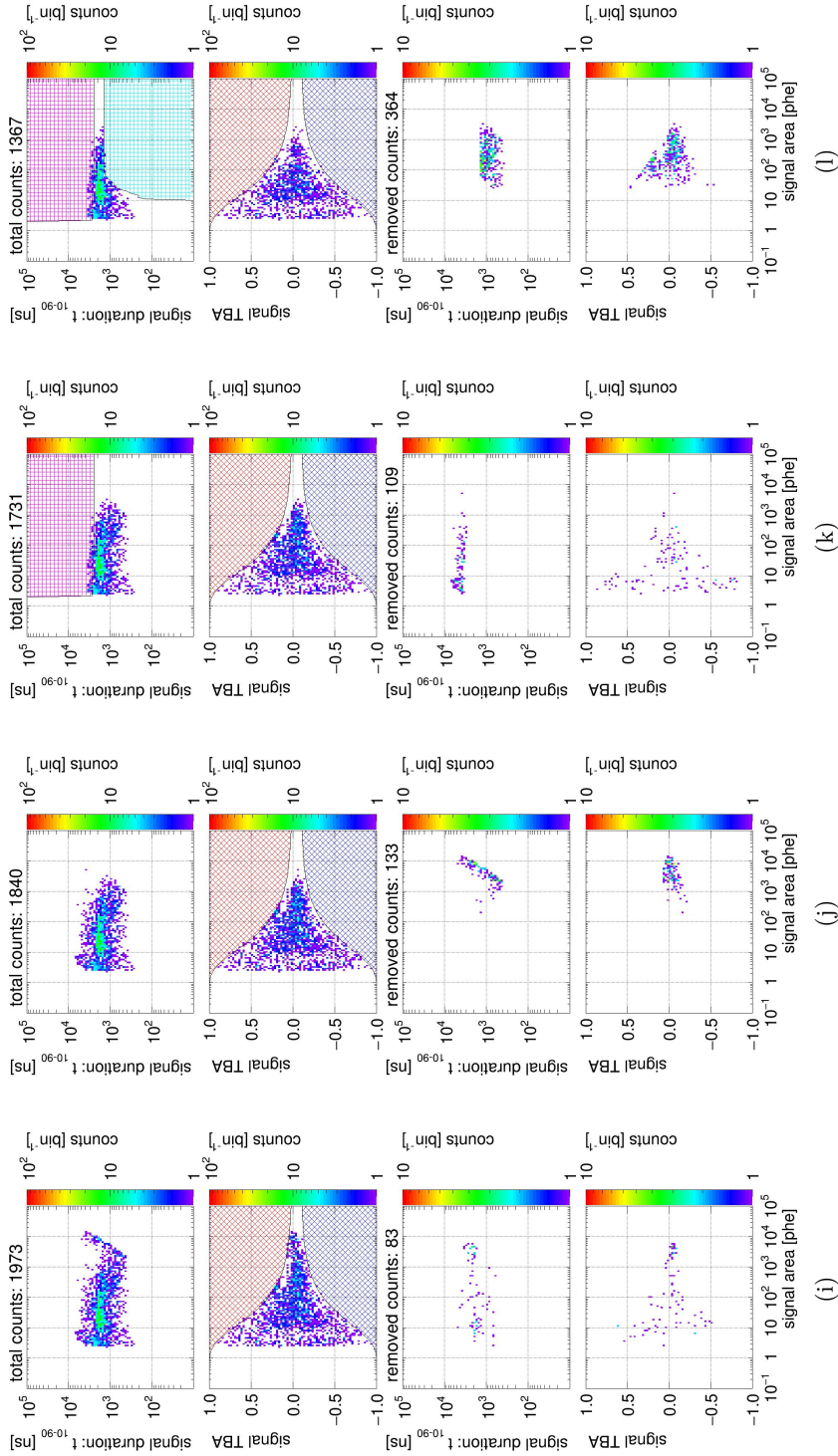


Figure 1.39: *Gas Test* signal selection (part 3): (row one) distribution of t_{10-90} duration vs area after signal selections; (row two) distribution of TBA vs area after signal selections; (row three) distribution of t_{10-90} duration vs area of removed signals; (row four) distribution of TBA vs area of removed signals; (i) applying signal selections up to “not an S1 S2 like signal”; (j) applying signal selections up to “not a saturated signal”; (k) applying signal selections up to “not a long duration signal”. The blue shaded area indicates the “top-heavy” region. The red hatched shaded area indicates the “bottom-heavy” region. The magenta hatched shaded area indicates the “short duration” region. The cyan hatched shaded area indicates the “long duration” region. The cuts described in the text are applied successively from panel to panel. See the main text for detailed descriptions of the event populations. Data were taken at 2017-12-8 14:02, with grid voltages V_T and V_B at +6 kV and -6 kV, operating gas density at 0.137 mol L^{-1} . The duration of data taking is 180.09 s.

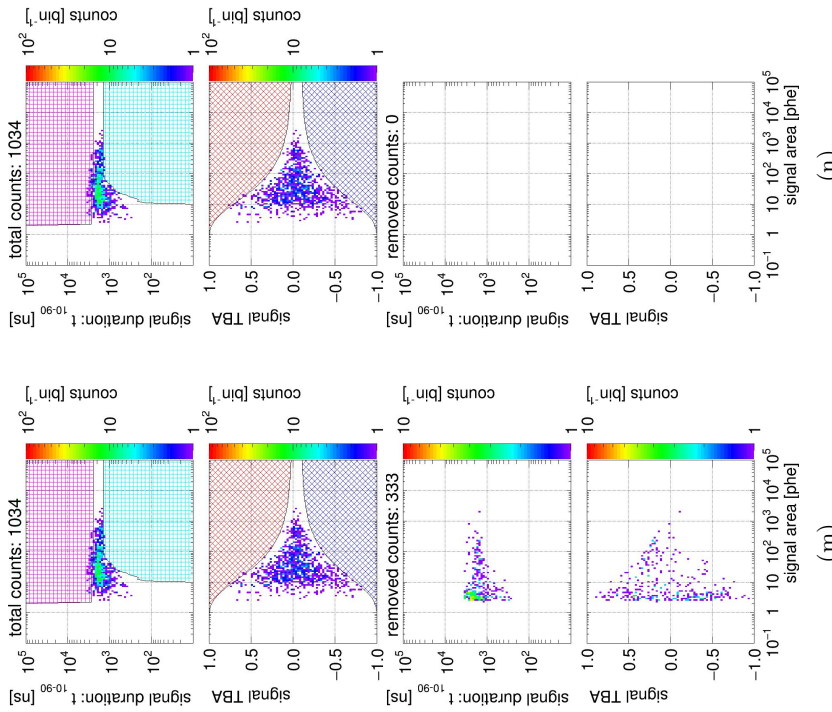


Figure 1.39: *Gas Test* signal selection (part 4): (row one) distribution of t_{10-90} duration vs area after signal selections; (row two) distribution of TBA vs area after signal selections; (row three) distribution of t_{10-90} duration vs area of removed signals; (row four) distribution of TBA vs area of removed signals; (m) applying signal selections up to “previous signal area veto”; (n) applying signal selections up to “Previous signal duration veto”. The red hatched shaded area indicates the “top-heavy” region. The blue shaded area indicates the “bottom-heavy” region. The magenta hatched shaded area indicates the “long duration” region. The cyan hatched shaded area indicates the “short duration” region. The cuts described in the text are applied successively from panel to panel. See the main text for detailed descriptions of the event populations. Data were taken at 2017-12-8 14:02, with grid voltages V_T and V_B at $+6\text{ kV}$ and -6 kV , operating gas density at 0.137 mol L^{-1} . The duration of data taking is 180.09 s.

1447 1.9.3 Signal selections varying ΔV_{T-B} and operating gas density

1448 The results of signal selections

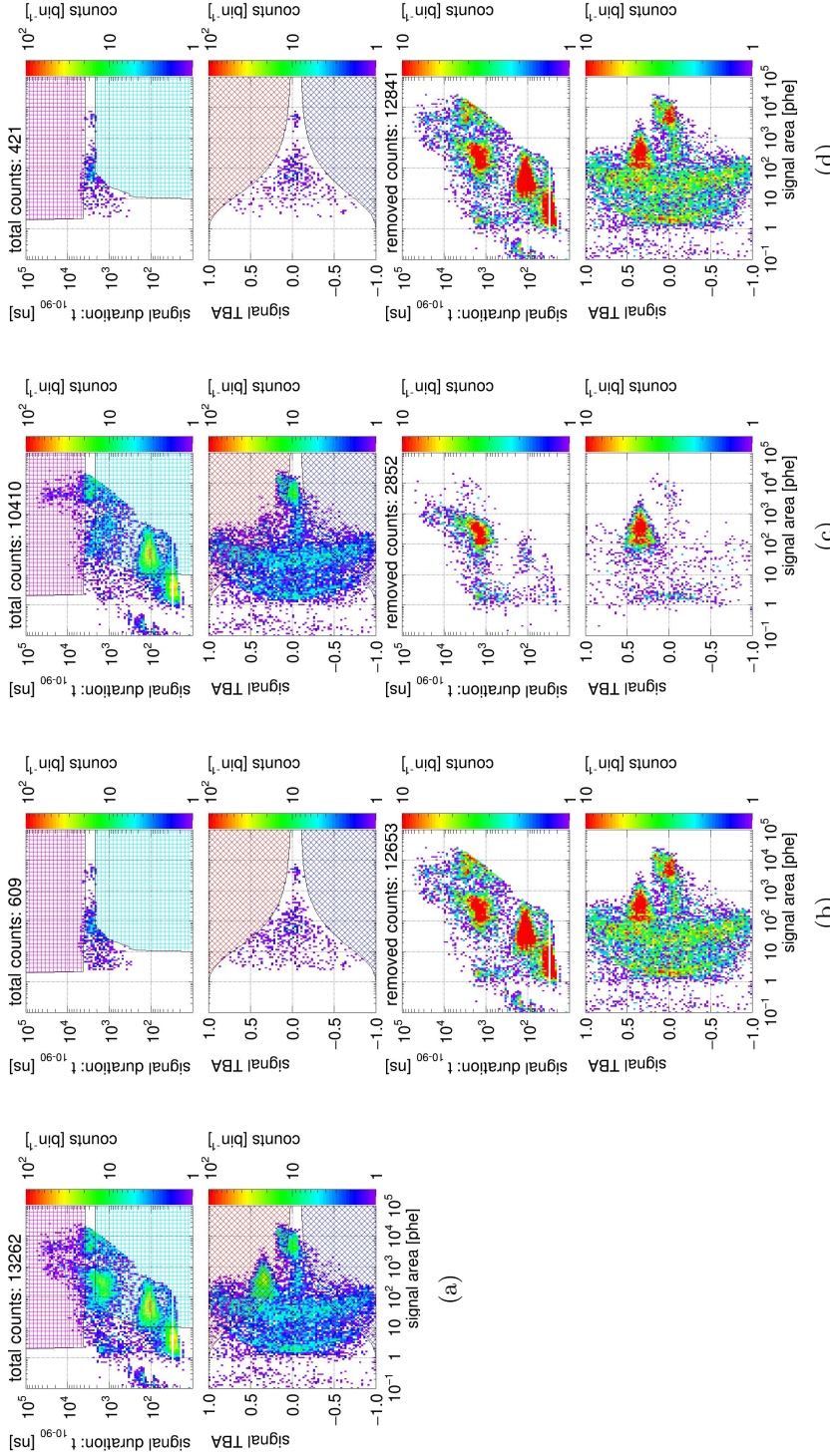


Figure 1.40: *Gas Test* signal selection with ΔV_{T-B} at 8 kV, operating gas density at 0.137 mol L^{-1} : (row one) distribution of t_{10-90} duration vs area after signal selections; (row two) distribution of TBA vs area after signal selections; (row three) distribution of t_{10-90} duration vs area of removed signals; (row four) distribution of TBA vs area of removed signals; (a) coinciding event building; (b) applying signal selections based on signal shape; (c) applying signal selections based on signal shape and based on the previous signals. The red hatched shaded area indicates the “top-heavy” region. The blue shaded area indicates the “bottom-heavy” region. The magenta hatched shaded area indicates the “short duration” region. The cyan hatched shaded area indicates the “long duration” region. Data were taken at 2017-12-8 13:43, with grid voltages V_T and V_B at $+4 \text{ kV}$ and -4 kV . The duration of data taking is 179.95 s.

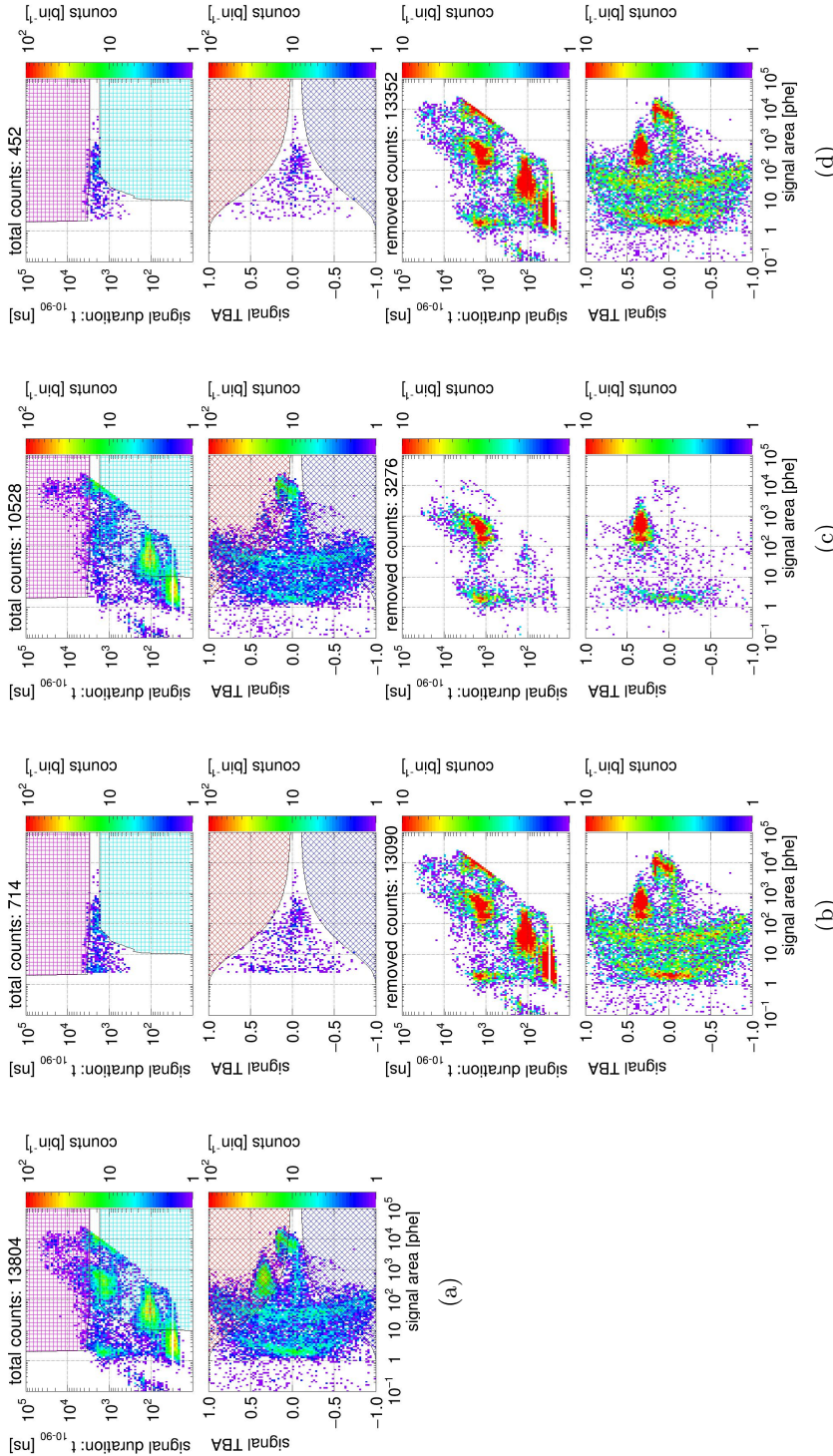


Figure 1.41: *Gas Test* signal selection with ΔV_{T-B} at 10 kV, operating gas density at 0.137 mol L^{-1} . (row one) distribution of t_{10-90} duration vs area after signal selections; (row two) distribution of TBA vs area after signal selections; (row three) distribution of t_{10-90} duration vs area of removed signals; (row four) distribution of TBA vs area of removed signals; (a) coinciding event building; (b) applying signal selections based on signal shape; (c) applying signal selections based on signal shape and based on the previous signals. The red hatched shaded area indicates the “top-heavy” region. The blue shaded area indicates the “bottom-heavy” region. The magenta hatched shaded area indicates the “short duration” region. The cyan hatched shaded area indicates the “long duration” region. Data were taken at 2017-12-8 13:52, with grid voltages V_T and V_B at +5 kV and -5 kV. The duration of data taking is 180.11 s.

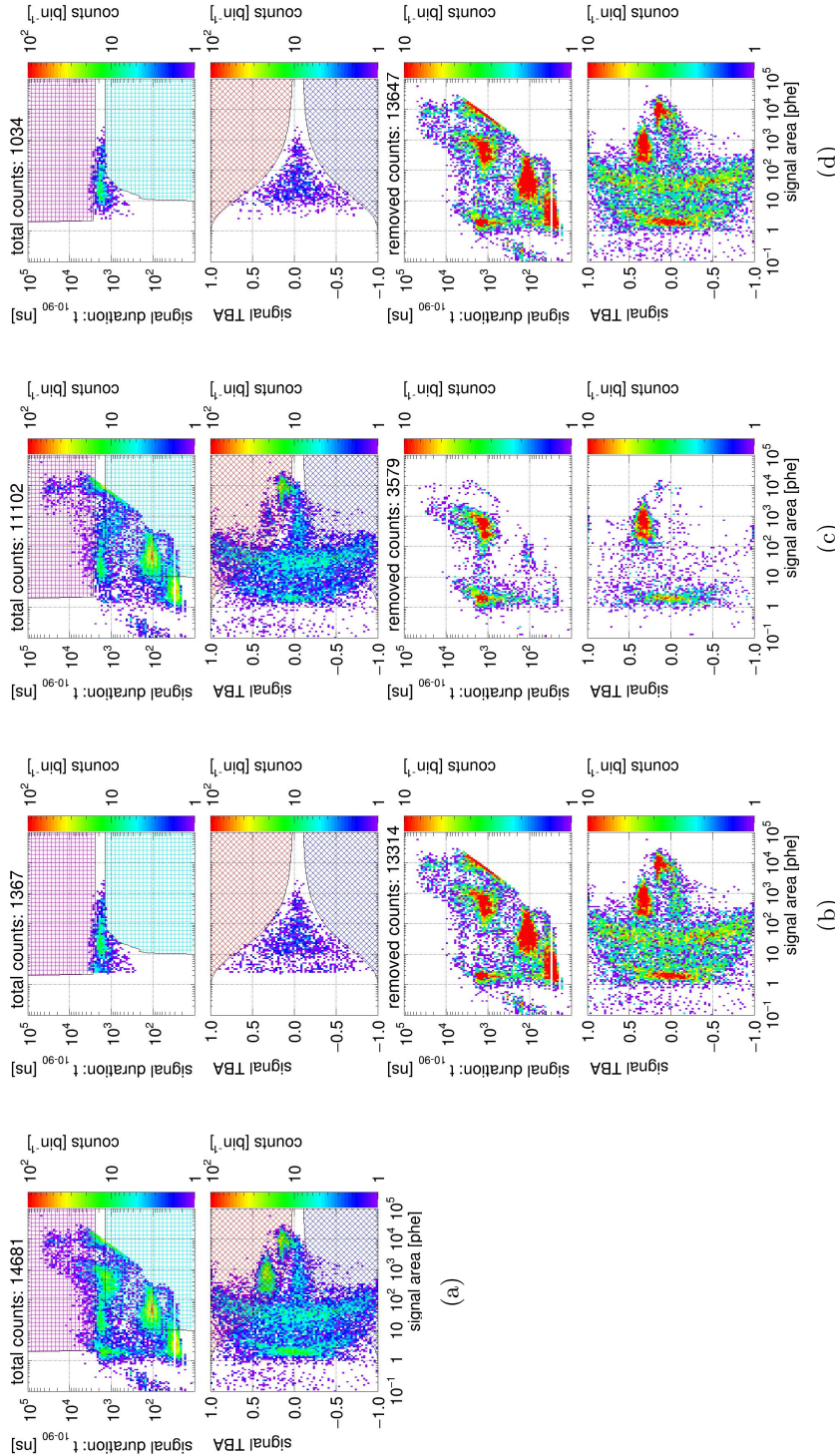


Figure 1.42: *Gas Test* signal selection with ΔV_{T-B} at 12 kV, operating gas density at 0.137 mol L^{-1} ; (row one) distribution of t_{10-90} duration vs area after signal selections; (row two) distribution of TBA vs area after signal selections; (row three) distribution of t_{10-90} duration vs area of removed signals; (row four) distribution of TBA vs area of removed signals; (a) coinciding event building; (b) applying signal selections based on signal shape; (c) applying signal selections based on signal shape and based on the previous signals. The red hatched shaded area indicates the “top-heavy” region. The blue shaded area indicates the “bottom-heavy” region. The magenta hatched shaded area indicates the “long duration” region. The cyan hatched shaded area indicates the “short duration” region. Data were taken at 2017-12-8 14:02, with grid voltages V_T and V_B at $+6 \text{ kV}$ and -6 kV . The duration of data taking is 180.09 s.

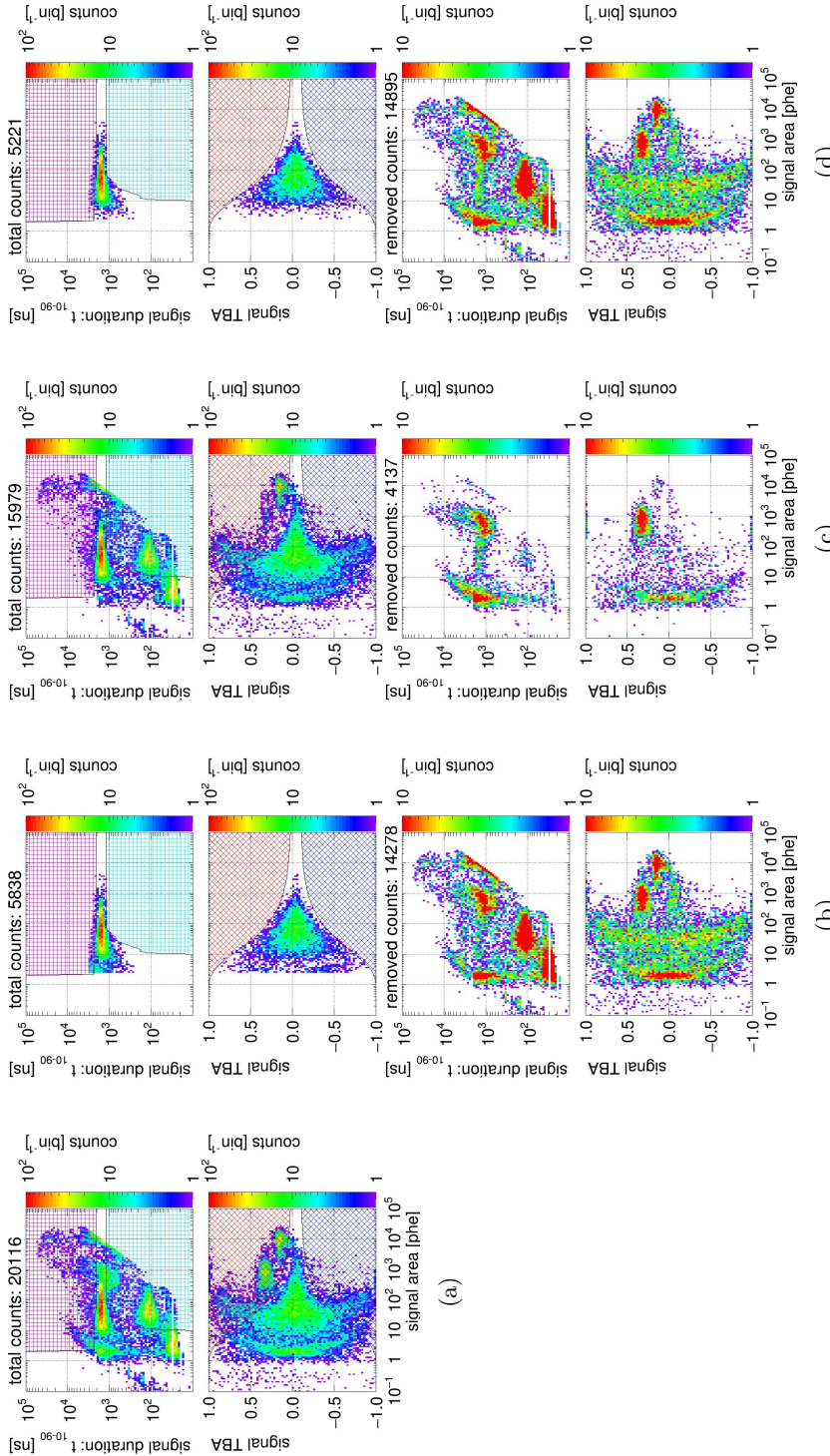


Figure 1.43: *Gas Test* signal selection with ΔV_{T-B} at 14 kV, operating gas density at 0.137 mol L^{-1} . (row one) distribution of t_{10-90} duration vs area after signal selections; (row two) distribution of TBA vs area after signal selections; (row three) distribution of t_{10-90} duration vs area of removed signals; (row four) distribution of TBA vs area of removed signals; (a) coinciding event building; (b) applying signal selections based on signal shape; (c) applying signal selections based on signal shape and based on the previous signals. The red hatched shaded area indicates the “top-heavy” region. The blue shaded area indicates the “bottom-heavy” region. The magenta hatched shaded area indicates the “long duration” region. The cyan hatched shaded area indicates the “short duration” region. Data were taken at 2017-12-8 14:21, with grid voltages V_T and V_B at +7 kV and -7 kV. The duration of data taking is 180.01 s.

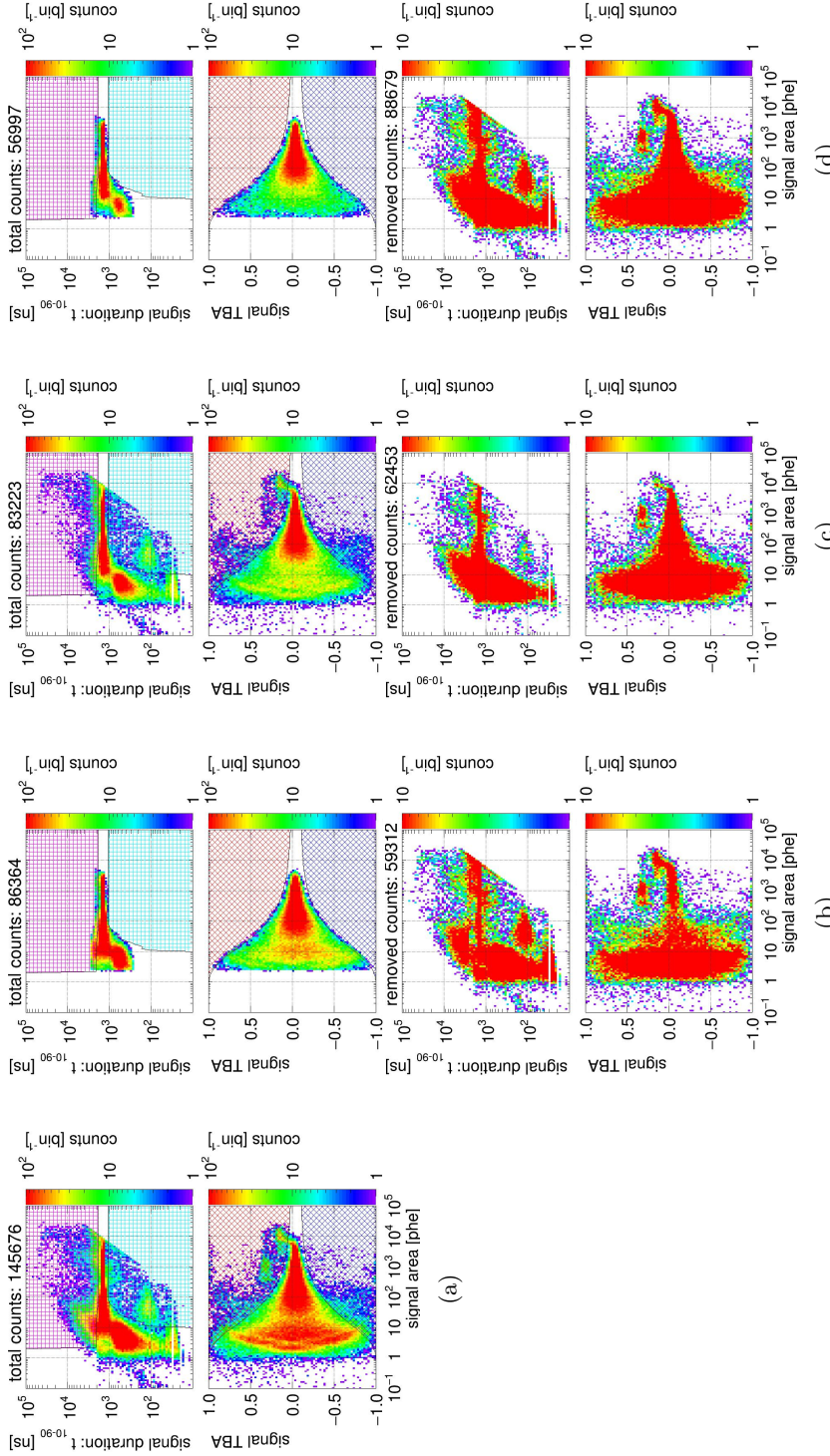


Figure 1.44: *Gas Test* signal selection with ΔV_{T-B} at 16 kV, operating gas density at 0.137 mol L^{-1} . (row one) distribution of t_{10-90} duration vs area after signal selections; (row two) distribution of TBA vs area after signal selections; (row three) distribution of t_{10-90} duration vs area of removed signals; (row four) distribution of TBA vs area of removed signals; (a) coinciding event building; (b) applying signal selections based on signal shape; (c) applying signal selections based on signal shape and based on the previous signals. The red hatched shaded area indicates the “top-heavy” region. The blue shaded area indicates the “bottom-heavy” region. The magenta hatched shaded area indicates the “short duration” region. The cyan hatched shaded area indicates the “long duration” region. Data were taken at 2017-12-8 14:42, with grid voltages V_T and V_B at +8 kV and -8 kV. The duration of data taking is 180.10 s.

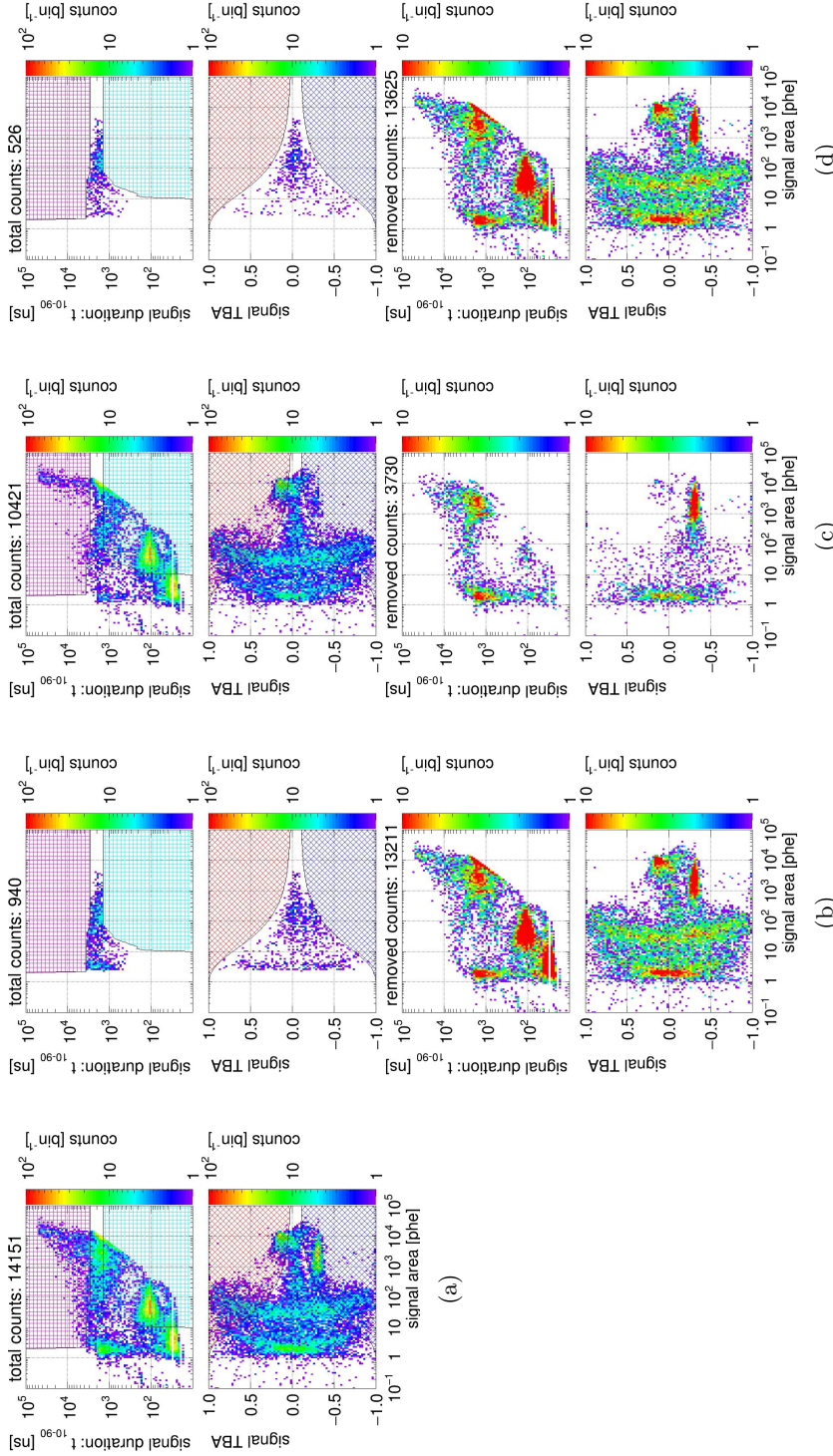


Figure 1.45: *Gas Test* signal selection with ΔV_{T-B} at 12 kV, operating gas density at 0.137 mol L^{-1} . (row one) distribution of t_{10-90} duration vs area after signal selections; (row two) distribution of TBA vs area after signal selections; (row three) distribution of t_{10-90} duration vs area of removed signals; (row four) distribution of TBA vs area of removed signals; (a) coinciding event building; (b) applying signal selections based on signal shape; (c) applying signal selections based on the previous signals. The red hatched shaded area indicates the “top-heavy” region. The blue shaded area indicates the “bottom-heavy” region. The magenta hatched shaded area indicates the “long duration” region. The cyan hatched shaded area indicates the “short duration” region. Data were taken at 2017-12-8 18:24, with grid voltages V_T and V_B at -6 kV and $+6 \text{ kV}$. The duration of data taking is 180.09 s.

1449 a figure with $\Delta V_{T-B} = 12\text{kV}$, at 2 bar

1450 1.10 Evaluation

1451 1.10.1 Simulations

1452 Simulations for electron emission signal is

1453 Detailed discussions of the calculation of the electric field is in Appendix ??.

1454 The evaluation of these cuts are estimated by simulations. Cut efficiency is used to indicate the
1455 quality of the cuts. With evaluating the ratio between the simulated electron emission signal passing
1456 cut and the total counts of simulations, the cut efficiency is estimated as

1457 Survival ratio of the candidate electron emission signals

1458 These two cuts previously mentioned may veto good candidate electron emission signals . Therefore,
1459 survival ratio of the candidate electron emission signals need to be estimated. The survival ratio is
1460 estimated by how much is the fraction of a careful selection of coinciding pulses survive these cuts.
1461 The careful selection of coinciding pulses also need to be uncorrelated from preceding pulses. The
1462 careful selection is the coinciding pulses in t_{25-75} range 0 ns to 200 ns, pulse area range 25 phe to
1463 250 phe. This selection is a conservative selection of S1 pulses that has few contaminations from other
1464 sources. Since S1 is from the primary light production of external particle sources, this selection of
1465 pulses are uncorrelated from preceding pulses. Thus, it can be used for estimating the survival ratio.
1466 The survival ratio is called quiet fraction (QF). For normal operation, QF is in the range of 0.6 to
1467 0.9. Details of this physical sources of S1 pulses will be discussed in the following Section. [1.9.1: S1](#)
1468 conservative population.

$$\text{cut efficiency} \approx \frac{\# \text{ pulses pass cut}}{\# \text{ simulations}} \quad (1.38)$$

1469 Higher cut efficiency indicates that we are capable of preserving more electron emission signals.
1470 Cut efficiency are evaluated with different detector operation conditions, such as gas density and
1471 grids operation voltage. Since the simulated electron emission signal that I used to evaluate the
1472 cuts have a few discrepancies from the real electron emission signal, the cut efficiency will be not be
1473 exactly accurate. Even though this estimate is only an approximation, the overall cut efficiency are
1474 not wildly off.

1475 1.10.2 Summary

1476 To summarize the cuts that I used, to be an electron emission signal candidate, a pulse should satisfy
1477 these conditions. It should

- 1478 • contain coinciding pulse in both PMTs,
- 1479 • uncorrelated from preceding pulses,
 - 1480 – not have any preceding pulse in the previous $100\ \mu s$,
 - 1481 – not have any preceding large pulse in the previous 10 ms,
- 1482 • have the correct pulse shape,
 - 1483 – not noise like,
 - 1484 – not have pulse heavily concentrated only in one of the PMTs,
 - 1485 – have longer than single PHE pulse area or positive pulse duration in at least one PMT,
 - 1486 – not “Cherenkov radiation” like,
 - 1487 – not S1 like,
 - 1488 – not muon like,
 - 1489 – not S1 S2 like,
 - 1490 – t_{10-90} (signal t_{10-90} duration) matches prediction from electron drift time between the
1491 top and bottom grids,
- 1492 • not saturate any PMT (this is required for analysis with condition that gas pressure higher
1493 than 1 bara).

¹⁴⁹⁴ **Appendix A**

¹⁴⁹⁵ ***Gas Test* RQ documentation**

¹⁴⁹⁶ This chapter summarizes the definitions of the RQs that are used for analysis in *Gas Test* analysis.

RQ name	shape	type	unit	default
‘aft_tXX’	array (L,)	float32	ns	nan
	Time difference between the start time of the pulse and the integrated pulse area reach XX% of the total area of pulse. XX=05,25,75,95.			
‘aft_t0’, ‘aft_t1’, ‘aft_t2’.	array (L,)	float32	ns	nan
	equivalent to ‘aft_t01’, ‘aft_t50’, ‘aft_t99’.			
‘arearq’	scalar	string		‘waveareas_trim_end’
	RQ used to compute coincidence pulse area.			
‘AmpThreshold’	scalar	float32	mV	2.5
	The threshold value for computing ‘above_threshold’ RQs.			
‘baselines’	array (L,)	float32	mV	nan
	Pulse baseline voltage.			
‘channels’	array (L,)	uint32		
	Pulse channel number.			
‘coin_pulse_amplitudes’	array (N,C)	float32	mV	nan
	Coincidence pulse amplitudes in each channel.			
‘coin_pulse_amplitudes_neg’	array (N,C)	float32	mV	nan
	Coincidence pulse negative amplitudes in each channel.			
‘coin_pulse_areas’	array (N,C)	float32	mV ns	nan
	Coincidence pulse areas in each channel.			

Continued on next page

RQ name	shape	type	unit	default
‘coin_pulse_areas_neg’	array (N,C)	float32	mV ns	nan
	Coincidence pulse negative areas in each channel.			
‘coin_pulse_areas_norm’	array (N,C)	float32	phe	nan
	Coincidence pulse area in each channel.			
‘coin_pulse_areas_post_TTus’	array (N,C)	float32	phe	0
	Pulse area of TT us after the stop time of a coincidence pulse. TT=100,50,20,10.			
‘coin_pulse_areas_pre_TTus’	array (N,C)	float32	phe	0
	Pulse area of TT us before the start time of a coincidence pulse. TT=100,50,20,10.			
‘coin_pulse_areas_section1’	array (N,C)	float32	phe	0
	Pulse area of a coincidence pulse of section1, which is defined by ‘pulse1_start’ and ‘pulse1_stop’.			
‘coin_pulse_areas_section2’	array (N,C)	float32	phe	0
	Pulse area of a coincidence pulse of section2, which is defined by ‘pulse2_start’ and ‘pulse2_stop’.			
‘coin_pulse_areas_sum’	array (N,)	float32	phe	nan
	Coincidence pulse total area.			
‘coin_pulse_areas_tXX’	array (N,)	float32	ns	nan
	Time difference between the start time of the coincidence pulse and the integrated coincidence pulse area reach XX% of the total area of the coincidence pulse. XX=01,05,10,15,25,50,75,85,90,95,99.			
‘coin_pulse_areas_tXXYY’	array (N,)	float32	ns	nan
	'coin_pulse_areas_tYY'-'coin_pulse_areas_tXX'			
‘coin_pulse_chs’	array (N,10)	int32		-1
	First 10 individual pulse channels in the coincidence pulse.			
‘coin_pulse_ids’	array (N,10)	int32		-1
	First 10 individual pulse ids in the coincidence pulse.			
‘coin_pulse_lastpulse_areas’	array (N,C)	float32	mV ns	nan
	Pulse area of the last pulse before a coincidence pulse in each channel.			
‘coin_pulse_lastpulse_ids’	array (N,C)	int32		-1

Continued on next page

RQ name	shape	type	unit	default
	Pulse id of the last pulse before a coincidence pulse in each channel.			
'coin_pulse_lastpulse_lens'	array (N,C)	float64	ns	nan
	Pulse length of the last pulse before a coincidence pulse in each channel.			
'coin_pulse_lastpulse_times'	array (N,C)	float64	ns	nan
	Start time of the last pulse before a coincidence pulse in each channel (since LZ_EPOCH_DATETIME).			
'coin_pulse_lens'	array (N,)	float64	ns	nan
	Coincidence pulse length.			
'coin_pulse_amplitudes_' peaktime	array (N,)	float64	ns	nan
	Time difference between the start time of the coincidence pulse and normalized coincidence pulse reach maximum amplitude.			
'coin_pulse_amplitudes_' peaktime_smooth	array (N,)	float64	ns	nan
	Time difference between the start time of the coincidence pulse and smoothed normalized coincidence pulse reach maximum amplitude.			
'coin_pulse_times'	array (N,)	float64	ns	nan
	Coincidence pulse start time (since LZ_EPOCH_DATETIME).			
'coin_pulse_waveforms'	list (N,C,W)	float32	mV	0
	Waveforms of a coincidence pulse in each channel.			
'coin_pulse_waveforms_norm'	list (N,C,W)	float32		0
	Waveforms of a coincidence pulse in each channel normalize by single photo electron size.			
'coin_pulse_waveforms_sum'	list (N,W)	float32		0
	Sum of waveforms of a coincidence pulse in all channels normalize by single photo electron size.			
'coin_pulse_wtime_tXXYY'	array (N,)	float32	ns	nan
	Pulse height(h_i) weighted average of time(t_i) between 'coin_pulse_areas_tXX' and 'coin_pulse_areas_tYY'. XXYY=1585, 0595. $\bar{t} = \sum h_i t_i / \sum h_i$.			
'coin_pulse_wtimeN_tXXYY'	array (N,)	float32	ns ^N	nan
	$\sum h_i (t_i - \bar{t})^N / \sum h_i$. XXYY=1585, 0595. N=2,3,4.			
'disp'	scalar	string		

Continued on next page

RQ name	shape	type	unit	default
	Display string ‘a:va;g:vg’. (ex: ‘a:+6.5;g:-6.5.’)			
‘duration’	array (F,)	float64	s	
	Duration of a file.			
‘dv’	scalar	float32	kV	
	Voltage difference between the top grid and the bottom grid.			
‘evtnum’	scalar	int64		
	Number of all computed pulses.			
‘firstvals’	array (L,)	float32	mV	
	Value of the first sample of the pulse.			
‘hft_t1’	array (L,)	float32	ns	
	Time difference between the start time of the pulse and the pulse amplitude reach maximum.			
‘in_coin_pulse’	array (L,)	bool		false
	Whether a pulse is in a coincidence pulse.			
‘neg_area_fraction’	array (L,)	float32		nan
	Ratio of negative pulse area and the sum of positive and negative pulse area.			
‘number_of_channels’	scalar	int32		4
	Number of channels.			
‘pos_area_above_threshold’	array (L,)	float32	mV ns	
	Pulse area above a certain threshold (default: 2.5 mV).			
‘pos_len_above_threshold’	array (L,)	float32	ns	
	Pulse length above a certain threshold (default: 2.5 mV).			
‘pos_len_above_threshold_- percentile_XX’	array (L,)	float32	ns	
	Time difference between the start of coincidence pulse of XX percent of all samples above a certain threshold. XX=05,50,95.			
‘pos_len_above_threshold_- trim_end’	array (L,)	float32	ns	
	Pulse length above a certain threshold excluding the ‘suppress_last_NSamples’ period.			
‘posareas’	array (L,)	float32	mV ns	
	Pulse positive area.			
‘pos_area_pulse1’	array (L,)	float32	mV ns	
	Pulse positive area of section1, which is defined by ‘pulse1_start’ and ‘pulse1_stop’.			
‘pos_area_pulse2’	array (L,)	float32	mV ns	

Continued on next page

RQ name	shape	type	unit	default
	Pulse positive area of section1, which is defined by ‘pulse2_start’ and ‘pulse2_stop’.			
‘pos_area_p1_p2’	array (L,)	float32	mV ns	
	‘pos_area_pulse2’ - ‘pos_area_pulse1’			
‘post_baseline’	array (L,)	float32	mV	
	Pulse baseline computed from the end of the pulse.			
‘post_pulse_length’	scalar	float64	ns	1800
	Pulse length not used in the end of a waveform for coincidence pulse searching.			
‘pre_baseline’	array (L,)	float32	mV	
	Pulse baseline computed from the beginning of the pulse.			
‘pre_pulse_length’	scalar	float64	ns	0
	Pulse length not used in the beginning of a waveform for coincidence pulse searching.			
‘procid’	scalar	string		
	Process id. (ex: [12345])			
‘prompt_frac_TTns’	array (L,)	float32		
	Ratio between the pulse area of the first TT ns and the total pulse area. TT=250,500,750,1000			
‘pulse1_start’	scalar	float64	sample	0
	Start time of pulse section 1.			
‘pulse1_stop’	scalar	float64	sample	75
	Stop time of pulse section 1.			
‘pulse2_start’	scalar	float64	sample	0
	Start time of pulse section 2.			
‘pulse2_stop’	scalar	float64	sample	200
	Stop time of pulse section 2.			
‘random_pulse_areas_post_TTus’	array (M,C)	float32	phe	0
	Pulse area of TT us after a random time. TT=100,50,20,10.			
‘random_pulse_areas_pre_TTus’	array (M,C)	float32	phe	0
	Pulse area of TT us before a random time. TT=100,50,20,10.			
‘random_pulse_times’	array (M,C)	float64	ns	nan
	A random time.			
‘rmsratio’	array (L,)	float32		

Continued on next page

RQ name	shape	type	unit	default
	Ratio between Root mean square (rms) of the waveform and the waveform amplitude.			
'sample_size'	scalar	float64	ns	4
	Sample size of a waveform.			
'skimfactor'	scalar	int64		1
	Ratio between the number of all computed pulses and the number of all recorded pulses.			
'sphe_size'	array (C,)	float64	mV ns	inf
	Pulse area of a single photo electron in each channel.			
'suppress_last_NSamples'	scalar	int32		450
	Number of samples not recorded in the end of a waveform.			
'times'	array (L,)	float64	ns	
	Pulse start time (since LZ_EPOCH_DATETIME).			
'trigvals'	array (L,)	float32	mV	nan
	Pulse trigger voltage.			
'usechannels'	array	int32		[0,2]
	Active channels.			
'va'	scalar	float32	kV	
	Voltage of the top grid.			
'vg'	scalar	float32	kV	
	Voltage of the bottom grid.			
'waveamplitudes'	array (L,)	float32	mV	
	Pulse amplitude.			
'waveareas'	array (L,)	float32	mV ns	
	Pulse area.			
'waveareas_trim_end'	array (L,)	float32	mV ns	nan
	Pulse area suppressing last 'suppress_last_NSamples' samples to 0.			
'waveforms'	list (L,)	float32	mV	nan
	Waveform.			
'wavelens'	array (L,W)	float32	ns	
	Pulse length.			
'window_width'	scalar	float64	ns	1500

Continued on next page

RQ name	shape	type	unit	default
	Window size of coincidence pulse searching. It is also called coincidence window width(CWW).			
'wtime'	array (L,)	float32	ns	nan
	Pulse height(h_i) weighted average of time(t_i). $\bar{t} = \sum h_i t_i / \sum h_i$.			
'wtimeN'	array (L,)	float32	ns ^N	nan
	$\sum h_i (t_i - \bar{t})^N / \sum h_i$. N=2,3,4.			
<p>L: number of all computed pulses. N: number of coincidence pulses. M: number of random pulses. C: number of channels. W: number of samples in a waveform. F: number of files in a dataset. LZ_EPOCH_DATETIME: 2015, Jan, 1st, 00 : 00 : 00. phe: average photo electron area.</p>				

Table A.1: Gas Test RQ documentation

¹⁴⁹⁸ **Appendix B**

¹⁴⁹⁹ **Abbreviations**

¹⁵⁰⁰ This chapter summarizes the abbreviations that occur in this thesis.

¹⁵⁰¹ #: the counts of

¹⁵⁰² ~: approximately

¹⁵⁰³ ADC: Analog-to-Digital Converter

¹⁵⁰⁴ avg.: average

¹⁵⁰⁵ BBN: Big Bang Nucleosynthesis

¹⁵⁰⁶ CCD: Charge-couple device

¹⁵⁰⁷ CDF: Cumulative Distribution Function

¹⁵⁰⁸ CMB: Cosmic Microwave Background

¹⁵⁰⁹ config.: configuration

¹⁵¹⁰ cont.: continued

¹⁵¹¹ CSDA range: Continuous Slowing Down Approximation range

¹⁵¹² CWW: Coincidence Window Width

¹⁵¹³ CV: Coefficient of Variation

¹⁵¹⁴ DAQ: Data AcQuisition

¹⁵¹⁵ DM: Dark Matter

¹⁵¹⁶ dur.: duration

¹⁵¹⁷ EL: ElectroLuminescence

¹⁵¹⁸ ELD: ElectroLuminescence Detector

¹⁵¹⁹ ER: Electron Recoil (event)

¹⁵²⁰ LUX: Large Underground Xenon experiment

¹⁵²¹ LZ: LUX-ZEPLIN experiment

¹⁵²² max.: maximum

¹⁵²³ min.: minimum

¹⁵²⁴ MFC: Mass Flow Controller

- 1525 NR: Nuclear Recoil (event)
1526 PDE: Photon detection efficiency (also called light collection efficiency)
1527 PDF: Probability Distribution Function
1528 PMF: Probability Mass Function
1529 PEEK: PolyEther Ether Ketone
1530 PHD(phd): counts of PHotoelectrons Detected
1531 PHE(phe): SPHE pulse area or counts of (single) PHotoElectrons. In other literatures, it is
1532 sometime called PE(pe).
1533 PMT: Photomultiplier Tube
1534 PPB(ppb): parts per billion atoms/molecules
1535 PTFE: PolyteTraFluoroEthylene
1536 R&D: Research and Development
1537 refl.: reflectivity
1538 RQ: Reduce Quantity of a pulse
1539 S1: primary Scintillation light
1540 S2: secondary Scintillation light
1541 S, SF: Survival Function
1542 SS: Stainless Steel
1543 QE: Quantum Efficiency (of a PMT)
1544 QF: Quiet Fraction
1545 SLAC: SLAC national accelerator laboratory
1546 TBA: Top-Bottom Asymmetry
1547 TPC: Time Projection Chamber (detector)
1548 vs.: versus
1549 WIMP: Weak Interaction Massive Particle
1550 XML: eXtensible Markup Language
1551 Λ CDM: Lambda Cold Dark Matter

1552

Bibliography

- 1553 [1] Hamamatsu Photonics, *Photomultiplier Tubes*, (2006) http://www.hamamatsu.com/resources/pdf/etd/PMT_handbook_v3aE.pdf.
- 1554
- 1555 [2] SAES, *PS3-MT3-R/N SPECIFICATIONS*, (2002) http://www.saespuregas.com/Library/documents/ps3spec_512.pdf.
- 1556
- 1557 [3] KNF Neuberger Incorporated Companies, *Diaphragm-Gas Sampling Pumps with double di-*
1558 *aphragm System*, <https://www.knfsusa.com/products/oem-products/product/products/diaphragm-gas-pumps-and-compressors/double-diaphragm-pumps/>.
- 1559
- 1560 [4] Alicat Scientific, *Operating Manual - MFCs*, http://www.alicat.com/documents/manuals/Gas_Flow_Controller_Manual.pdf.
- 1561
- 1562 [5] T Shutt, *Light guide software for photon propagation (unpublished)*, (2018)
- 1563 [6] C. Silva, “Study of the reflectance distributions of fluoropolymers and other rough surfaces
1564 with interest to scintillation detectors”, (2009).
- 1565 [7] K. Lung et al., “Characterization of the Hamamatsu R11410-10 3-in. photomultiplier tube
1566 for liquid xenon dark matter direct detection experiments”, *Nuclear Instruments and Meth-*
1567 *ods in Physics Research, Section A: Accelerators, Spectrometers, Detectors and Associated*
1568 *Equipment* **696**, 32 (2012).
- 1569 [8] B. Feuerbacher and B. Fitton, “Experimental Investigation of Photoemission from Satellite
1570 Surface Materials”, *Journal of Applied Physics* **43**, 1563 (1972).
- 1571 [9] J. W. Keto, R. E. Gleason, and G. K. Walters, “Production Mechanisms and Radiative Life-
1572 times of Argon and Xenon Molecules Emitting in the Ultraviolet”, *Physical Review Letters*
1573 **33**, 1365 (1974).
- 1574 [10] A. Hitachi et al., “Effect of ionization density on the time dependence of luminescence from
1575 liquid argon and xenon”, *Physical Review B* **27**, 5279 (1983).
- 1576 [11] C. M. B. Monteiro et al., “Secondary scintillation yield in pure xenon”, *Journal of Instrumen-*
1577 *tation* **2**, P05001 (2007).

- 1578 [12] V. Chepel and H. Araújo, “Liquid noble gas detectors for low energy particle physics”, *Journal
1579 of Instrumentation* **8**, R04001 (2013).
- 1580 [13] J. C. Bowe, “Drift velocity of electrons in nitrogen, helium, neon, argon, krypton, and xenon”,
1581 *Phys. Rev.* **117** (1960).
- 1582 [14] C. Geuzaine and J.-F. Remacle, “Gmsh: A 3-D finite element mesh generator with built-in pre-
1583 and post-processing facilities”, *International Journal for Numerical Methods in Engineering*
1584 **79**, 1309 (2009).
- 1585 [15] CSC – Scientific Computing Ltd., *ELMER–a finite element solver for multiphysics*, (1999)
1586 <https://www.csc.fi/web/elmer>.
- 1587 [16] S. Kotila and J. Haataja, “CSC Report on Scientific Computing 1999–2000”, CSC – Scientific
1588 Computing Ltd., Finland (1999).
- 1589 [17] S. Biagi, “Monte Carlo simulation of electron drift and diffusion in counting gases under
1590 the influence of electric and magnetic fields”, *Nuclear Instruments and Methods in Physics
1591 Research Section A: Accelerators, Spectrometers, Detectors and Associated Equipment* **421**,
1592 234 (1999).
- 1593 [18] R. Veenhof, “Garfield, recent developments”, *Nuclear Instruments and Methods in Physics
1594 Research Section A: Accelerators, Spectrometers, Detectors and Associated Equipment* **419**,
1595 726 (1998).
- 1596 [19] W. Blum, W. Riegler, and L. Rolandi, *Particle Detection with Drift Chambers* (Springer, 2008),
1597 p. 448.
- 1598 [20] COMSOL Inc., *COMSOL Multiphysics Reference Manual, version 5.3*, (2018) [https://www.
1599 comsol.com/](https://www.comsol.com/).
- 1600 [21] US Environmental Protection Agency, “EPA Assessment of Risks from Radon in Homes”,
1601 (2017).
- 1602 [22] D. E. Groom, N. V. Mokhov, and S. I. Striganov, “MUON STOPPING POWER AND RANGE
1603 TABLES 10 MeV–100 TeV”, *Atomic Data and Nuclear Data Tables* **78**, 183 (2001).
- 1604 [23] S. J. C. do Carmo et al., “Absolute primary scintillation yield of gaseous xenon under low drift
1605 electric fields for 5.9 keV X-rays”, *Journal of Instrumentation* **3**, P07004 (2008).
- 1606 [24] L. M. P. Fernandes et al., “Primary and secondary scintillation measurements in a Xenon Gas
1607 Proportional Scintillation Counter”, *Journal of Instrumentation* **5**, P09006 (2010).
- 1608 [25] U Fano, “Penetration of Protons, Alpha Particles, and Mesons”, *Annual Review of Nuclear
1609 Science* **13**, 1 (1963).
- 1610 [26] S. P. Ahlen, “Theoretical and experimental aspects of the energy loss of relativistic heavily
1611 ionizing particles”, *Reviews of Modern Physics* **52**, 121 (1980).

- 1612 [27] V. Álvarez et al., “Initial results of NEXT-DEMO, a large-scale prototype of the NEXT-100
1613 experiment”, [Journal of Instrumentation](#) **8**, P04002 (2013).
- 1614 [28] P. Sorensen and K. Kamdin, “Two distinct components of the delayed single electron noise in
1615 liquid xenon emission detectors”, [Journal of Instrumentation](#) **13**, P02032 (2018).
- 1616 [29] A.~Kramida, Yu.~Ralchenko, and J.~Reader, *No Title*, (2018)